5-2009

Characterization of PEM Electrolyzer and PEM Fuel Cell Stacks Using Electrochemical Impedance Spectroscopy

Nilesh V. Dale

CHARACTERIZATION OF PEM ELECTROLYZER AND PEM FUEL CELL STACKS USING ELECTROCHEMICAL IMPEDANCE SPECTROSCOPY

by

Nilesh V. Dale
Bachelor of Engineering, University of Pune, 2001

A Dissertation

Submitted to the Graduate Faculty

of the

University of North Dakota

in partial fulfillment of the requirements

for the degree of

Doctor of Philosophy

Grand Forks, North Dakota
May
2009

This dissertation, submitted by Nilesh V. Dale in partial fulfillment of the requirements for the Degree of Doctor of Philosophy from the University of North Dakota, has been read by the Faculty Advisory Committee under whom the work has been done and is hereby approved.

Chairperson

Co-chairperson

This dissertation meets the standards for appearance, conforms to the style and format requirements of the Graduate School of the University of North Dakota, and is hereby approved.

Dean of the Graduate School

December 22, 2008
Date

PERMISSION

Title Characterization of PEM Electrolyzer And PEM Fuel Cell Stacks Using Electrochemical Impedance Spectroscopy

Department Engineering

Degree Doctor of Philosophy

In presenting this dissertation in partial fulfillment of the requirements for a graduate degree from the University of North Dakota, I agree that the library of this University shall make it freely available for inspection. I further agree that permission for extensive copying for scholarly purposes may be granted by the professor who supervised my dissertation work or, in his absence, by the chairperson of the department or the dean of the Graduate School. It is understood that any copying or publication or other use of this dissertation or part thereof for financial gain shall not be allowed without my written permission. It is also understood that due recognition shall be given to me and to the University of North Dakota in any scholarly use which may be made of any material in my dissertation.

Signature _____

Date 12/17/2008

TABLE OF CONTENTS

LIST OF FIGURES

Figure Page

LIST OF TABLES

ACKNOWLEDGEMENTS

I would like to express my gratitude to my advisor Dr. Michael Mann for his remarkable guidance, tremendous encouragement, technical and financial support throughout all of my work. I would also like thank to my co-advisor Dr. Hossein Salehfar for his directions, intellectual contributions and encouragement for writing several research papers.

I appreciate the comments, suggestions and thoughtful review by my dissertation committee members: Dr. David Pierce, Dr. Brian Tande and Dr. Chandice Covington.

Many thanks to my lovely wife, Aparna, for her care, love, support and help me understand electrical engineering to finish my work. Thanks to my family and friends, who gave me moral and financial support whenever needed. Also, special thanks to Jane, Ed, Kevin and Linda for their love and that they made me feel their place is my home.

I would also like to give my special thanks to Dr. Kevin Harrison for providing foundation for my research by building electrolyzer system and teaching me much technical work. Thanks to Tae-hee Han, Christian Biaku and Andrew Peters for their technical support and friendship.

A big thank to Dave Poppeke for his ideas and undergraduate students to put pieces of their work into finish my research. I would also like to thank the funding agencies U.S. Department of Energy and ND EPSCoR.

Dedication

This dissertation is dedicated to my dear parents; Aai and Nana.

ABSTRACT

In order to compete with currently available hydrogen production technologies, proton exchange membrane (PEM) water electrolysis must be cost effective and efficient. Characterization of the PEM electrolyzer stack can provide better understanding of the processes at the electrode level and losses during the operation to help improve its energy efficiency, important understanding to shape future research and the optimization of stack designs.

PEM fuel cells have seen significant developments in recent years due to their capability as an efficient and environment friendly solution for energy conversion. Understanding the behavior of the PEM fuel cell stack at varying loads is vital for optimizing hybrid systems efficiency. Therefore, it is important to characterize all aspects of a fuel cell when it is running under realistic operating conditions.

Electrochemical impedance spectroscopy (EIS) is the sophisticated method to study the PEM cell behavior due to its electrochemical nature. Characterizing PEM cell stacks using EIS technique has a major advantage of differentiating between contributions of each process towards the overall performance of PEM cell stacks. The contributions of ohmic, kinetic and mass transport losses can be differentiated using EIS studies. A 1.2 kW PEM fuel cell and 6 kW PEM electrolyzer were characterized using this technique. Fuel cell EIS testing was accomplished using a frequency response analyzer (FRA) and programmable electronic DC load over a frequency range from 20 kHz to 50 mHz. EIS studies of 6 kW PEM electrolyzer were carried using the FRA,

modified linear DC power supply and custom build current transformer core. The experimental impedance data were analyzed using Nyquist and Bode plots for different types of losses. Electrolyzer modeling was also done based on thermodynamic principles. Stack parameters such as membrane conductivity, anode and cathode exchange current densities were extracted using Mathematica from experimental data obtained at various temperatures.

Some aspects of hydrogen conditioning and compression are also addressed as a part of this study. A novel technique of hydrogen drying using thermoelectric coolers was developed and tested. Hydrogen compression using electrochemical cell was studied, mathematically modeled and compared with its counterpart mechanical compressor.

CHAPTER 1

INTRODUCTION

1.1 Background

Energy is the backbone of today's modern industrial society. For centuries, fossil-based energy sources have fueled the energy needs of our society. Even today, the world is growing increasingly dependent on fossil fuels. Over the last 150 years, burning fossil fuels has increased the concentration of CO_2 in the atmosphere from 280 to 370 ppm and is expected to pass 550 ppm this century [1]. Today's world energy problems, due to high reliance on coal, oil and natural gas, rising per capita energy use of low income countries, and harmful environmental impacts of fossil-fuel based energy systems, has necessitated the need for clean self-sustained energy systems. Self-sustained and clean energy systems are needed to support sustainable global economic development and to mitigate the effects of green house gases. A shift from fossil-based fuels to nonfossil fuels will take place not due to physical exhaustion/depletion but rather due to their unacceptable cost, politics, our dependence on an oil producing countries for meeting the nation's energy needs and importantly, their harmful environmental impacts [2].

Among the available alternatives to fossil fuels, hydrogen has been touted as a promising energy carrier for the future. When burned, or oxidized in fuel cell, it emits no pollution including no green house gases. As a constituent of water, hydrogen is one of the most abundant elements on earth. In order to use hydrogen as an energy carrier, it is necessary that it be present in unbound form, H_2, for easy availability. A significant

amount of energy is required to obtain unbound hydrogen from H_2O, CH_4 and other hydrogen carriers. Currently, several technologies are under development for hydrogen generation such as reforming of fossil fuels, electrolysis of water using various energy sources (e.g., nuclear, fossil, and renewable), biomass gasification, photo-catalytic splitting of water, and thermolysis of water. Hydrogen production using renewable energy sources offers the best long-term solution. However, the renewable sources are intermittent in nature and have to be over-designed in terms of capacity in the absence of energy storage. Hydrogen offers long term energy storage flexibility.

1.2 Problem Statement

"*Any pathway that includes the conversion of electricity to hydrogen by electrolysis, and then conversion of the hydrogen to electricity via a fuel cell is inefficient and not a desirable basis for an economically and environmentally sound energy policy*" [3]. This conclusion by Frank Kreith et al. clearly states the problems in the pathway of developing a hydrogen economy. To emerge as a promising energy carrier for the future and to achieve all its environmental benefits, hydrogen needs to be produced utilizing renewable energy sources. Almost 95% of hydrogen in the world today is produced from fossil fuels (natural gas, oil and coal). However, fossil fuel based hydrogen production technologies emit CO_2. Today, the use of hydrogen for power generation is minimal due to its high production cost and lack of transportation, storage, and distribution infrastructure. The technological challenges related to efficient and cost effective hydrogen production, storage and end-use technologies are hampering the use of hydrogen as power generation source.

Hydrogen production through water electrolysis is relatively efficient but currently is not a cost competitive. Proton exchange membrane (PEM) electrolysis is a promising technology for production of greenhouse gas free hydrogen using renewable energy sources. However, in order to compete with currently available hydrogen production technologies, PEM water electrolysis must be cost effective and efficient.

The need for efficient, non-polluting, self-sustained energy systems is also attracting more attention to fuel cell technologies. PEM fuel cells have seen significant developments in recent years due to their capability as an efficient and environment friendly solution for energy conversion. In renewable integrated power systems, hydrogen produced through water electrolysis can be used in PEM fuel cells to generate power whenever the renewable energy is not enough to balance the load. In addition, to substantially reduce the green house gases, the use of hydrogen in a fuel cell offers the highest fuel conversion efficiency compared with other technologies [4]. However, the amount of energy that can be released by hydrogen utilization is always lower than the amount of energy required to produce hydrogen [5].

The basic challenges that need to be addressed for hydrogen to become a promising energy carrier includes its high production cost, energy intensive compression processes, storage problems due to its low volumetric energy density, its effective and safe transportation and distribution infrastructure, and its end use in fuel cells.

1.3 Research Hypotheses

This research study is mainly focused on the PEM fuel cell and PEM electrolyzer. A novel technique to control the dew point of hydrogen and electrochemical compression

of hydrogen as an alternative to conventional mechanical compression were also explored. Therefore, this research has separate and multilevel hypotheses.

Physical properties, reaction kinetics and transport phenomenon can cause performance losses in PEM fuel cells and PEM electrolyzers. Electrochemical investigation techniques can be useful in characterizing the PEM cells performance. The generalized hypothesis of this research is: "EIS is an effective tool of characterizing the performance losses of PEM cells at both the cell and stack level".

A PEM fuel cell's energy efficiency can be improved by reducing the voltage losses related to the various processes occurring in the fuel cell. As evidence, the following sub hypotheses were explored as part of the PEM fuel cell study:

1) Performance and properties of a single cell change when several single cells are arranged in series to form a stack.
2) PEM cell losses are dependent on the operating current densities.
3) Single cell performance is dependent on the position of a cell in the stack.
4) Performance of a single cell improves with an increased concentration of hydrogen.
5) The contribution of mass transport loss depends on the dominance of water transport mechanism at that current density.
6) High frequency behavior of PEM fuel cells is dependent on external artefacts, humidity level and amount of hydrogen.
7) High frequency behavior of PEM cells changes with position of cells in the stack.

8) Stack level EIS studies of PEM fuel cells require larger AC signal amplitude than single cell studies currently reported in the literature.

9) Results of the EIS experiment are a function of the stack run time.

For PEM water electrolysis to be a cost competitive and efficient hydrogen production technology, the various losses should be reduced by finding the causes of the losses and optimizing the operating conditions. The thermodynamics of water electrolysis reaction may have an influence on electrical efficiency of the PEM electrolyzer. The following sub hypotheses were explored as part of PEM electrolyzer study:

1) In the absence of an off–the–shelf power supply capable of performing stack level EIS studies of an electrolyzer, PEM electrolyzer stack studies for a frequency range of 20 kHz to 0.5 Hz are possible with novel power supply setups.
2) Increasing the operating temperature increases the efficiency of the electrolyzer.
3) An increase in output hydrogen pressure decreases the electrolyzer efficiency.
4) Temperature dependent equations for reversible potential and higher heating values voltage help in obtaining accurate PEM electrolyzer parameters and electrical efficiency.
5) Anode exchange current density, cathode exchange current density and membrane conductivity increase with increasing operating temperature.

High output pressure of product hydrogen from electrolysis is desirable to reduce the compression cost. However, producing hydrogen at higher pressure may increase the losses in electrolyzer resulting in high energy consumption. Compression of gaseous

hydrogen for high pressure storage is an energy intensive process. The electrochemical compression of hydrogen may provide a better alternative to the conventional mechanical compressor. The following sub-hypotheses were explored as a part of the electrochemical compression study:

1) Electrochemical compression is more efficient than mechanical compression for low pressure applications.
2) Ohmic losses dominate the polarization losses at high pressure when using a PEM cell compressor due to the membrane properties and cell design.

1.4 Research scope

A typical renewable energy based stand-alone energy system consists of a renewable energy source (e.g., wind or solar), power electronics, hydrogen production units, compressor, storage tanks and fuel cells. In this research work, the study is focused on hydrogen production using PEM electrolysis, hydrogen conditioning, hydrogen compression and a PEM fuel cell.

The characterization of PEM cells at the stack level is a very important aspect for future energy research. The literature is rich with studies generating fundamental information relating physical properties to the performance for single PEM cells. So far, the same information has been used to model PEM stack performance. However, some important properties change when cells are stacked together. In real situations, the PEM cell stacks are used and not the single cell. The success of the PEM cell stack in environmental friendly power production and hydrogen generation lies in their efficient conversion of energies. Characterization of the PEM cell stack can provide a better understanding of the processes at the electrode level and losses during the operation to

help improving its energy efficiency. An understanding of stack level properties is important to gain the knowledge at the microelectrode level for the optimization of stack designs. Understanding the behavior of the PEM fuel cell stack at varying loads is vital for optimizing hybrid systems efficiency. Therefore, it is important to characterize all aspects of the fuel cell when it is running under realistic operating conditions. This research was mainly focused on characterization of a 1.2 kW PEM fuel cell and 6 kW PEM electrolyzer stack.

Hydrogen conditioning and its subsequent compression for storage are also identified as key processes in renewable energy systems involving hydrogen production via water electrolysis. A novel technique based on thermoelectric coolers (TEC) to control the dew point of electrolytically generated hydrogen was developed and tested. This conditioned hydrogen can be electrochemically compressed using PEM cells. The hydrogen compression has been identified as an energy intensive process. The study and modeling of the PEM cell compressor was performed to evaluate its performance, losses and limitations.

1.5 Approach

Due to the electrochemical nature of the PEM fuel cell and PEM electrolyzer stack, electrochemical impedance spectroscopy (EIS) is identified as a sophisticated and efficient method to characterize the behavior of these stacks. A literature search helped realize the capabilities of EIS in differentiating between contributions of each process towards the overall performance of PEM cell stacks. The contributions of ohmic, kinetic and mass transport losses can be differentiated using EIS studies. As the fuel cell produces power, its EIS study needs an electronic load with wide frequency and high

current range. The electrolyzer, on the contrary, needs electricity and its EIS study needs a power supply capable of supplying AC power with DC offset over a wide frequency range. Unavailability of this kind power supply in the market makes this study challenging. Efforts were carried out to modify the existing DC power supply and to build a custom current transformer core to fulfill the EIS tests requirements.

Fuel cell EIS tests are accomplished using a frequency response analyzer (FRA) and programmable electronic DC load. The impedance data were obtained for various load currents over a frequency range from 20 kHz to 50 mHz. The experimental impedance data were analyzed using Nyquist and Bode plot for different types of looses. The contribution of ohmic loss because of membrane resistance and anode and cathode activation losses were evaluated towards the performance of the fuel cell. EIS tests were also carried out for group of cells and single cells in the stack at various positions to evaluate their performance and to compare their losses to that with whole stack. The general approach of characterizing the fuel cell using current-voltage (I-V) characteristics was also carried out to verify the results of the EIS tests. I-V characteristics at different fuel cell stack temperatures and at single cells were obtained.

EIS studies of a 6 kW PEM electrolyzer were performed using the FRA, modified linear DC power supply and a custom build current transformer core. Impedance data at higher (20 kHz to 1 kHz) and lower frequency (20 Hz to 0.5 Hz) are obtained at various current levels and different operating conditions. Three power supply setups were proposed to carry the full frequency range (20 kHz to 0.5 Hz) EIS study of the electrolyzer stack in the future. The impedance data were analyzed using Nyquist and Bode plots.

EIS studies for both the PEM fuel cell and PEM electrolyzer are expected to give detailed insight of important electrochemical processes at the electrode level and help understand the membrane-electrode interface mechanisms. Understanding the losses at various operating and loading conditions can help improve performance by better manufacturing processes, material development, thinner membrane and catalyst loading. The EIS test results can help obtain the optimum operating conditions while maximizing the efficiency.

Semiempirical modeling of a PEM electrolyzer based on thermodynamic principles was performed to extract the stack parameters which mostly are proprietary. Temperature dependent equations for the reversible potential and Nernst potential were derived from thermodynamic principles. The temperature dependent Nernst potential is very useful in predicting a more accurate cell voltage of the PEM electrolyzer. The semiempirical modeling results can be used to calculate the accurate electrolyzer energy efficiency at various operating conditions.

The experimental system for a novel technique to control the dew point of hydrogen using Peltier effect based thermoelectric coolers (TECs) proposed by Harrison [6] was developed to test its feasibility. Some modifications were incorporated to the previously proposed dew point control system for efficient performance. The user interface to control this dew point system is developed using LabView. Temperature, pressure, dew point and mass flow sensors were used to monitor the system.

An alternative method to energy intensive mechanical compression of hydrogen using PEM cell compression was evaluated using theoretical modeling. The limiting factors of PEM cell compressors such as water management, back diffusion of hydrogen

and membrane electrode assembly were studied. The comparison study of a PEM cell compressor with its counterpart, mechanical compressor, was carried to evaluate its advantages over mechanical compressor in terms of energy saving.

1.6 Layout of Dissertation

The main body of this dissertation comprises six chapters. Chapter 2 describes the main attributes of hydrogen as an energy carrier. The technologies for hydrogen production, storage and utilization in fuel cell are reviewed. The emphasis is given to the PEM electrolysis hydrogen production and PEM fuel cell technology. UND's PEM electrolysis and PEM fuel cell test setups are described briefly.

Chapter 3 mainly describes the experimental setups designed, developed and used for EIS studies of PEM fuel cell stack and PEM electrolyzer stack. The first part of the chapter discusses the use of EIS technique in PEM cell studies. The second part explains the experimental setups for EIS studies of PEM fuel cell and electrolyzer stacks.

Chapter 4 discusses the primary experimental results of this dissertation research in detail. The first half of the Chapter 4 elaborates on impedance study results for PEM fuel cell and the later half discusses the PEM electrolyzer impedance study results. Most of the EIS results for PEM fuel cell were verified at various current levels. Because of the large data size, it's been stored on the compact disc and given to the primary Advisor.

Chapter 5 presents the semiempirical modeling of the 6 kW PEM electrolyzer and modeling results. Temperature dependent equations for reversible potential derived from thermodynamic principles as a part of this modeling are used to extract the coefficients of the semiempirical equation. The model code from Mathematica is presented in Appendix D.

Chapter 6 reviews the electrochemical compression of hydrogen technology. The mathematical modeling of electrochemical compressor is also presented. The experimental setup designed for a novel technique of controlling the dew point of hydrogen is discussed in the later part of this chapter.

CHAPTER 2

HYDROGEN

2.1 Hydrogen: An Energy Carrier

Hydrogen is the lightest and the first element in the periodic table of elements with an atomic weight 1.00794 and atomic number Z=1. It is the ninth most abundant element on Earth's crust (1400 mg/kg), second most abundant element in Earth's sea after oxygen (1.08×10^5 mg/l) and the most abundant element of the universe [7]. Hydrogen is a colorless, odorless, tasteless gas. It exists as diatomic molecule.

When hydrogen reacts with the oxygen, it forms water and energy is released during the reaction. Low heating value (LHV) and high heating value (HHV) energy densities of hydrogen are distinguished based on the state of H_2O products of the reaction. If the H_2O is in the vapor phase the energy released is called LHV or net calorific value. On the other hand if the H_2O is in form of liquid water then the energy released is called HHV or gross calorific value. Table 1 shows the HHV and LHV for 1 kg of hydrogen.

Table 1: Energy Content for 1 kg (2.2 lb) of Hydrogen (12 m^3) reacting with oxygen to form water [8]

Higher Heating Value	Lower Heating Value
134,200 Btu	113,400 Btu
39.3 kWh	33.2 kWh
141,600 kJ	119,600 kJ
33,800 kcal	28,560 kcal

Positive attributes of hydrogen as an energy carrier are as follows [5]:

i) It can be derived from diverse domestic resources like fossil, nuclear and renewables.

ii) It is compatible with high-efficiency fuel cells, combustion turbines and reciprocating engines to produce power with non zero emissions of criteria pollutants.

iii) It produces near non zero emission of gases from renewable and nuclear sources.

iv) It can serve all sectors of the economy including transportation, power, industrial and buildings [9].

v) It has the highest energy content per unit of weight of any known fuel.

vi) Liquid hydrogen is the best transportation fuel based upon utilization efficiency and mass energy density compared to gasoline, jet fuel and alcohols [10].

vii) At the user end, hydrogen can be converted to useful energy forms (thermal, mechanical and electrical) through five processes compared to only one (i.e. flame combustion) for fossil fuels [10].

viii) Hydrogen is 39% more efficient than fossil fuels when it comes to the conversion efficiency at the user end [10].

ix) Hydrogen is the safest fuel in terms of hazards and toxicity [10].

2.2 Hydrogen Production Technologies

Hydrogen production technologies can be categorized as,

A. Thermal Process

B. Electrolytic Process

C. Photolytic Process

A. Thermal Processes: Hydrogen can be produced from thermal processes utilizing the energy in various resources such as natural gas, coal or biomass. The thermal processes used to produce hydrogen are as follows.

I. Natural gas reforming

II. Coal gasification

III. Biomass gasification

IV. Reforming of renewable liquid fuels

V. High temperature steam electrolysis

B. Electrolytic Processes

Hydrogen production through electrolytic processes uses electricity to split water into hydrogen and oxygen. Though the electrolytic hydrogen production process is an energy intensive process, it can result in zero greenhouse gas emissions if the source of electricity used is from renewables or other clean energy sources. The water splitting reaction takes place in a unit called electrolyzer. Electrolyzers can be classified as, proton exchange membrane (PEM) electrolyzers, alkaline electrolyzers and solid oxide electrolyzers.

In PEM electrolyzers, the electrolyte is a solid polymer membrane which has selectivity for hydrogen ions or protons. Alkaline electrolyzers use an alkaline solution, generally sodium or potassium hydroxide, which acts as an electrolyte. Solid ceramic material is used as an electrolyte in solid oxide electrolyzers. Unlike the PEM electrolyzer membrane, the negatively charged oxygen ions are transported through the solid oxide electrolyzer's membrane at elevated temperatures. Solid oxide electrolyzers

operate at high temperature about 500–800 °C. The operating temperatures for PEM and alkaline electrolyzer are about 80–100 °C and 100–150 °C, respectively.

2.2.1 PEM Electrolysis

Proton exchange membrane electrolyzers are also known as solid polymer electrolyzers (SPE). In PEM electrolyzers, a polymer membrane, generally Nafion®, separates the gases and provide conductivity to protons. A single PEM electrolytic cell has two electrodes, anode and cathode, PEM and catalyst layer. Water at the anode reacts to form oxygen and protons (H^+). Protons selectively migrate across the PEM to the cathode and electrons flow through the external circuit. At the cathode, protons combine with electrons to form hydrogen gas. PEM electrolyzers offer high current densities which contributes its compact size and fewer cells than their alkaline counterparts. The PEM electrolyzer's capability to handle high pressure differential across the membrane can help produce hydrogen at higher pressures reducing the compression stages for high pressure storage. In PEM electrolyzers, oxygen can not enter the hydrogen stream because of membrane selectivity for protons. PEM electrolyzers use only clean water and electricity to produce pure hydrogen unlike alkaline electrolyzers generally use potassium hydroxide (KOH) which is extremely corrosive especially at 60 °C operating temperature.

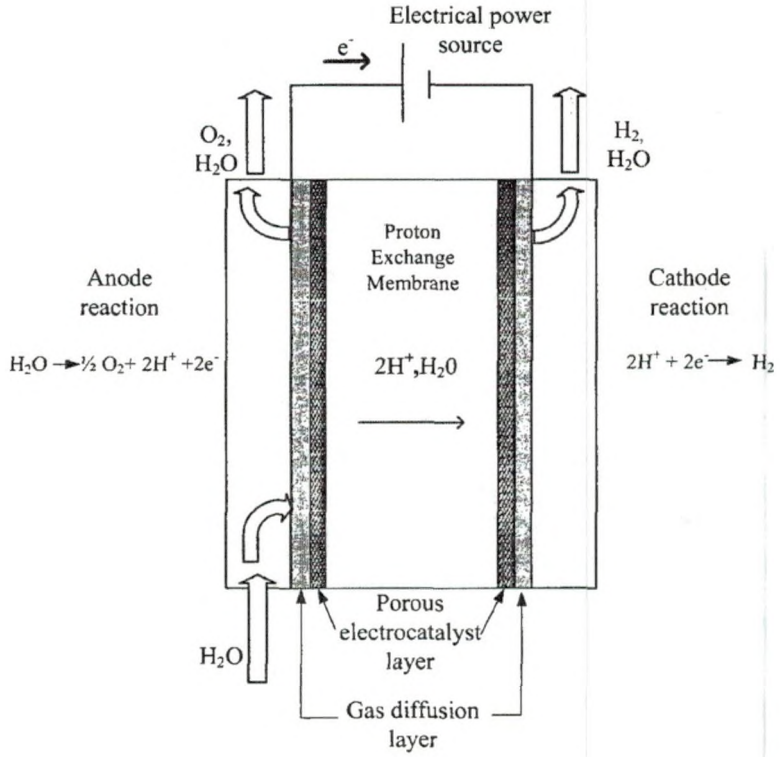

Figure 1: PEM electrolysis cell components with anode and cathode reactions

The PEM water electrolysis cell primarily consists of a PEM with two electrodes, namely anode and cathode, bonded on it on either side. These electrodes have catalyst particles on them. Generally, different electrocatalysts are used for the anode (e.g., IrO_2) and cathode (e.g., Pt) [11]. The PEM bonded with the catalyst layer and electrodes is also referred as membrane electrode assembly (MEA). A porous backing like metallic meshes is used to establish the electric contact and mechanical support [12].

2.2.2 UND's PEM Electrolysis System

The University of North Dakota (UND) has established a renewable hydrogen test facility to address the system integration issues of wind-based electrolytic hydrogen production. In addition to the electrolytic hydrogen production system the test facility is equipped with a PEM fuel cell test facility. The overall PEM electrolysis system is

designed to allow the precise control over operating temperature, hydrogen system pressure, water resistivity, water flow, stack current and safety. Along with the temperature, pressure and current-voltage sensors, the main components of the system are a 6 kW PEM electrolyzer stack, hydrogen-water phase separator, two 6 kW Xantrex DC power supplies [13] which are capable of delivering up to 200 A to the electrolyzer, a temperature controlled water loop, a two-tube desiccant drying system and a back pressure regulator to control the operating pressure. Figure 2 shows the overall PEM electrolysis system.

A National Instruments (NI) signal conditioning extension for instrumentation (SCXI) data acquisition system is used with LabView program to monitor, control and record operational data. A safety interlock loop allows system operation only after series of vital components status checks.

Water quality is an important aspect of the PEM electrolyzer. The manufacturer defines minimum water resistivity to be 1 MΩ-cm [14]. High resistivity is associated with water purity. Contaminants such as electrolytes and ions found in water make it conducting for electricity. Removing these contaminants increases the resistivity of the water. To remove these contaminants and ions the water is filtered and deionized (DI) using mixed bed resins and carbon filters. To avoid any further contamination of DI water, polypropylene tubing is used before it enters the electrolyzer. The polypropylene reservoir tank also used as a oxygen-water separator.

A temperature control unit (chiller) from Lytron [15] controls the inlet DI water temperature thereby providing control of the operating temperature of electrolyzer. This system is designed to allow higher temperature testing by maintaining DI water

temperature with the chiller and a heater provided in oxygen-water phase separator. The mixed bed filters currently limit the operation to roughly 60°C. At temperatures higher than 60°C the resins used for deionization breaks down. For this reason to perform high temperature tests, first the resistivity of water is raised higher than the required level (upto 6–7 MΩ-cm) and then the temperature of DI water is raised with a heater. This temperature controlled DI water, with the help of pump inside the chiller, is then supplied to the electrolyzer stack bypassing the mixed bed resins and carbon filter. This allows tests at desired temperature and water quality. The resistivity of the DI water is monitored in the oxygen-water phase separator, before pumping water into the stack. The flow of the DI water to the stack is controlled between 1.5 to 2.5 gallon per minute. Except at high temperatures, if resistivity is lower than required, then water is cycled through mixed bed filters again until desired resistivity is achieved. Two combustible gas detectors monitor the safe operation in the test facility room. One is mounted in the canopy hood directly above the experimental table and another to the oxygen phase separator to monitor the accidental mixing of oxygen and hydrogen. Both detectors are set at 10% of lower flammability limit (LFL) of hydrogen in air to alarm and at 20% of LFL of hydrogen in air to initiate shutdown process using data acquisition system and software program LabView.

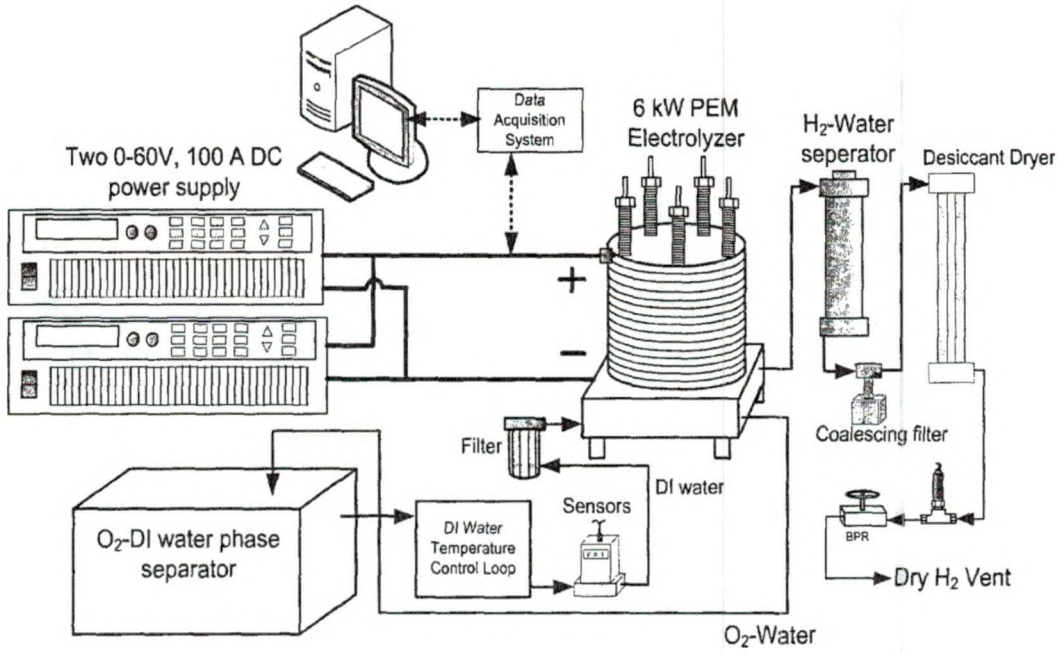

Figure 2: Experimental setup for a 6 kW PEM electrolysis system with temperature control

The interlock loop was designed to insure the safe operation of the system. In the event the combustible gas detector senses the preset limit of % lower flammability limit (LFL) while system is operating, the control software senses the alarm signal to turn off the system. In any event, the interlock loop devices interrupt the loop; power supplies output are turned off. Also, in any fault condition, power supply to stack can be turned off by pressing manual emergency stop. If system is running and the emergency stop is pressed the pressurized hydrogen is vented out through a solenoid valve. This interlock loop enables or disables the power supplies to electrolyzer stack depending on the state of the electromechanical relays which are wired to combustible gas detector [6].

The DI water loop maintains the temperature and resistivity of water using the Lytron's Kodiak® chiller and carbon mixed bed filters respectively. The oxygen phase separator is equipped with a level sensing float, temperature, resistivity and combustible

gas detector sensors to monitor system performance and safety. After achieving the desired resistivity and temperature of DI water, the stack is supplied with power using two DC power supplies and DI water is run through the stack. Before entering the stack, DI water goes through 10 μm filter and sensing stage where its temperature, flow, pressure and resistivity are monitored again for stable and safe operation. Hydrogen gas coming out of the cathode side is separated from liquid water in a high pressure hydrogen-water separator. A coalescing filter, immediately following the separator, removes most of the remaining liquid water from hydrogen gas. An automatic drain connected to the coalescing filter collects and recycles the DI water back to external reservoir with the help of hydrogen system pressure. A two tube desiccant drying system performs the remaining drying process of the hydrogen gas. Dry hydrogen product gas then enters the sensing stage equipped with mass flow, temperature, pressure and dew point sensors. A back pressure regulator can be adjusted to maintain the hydrogen system pressure. Oxygen from the anode side is separated from DI water in oxygen phase separator where oxygen is then vented using a check valve and DI water is reused. Currently, the product hydrogen is vented in the atmosphere; however, it can be conditioned using the novel technique utilizing thermoelectric coolers proposed and tested as a part of this work. The conditioned hydrogen can be stored in composite pressure tank using mechanical or electrochemical compressor in future.

2.3 Hydrogen Conditioning, Compression and Storage

Renewably generated hydrogen and fuel cell systems are seen as key energy system solutions for future. However, hydrogen's low volumetric energy density is a significant problem in realizing these future energy systems at lower costs and higher

efficiencies. The volumetric density of hydrogen can be increased by compression or liquefaction. Although both the technologies are mature and have been practiced for many years, both processes are energy intense which increases the overall cost of hydrogen use for electricity or power generation.

In the case of hydrogen production through water electrolysis, product hydrogen coming out the electrolyzer is 100 % saturated. It contains liquid water as well as water vapor. The saturated hydrogen needs to be dried before compressing it for storage. Generally, this drying is achieved using a desiccant drying method. The two tube desiccant drying system, as in case of Proton Energy System's HOGEN40® generator [16], uses 10% of the dried hydrogen to regenerate its desiccant. This hydrogen loss affects the overall system efficiency. An alternative method for hydrogen drying using thermoelectric coolers was proposed and developed as part of this work. The details of the system are discussed in Chapter 6.

Hydrogen storage in compressed gas form is a well established technology. Mechanical compression is the most common means to achieve pressurization; however, it suffers from limitations such as intensive energy use, wear and tear of moving parts, hydrogen embrittlement, excessive noise, bulky equipment and contamination of gas usually by compressor lubricant. In a diaphragm compressor, the contamination of the gas by lubricant can be avoided, yet it still suffers from other limitations. The diaphragm has to be replaced over a period of time. Non-mechanical pressurization by thermal cycling is possible, but this is also energy intensive and not commercially practical yet. An alternative means to compress hydrogen is use of polymer electrolyte membrane

(PEM) cells. The hydrogen compression using PEM cell in discussed in detail in Chapter 6.

The current hydrogen storage technologies with their limitations are summarized below

1) Liquid hydrogen: Liquid hydrogen is stored at cryogenic temperatures (i.e., at its boiling point -235 °C). Liquid hydrogen has a density of 70.8 g/L. Liquid hydrogen requires less volume than compressed hydrogen storage. However, the energy required for the liquefied hydrogen storage is three times more than the energy required to store that hydrogen at 70 MPa [17]. It is challenging to store the hydrogen at those temperatures and any heat transfer causes some hydrogen to evaporate. This storage technology has special handling needs and requires extensive energy to liquefy the hydrogen gas.
2) Compressed hydrogen: Hydrogen storage in compressed form is one of the simplest and most mature technologies. However, new tank designs for increased strength-to-weight ratio, safety, cost reduction and higher pressure range are necessary. At present, this is the most promising hydrogen storage options due to availability of 35 MPa and 70 MPa storage tanks. At 35 Mpa, compressed hydrogen storage has density of 23.5 g/L. To store 6 kg of hydrogen requires 255 L (67.5 gallons) in compressed gaseous form as compared to 85 L (22.4 gallons) in liquid form.
3) Metal hydrides: Hydrogen can be stored in the metal hydride forms by chemically bonding the hydrogen to the metal. Some hydrides can adsorb the hydrogen at or below atmospheric pressures and can release the hydrogen at higher pressure when

heated. This storage method is advantageous for lower pressure storage at a reasonable volumetric energy density.

4) Activated carbon hydrogen storage: Hydrogen can be stored as a liquid and a low temperature gas in the micropores of the carbon. Surface area and pore size distribution defines its capacity for hydrogen storage. The hydrogen is stored in the micropores of the carbon by physisorption process.

2.4 Fuel Cell Technology

A fuel cell is an electrochemical device which converts chemical energy stored in the hydrogen directly into electrical energy with only by-product as water. Hydrogen is used as a fuel and oxygen (air) serves as an oxidant. The basic fuel cell consists of a electrolyte with an electrode on each side. Fuel cells are classified based on the type of electrolyte used. Besides the electrolyte type, they also differ in operating temperature, application and efficiency.

Table 2: Fuel cell classification [18]

Fuel Cell Type	Electrolyte	Mobile ion	Operating Temperature
Alkaline Fuel Cell (AFC)	Potassium hydroxide solution (KOH)	OH^-	50 – 200 °C
Proton Exchange Membrane Fuel Cell (PEMFC)	Proton exchange membrane	H^+	30 – 100 °C
Direct Methanol Fuel Cell (DMFC)	Proton exchange membrane	H^+	20 – 90 °C
Phosphoric Acid Fuel Cell (PAFC)	Phosphoric acid	H^+	160 – 200 °C
Molten Carbonate Fuel Cell (MCFC)	Molten mixture of alkali metal carbonates	CO_3^{2-}	620 – 660 °C
Solid Oxide Fuel Cell (SOFC)	Oxide ion conducting ceramic	O^{2-}	500 – 1000 °C

2.4.1 Fuel Cell Advantages and Disadvantages

Fuel cells show some common characteristics with the combustion engines as both produce power as long as they are supplied with fuel, and with primary batteries as both rely on electrochemistry to work. Fuel cells are often more efficient than combustion engines as they produce electricity directly from chemical energy. Fuel cells have no moving parts which can result in long lasting and silent systems. In the absence of combustion NO_x, SO_x and particulate matter emissions are nearly zero. Fuel cells can be easily scaled according to power and capacity requirement. Fuel cells offer higher energy densities and longer life compared to the batteries.

Cost is the biggest disadvantage of the current fuel cell technology. Fuel availability and storage are the next problems, as hydrogen has low volumetric energy density and is difficult to store economically. The other problems associated with fuel cell technology are its operational temperature capability, susceptibility to environmental poisoning, and startup/stop cycle durability [19].

2.4.2 Fuel Cell Thermodynamics

Hydrogen and oxygen combine in a fuel cell to produce electrical energy. The total heat energy released in the fuel cell reaction is given by change in enthalpy, ΔH. At standard conditions (1 atm and 298.15 K), $\Delta H°$ for the hydrogen/oxygen reaction is -285.83 kJ/mole. However, this is not the energy that can be extracted from fuel cell reaction. In the process of hydrogen/oxygen combination the entropy of the gases decreases by 48.7 kJ. The entropy in the amount of $T\Delta S$ will be expelled to the environment as heat at temperature T. The thermodynamically extractable energy of the reaction is given as change in Gibbs free energy (ΔG) by subtracting the heat expelled to

the environment (TΔS) from the total heat energy released in the reaction (ΔH). At standard conditions, ΔG° for hydrogen/oxygen reaction is – 237.14 kJ/mole. The ideal efficiency of the fuel cell can be given by,

$$\eta = \frac{\text{Thermodynamically extractable energy}}{\text{Total heat energy released}} = \frac{\Delta G}{\Delta H} \qquad 2\text{-}1$$

Thus, the theoretical efficiency limit for the fuel cell reaction is 83%.

The useful extractable energy, ΔG can be expressed as an electric potential, or voltage (E_0) using following equation,

$$E_0 = -\frac{\Delta G}{nF} \qquad 2\text{-}2$$

where, F is the Faraday constant (96,485 C/mol of e^-) and n =2 is the number of electrons per mole involved in the reaction. At standard conditions, this equation gives 1.23 V. This voltage is referred as the fuel cell open circuit voltage (OCV).

The change in Gibbs free energy is dependent on the change in enthalpy of the reaction. Enthalpy is a function of temperature and pressure. Therefore, Gibbs free energy changes with temperature and pressures. Hence, the fuel cell open circuit voltage changes with the operating conditions. This dependence is given by Nernst Equation [18].

$$E_{Nernst} = E_0 + \frac{RT}{2F} \ln\left(\frac{P_{H_2} P_{O_2}^{0.5}}{P_{H_2O}}\right) \qquad 2\text{-}3$$

where, R is the universal gas constant (8.314 J mol^{-1} K^{-1}), T is temperature in Kelvin, and P_i is the partial pressure of the species i.

2.4.3 Fuel Cell Losses

In practical situations, the actual fuel cell voltage is less than the thermodynamically predicted voltage due to irreversible kinetic losses. If more current is

drawn from fuel cell, the cell voltage declines due to an increase in losses. In general, there are four fuel cell losses which define the current voltage characteristics of a fuel cell.

1. Fuel crossover
2. Activation losses
3. Ohmic losses
4. Concentration or mass transport losses

Fuel Crossover

The fuel cell voltage is less than the thermodynamically predicted voltage even when current is not drawn from the fuel cell. This decrease in voltage is due to the fuel and electron leak across the membrane. Though the fuel cell electrolyte is selective for only protons, a certain amount of gas and electron flow is possible.

Activation Losses

The voltage of the fuel cell drops due to the "sluggishness" of the reactions at the anode and cathode electrode. The oxygen reduction reaction at the cathode is slower and accounts to the most of the activation losses. The reactants have to overcome an energy barrier to convert into the product. A portion of the voltage generated is lost in lowering this barrier to drive the chemical reaction. It is related to the activation energy required at both the anode and the cathode of the fuel cell, hence referred as activation loss. The relation between activation overvoltage and current is described by Tafel equation [18].

$$\eta_{act} = \frac{RT}{\alpha F} \ln \frac{i}{i_o} \qquad 2\text{-}4$$

where, i is the current density (A/cm^2), i_o is exchange current density (A/cm^2), and α is charge transfer coefficient (CTC).

At zero current density, the fuel cell reaction does take place at the fuel cell electrode. However, the reverse reaction is also taking place at the same rate which establishes the equilibrium between the forward and backward reactions. This current density is referred as the exchange current density [18]. The exchange current density is crucial in controlling the fuel cell electrode performance. Activation losses are minimized by maximizing the exchange current density. The exchange current density is a function of the catalyst and reaction surface area. The activation losses in the fuel cells can be reduced by raising the cell temperature, using more effective catalyst, increasing the roughness of the electrodes, increasing reactant concentration, and increasing the pressure.

Ohmic Losses

The losses due to the resistance to the flow of ions through the electrolyte and the electrical resistance of the electrode are referred as ohmic losses. In most fuel cells, the resistance is mainly caused by the electrolyte. However, the resistance due to the cell interconnects or bipolar plates also contribute to this loss. The total ohmic resistance (R_Ω) of the cell can be expressed as a sum of contributions from the contact resistance and ohmic resistance of the cell components such as, membrane, catalyst layer, and end plates.

Concentration or Mass Transport Losses

At high current densities, the fuel cell output voltage drops rapidly due to the mass transport limitations. This loss is significant at higher current densities when the reactants at the electrode surface are consumed more rapidly than they are replenished. This voltage loss due to the reduction of the reactant's concentration in the gas channels

is called concentration loss. This loss sometimes is called the gas diffusion loss due to the diffusive resistance of the gas diffusion layer to the gases.

In fuel cell modeling, the mass transport losses and concentration losses are used as an interchangeable terms. However, concentration loss is a subset of mass transport loss.

2.4.4 PEM Fuel Cell

The proton exchange membrane (PEM) fuel cell uses an ion conducting solid electrolyte membrane. The PEM fuel cell is also termed as polymer electrolyte membrane fuel cell. A solid polymer electrolyte has advantages such as high power density and less corrosion over liquid electrolytes. PEM fuel cells operate at lower temperature which allows faster start up and immediate response to changes in the load. The wide power range and versatility allows their use in large number of applications. The PEM fuel cells are seen as promising choice for transportation applications due to their power ranging upto several kilowatts with temperature only varying from room temperature to 100 °C.

PEM fuel cells use hydrogen as a fuel and oxygen, generally from air, as an oxidant to produce electricity and water. The PEM fuel cell primarily consists a of positively charged electrode, i.e. anode, a polymer electrolyte membrane and a negatively charged electrode, cathode. Hydrogen gas introduced at the anode oxidizes to protons (H^+). Protons migrate through polymer electrolyte membrane from anode to cathode and electrons flow to the cathode through an external circuit. Oxygen introduced at the cathode reacts with protons and electrons to form the product water and heat. A catalyst is essential for the electrochemical conversion of hydrogen and oxygen in the fuel cell.

Therefore, in PEM fuel cells both the anode and the cathode contain catalyst, usually platinum (Pt), to boost the electrochemical reaction.

The PEM fuel cell electrode reactions are shown below,

Anode reaction: $H_2 \rightarrow 2H^+ + 2e^-$ 2-5

Cathode reaction: $\frac{1}{2}O_2 + 2H^+ + 2e^- \rightarrow H_2O + \text{heat}$ 2-6

Overall reaction: $H_2 + \frac{1}{2}O_2 \rightarrow H_2O + \text{heat}$ 2-7

The basic PEM fuel cell operation is shown in Figure 3.

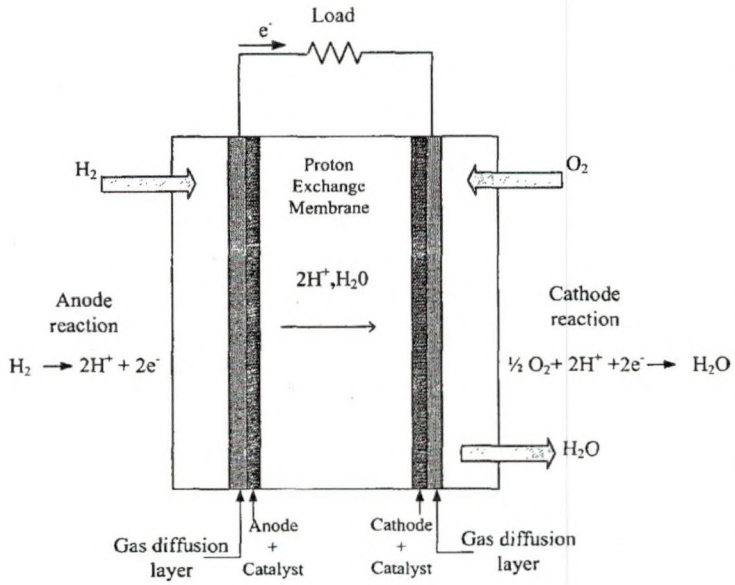

Figure 3: PEM fuel cell components with electrode reactions

2.4.5 UND's PEM Fuel Cell System

UND's renewable hydrogen test facility has two 1.2 kW Ballard's Nexa™ [20] PEM fuel cells. The Ballard's Nexa™ PEM fuel cell system has 47 membrane electrode assemblies (MEA). It is a fully integrated system that produces 1200 W unregulated DC power using hydrogen and air. An integrated control board, onboard sensors and a

microprocessor monitor the system performance and allow a fully automated fuel cell operation. This PEM fuel cell stack is capable of supplying 44 A. Its output voltage varies ranging from 43 V at no load and 26 V at full load [21]. The Nexa™ power module operates on pure and dry hydrogen and room air. The air is humidified before reaching the fuel cell to maintain the membrane saturation. The stack is air cooled. Hydrogen inlet, oxidant air and cooling air flow rates are controlled using an embedded control board. The compressor's speed that supply oxidant air and the cooling air fan speed are adjusted by the control board to match the current requirement

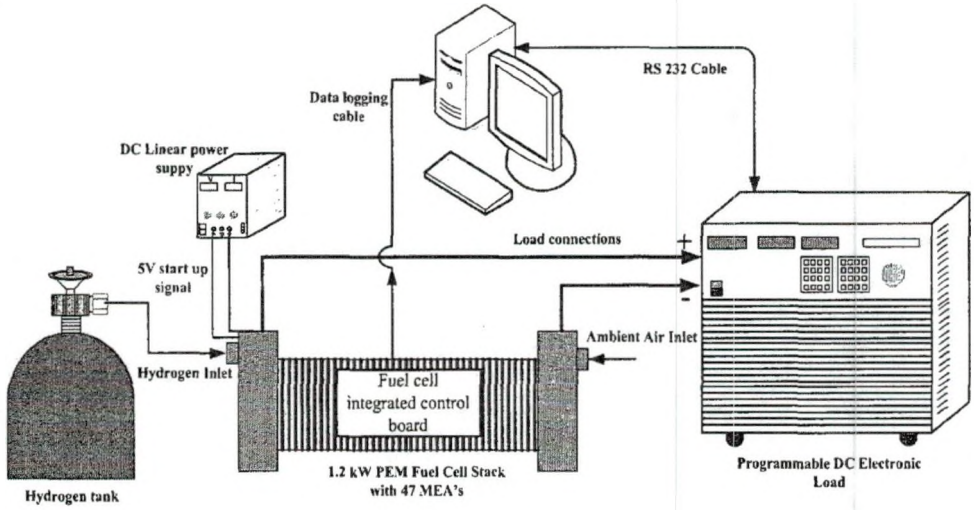

Figure 4: PEM fuel cell experimental setup

As shown in Figure 4, hydrogen is supplied to the PEM fuel cell stack from a hydrogen tank. The Nexa™ fuel cell operates at 5 psi hydrogen pressure. The procedure followed to supply the hydrogen from hydrogen tank to the fuel cell is summarized in Appendix A. The fuel cell is connected to the DC electronic load using 4 guage load wires. The DC load is controlled through its software program using RS 232 cable connected to the computer (Comp 2). The Nexa™ fuel cell needs 5 V start up signal

before it starts producing power. Therefore, a linear DC power supply is connected to the fuel cell control board to supply the start up signal. A LabView interface with the help of integrated control board monitors and controls the operation of fuel cell stack.

CHAPTER 3

AC IMPEDANCE STUDIES OF PEM CELL STACKS

3.1 Electrochemical Impedance Spectroscopy

The most common technique to study PEM cell behavior involves examining its current-voltage characteristics as this technique reveals the different electrode processes occurring at various current densities [22]. However, current-voltage characteristics do not help understand the membrane-electrode interface mechanisms and the individual contribution of each process occurring at the electrode level. Transient techniques such as current interrupt, potential sweeping, potential stepping and electrochemical impedance spectroscopy (EIS) have also been used to characterize fuel cells [23, 24, 25]. EIS helps understand the chemical and physical processes in solutions as well as solids. EIS is the most sophisticated method to study the PEM cell behavior because of its electrochemical nature. Researchers [26,27,28] have demonstrated EIS's capabilities to study the fundamental processes of fuel cells.

Various microscopic processes takes place in a PEM cell when electricity is supplied to it (e.g., electrolyzer) or electricity is drawn from it (e.g., fuel cell). These processes include electron transport through electronic conductor, at the electrode-electrolyte interface and transfer of charged atoms through an electrolyte. A number of parameters such as conductivity of the membrane, dielectric constant, adsorption reaction rate constant at electrode-material interface, capacitance of the interface region, diffusion

coefficient of the species and the equilibrium concentrations of the charged species can be derived from EIS studies [29].

The EIS study is done by applying a small sinusoidal voltage or current perturbation around a steady-state value and measuring the resulting current or voltage along with the phase angle. The data is used to calculate real and imaginary impedances and plotted them against each other for different frequency perturbations. The real part of the complex impedance is pure resistance and the imaginary part is combination of capacitance and inductance. Nyquist and Bode plots can be used for analyzing the impedance data. Nyquist plots are common way of analyzing the impedance data. However, the frequency dependence of the impedance can not be revealed in Nyquist plot. On the other hand, the Bode plot provides information on the frequency dependence of the impedance.

Generally, in an impedance spectrum, the high frequency region (> 100 Hz) reflects the charge transport in the catalyst layer, whereas the low-frequency region (<0.01 Hz) reveals the mass transport in the gas diffusion layer, the catalyst layer and the membrane. The steady state value of the current at which the EIS experiment is carried out determines the importance of the transport processes. The mass transport resistance is not significant at low current levels. Charge transport contributes to the impedance at low current levels and mass transport at high current levels [30].

Initial EIS studies performed on PEM fuel cells were intended to understand charge transport in different sections of the membrane electrode assembly (MEA): the catalyst and gas diffusion layers and membrane [30, 31]. With this knowledge, catalyst performance, electrode parameters and membrane performance can be understood at

normal operation. This information can be used by cell and system designers. Only recently have studies been devoted to observing impedance changes under extreme operating conditions of fuel cells which could lead to failure such as a flooded electrode, dry membrane and catalyst poisoning [31, 32]. Based on this understanding, EIS can be used as a diagnostic technique. EIS gives significantly more information about the cause of failure than monitoring the terminal voltage output of the fuel cell. Conventional techniques that monitor the voltage alone cannot distinguish between failure modes because several failures result in the same low voltage at the fuel cell terminal. These failures include a dry membrane, low partial pressure of oxygen or hydrogen, and blockage of the anode by water as a result of back diffusion of water from cathode to the anode. EIS can differentiate between these and other failure modes.

Some investigators have used EIS to develop electrical equivalent circuits of PEM fuel cells for modeling purposes [30,33, 34, 35]. The use of experimentally determined parameters greatly improves modeling accuracy and validity. These equivalent circuits consist of components like capacitors, resistors and in some cases inductors. The constant phase element (CPE) and Warburg impedance are also used in equivalent circuits to accurately model the activation and mass transport losses respectively.

3.2 EIS Studies of PEM Fuel Cell

EIS studies of PEM fuel cells operating under various loading conditions are of prime importance for integrated power systems where the load is never constant. Characterizing fuel cells using EIS technique has a major advantage of differentiating between contributions of each process towards the overall performance of fuel cell. The contributions of ohmic, kinetic and mass transport losses can be differentiated using EIS

studies. EIS spectrum of the PEM fuel cell is generally dominated by the activities at the cathode. The cathode overpotential is the main contributor to the impedance spectrum obtained for fuel cell because the oxygen reduction reaction (ORR) at the cathode is slower than hydrogen oxidation reaction (HOR) at the anode.

Most of the EIS studies of PEM fuel cells to date are focused on the single cell [36, 37, 38, 39]. Recently, a few studies have investigated fuel cell stacks as well [40, 41, 42]. Most of the stack level EIS studies, however, do not take into account the effect of the control systems integrated with the fuel cell stack on its behavior. For example, in the case of Ballard's Nexa™ PEM fuel cell, decaying system voltage changes because of the purging process which is controlled by an integrated control board. As a result of this purging process, the output voltage is not perfectly constant at a given load. The integration of this and other process operation/control systems into the fuel cell is an important step in transferring the fuel cell technology from laboratories to practical applications. Therefore, when integrating this type of fuel cell into a power system, the effect of all system components on the fuel cell behavior must be taken into account.

The performance analysis of a PEM fuel cell stack without the embedded controls has been studied by W. Zhu et al. [40]. In their work, a single fuel cell, a group of fuel cells, and a complete stack were studied without embedded controls using ac impedance studies. However, the objective of the work is to perform EIS analysis of a PEM fuel cell stack with its embedded controls. This work is focused on studying the behavior of the whole stack, group of cells and individual cells placed at different locations in the stack under various loading conditions. In the present work, the results from the whole stack ac impedance study reported by W. Zhu et al. are verified with a

different experimental setup. In addition, the wide frequency range (20 kHz – 50 mHz) used in this work allows one to study the high and low frequency behaviors of the individual cells and the whole stack. This study is performed at the system controlled hydrogen flow rate, oxidant air flow rate, temperature, air stoichometry and humidity. The effects of control processes such as purging can be seen on impedance data.

During fuel cell operation, nitrogen and product water in the air stream slowly migrate across the fuel cell membrane and accumulate in the hydrogen stream. This accumulation of nitrogen and water at the anode decreases the voltage of certain cells in the PEM stack. These cells are termed as "purge cells". A hydrogen purge valve at the stack outlet is periodically opened in response to the purge cell voltage to flush out the accumulated constituents at the anode to restore the system voltage. Purging occurs frequently when the fuel cell is operating at high currents.

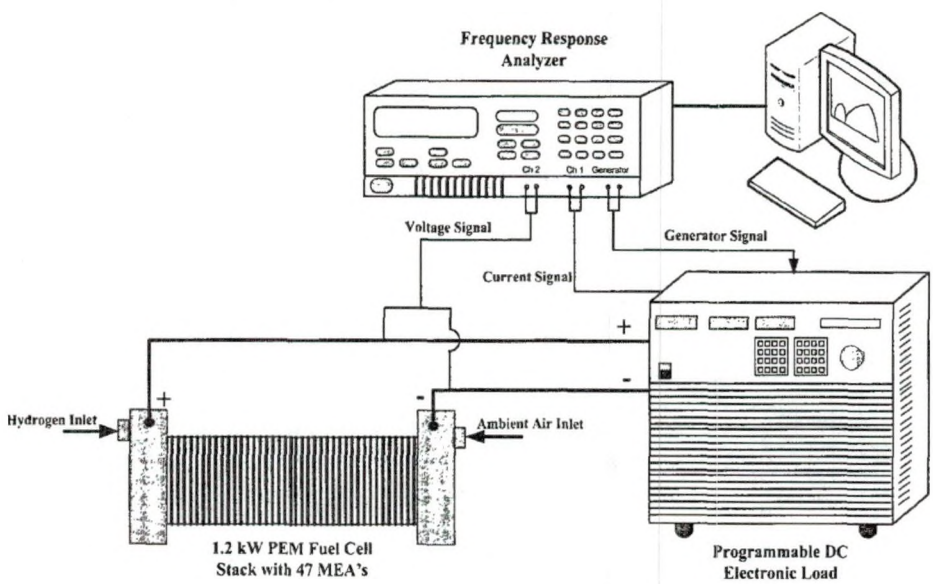

Figure 5: Experimental set up for ac impedance study of 1.2 kW PEM fuel cell

The experimental setup for whole stack is depicted in Figure 5. The impedance data was collected using a Solartron 1250A frequency response analyzer (FRA) [43] and a Chroma 63203 programmable DC electronic load [44]. The Solartron 1250A FRA has a frequency range from 10μHz to 65 kHz. The Chroma DC electronic load has a frequency range upto 20 kHz. The impedance spectrum was recorded by sweeping frequencies over the range of 20 kHz to 50 mHz with 10 points per decade. Each sweep represents one set of data, spectra, and takes about 11 minutes to complete. The EIS experiments were carried out in galvanostatic mode which is the usual mode of fuel cell operation. Current control is easier than voltage control with commercial electronic loads [41,45].

An AC signal with a DC offset was generated by the FRA which modulated the current from the fuel cell stack using a programmable DC load. The response voltage and current were measured for impedance calculations. The current measured at the electronic load is sent to channel 1 and the voltage measured across the stack or group of cells is sent to channel 2 of FRA. The appropriate normalization factor was used to scale the current signal from the electronic load for impedance calculations. Collected data and generated impedance data by the FRA is plotted and analyzed using Zplot® and Zview software programs [46].

The EIS measurements for groups of cells and single cells at different locations in stack were carried out by measuring voltage directly across the group of cells or single cells while current was measured at the electronic load. In case of fuel cells with embedded control, the stack temperature reaches and/or maintains a certain value at a particular current (eg. ~32.7 °C at 5 Adc or ~42.5 °C at 15 Adc). Before each measurement the fuel cell was operated for at least an hour at a particular current to allow

the system to reach steady state. Running the fuel cell at other current levels can result in different stack temperatures. EIS measurements at temperatures different from its steady state value results in impedance spectra which exhibit a different behavior of the electrode processes than its steady state behavior.

At moderate load levels, the load wires connected to the stack can have significant magnetic fields which introduce inductive artefacts at high frequencies of the impedance spectra [27]. For this study, these effects were minimized by making good connections, spirally winding the current carrying wires connected to the load, using equal length coaxial cables connected to the FRA. The effect of current carrying load wires on the high frequency loop and on the high and low frequency intercept loop was clearly observed and is discussed in Chapter 4.

3.3 EIS Studies of PEM Electrolyzer

EIS is a popular analytical tool whose results can be correlated with complex variables such as mass transport, charge transport, rates of chemical reactions, corrosion, dielectric properties, and the effect of composition on the conductance. Very little work has been performed using EIS to analyze PEM electrolysis stacks because power supplies of required rating lack the wide frequency bandwidth required to conduct full range EIS studies. The primary limitation is a power supply able to generate the high level of DC required to run the electrolysis stack at full load (140 Adc at 50 V) while applying the test AC signal (at least 5–10 % of the DC current at 0.01 to 20 kHz) required to perform the EIS analysis. Existing power supplies are typically restricted to either low current applications at the required frequency, or limited frequency range at the required current.

EIS studies of the PEM cell stacks require a frequency response analyzer (FRA) supplying modulating signal to a DC power supply. The DC power supplies a base current and small AC perturbations are imposed on the PEM cell stack. The resulting voltage is measured and analyzed using a FRA for different frequencies. In absence of an off–the–shelf DC+AC power source capable of supplying desired AC test signal with DC offset up to the rated 140 A DC, the EIS study of a 6 kW PEM electrolyzer stack was a challenging task to complete. Three different power supply setups, namely low frequency setup, middle frequency setup and high frequency setup were used to obtain the impedance data for whole frequency range (0.01 Hz to 20 kHz). To obtain the low frequency impedance data, an existing Xantrex switching DC power supply was slightly modified by replacing some of the capacitors responsible for filtering the output with much smaller capacitors. With less filtering, it produces a small AC signal with a DC offset. For middle frequency range, off–the–shelf DC+AC power source with frequency range from 15 Hz to 1 kHz can be used. However, these power supplies are limited in current approximately to 30 A. To achieve the rated electrolyzer current of 140 A, these power supplies can be connected in parallel. The high frequency set up involves a toroid core as a current transformer. These power supply setups used to perform EIS tests of the electrolyzer stack are explained below.

Low Frequency Power Supply Setup

In AC impedance studies of PEM cells, low frequency is the most interesting and least understood frequency range. Mass transport losses and inductive effects, if present, can be observed at low frequencies. The initial goal was to perform the EIS tests at frequencies as low as 0.01 Hz to get a better understanding of the electrolyzer stack at

these lower frequencies. An existing Xantrex programmable DC power supply capable of supplying 60 V and 100 Adc was modified. Four 3300μF capacitors filtering the DC output of switching power supply (PS 1) were replaced with two 12 pF capacitors as shown in Figure 6. A small AC signal with DC offset generated by the FRA was sent to the programming lines of switching power supplies to output an AC current with a DC offset. The switching power supply scales its output according to the input signal from the FRA. If an input AC signal of 1 V peak to peak with a 5 V DC offset is supplied to the programming lines, then the power supply outputs a 10 A AC with 50 A DC offset. The frequency range achieved with this setup was from 0.5 Hz to 20 Hz. At the targeted lower frequency of 0.01 Hz the response of the switching power supply was found very noisy.

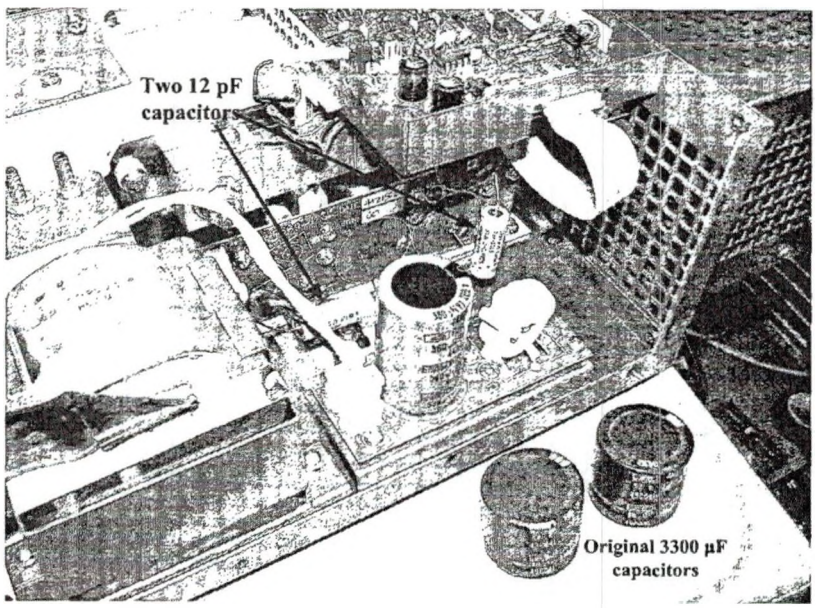

Figure 6: Capacitors replacement for PS 1

As the modified switching power supply is capable of supplying upto 100 A DC, EIS tests with this setup are limited to 85 A with AC signal of 10% of DC current. To

achieve the rated current of electrolyzer of 140 A, the other switching power supply can also be modified similarly and connected in parallel with already modified power supply (PS 1). With this setup, the EIS tests can be performed at rated current over a frequency range of 0.5 Hz to 20 Hz.

Middle Frequency Range Power Supply Setup

The mid frequency range from 20 Hz to 1 kHz can be achieved by a power supply such as the Chroma 61605 [44]. The Chroma 61605 and Agilent 6813B [47] have a capability of supplying AC power with DC offset required for EIS tests of an electrolyzer. However, these power supplies are limited in current range. The Chroma 61605 is limited in the current range upto 30 A. Agilent 6813B has a limited frequency range from 45 Hz to 1 kHz and current range upto 13 A rms. Among these, Chroma 61605 offers better current and frequency ranges. The electrolyzer EIS tests can be performed using Chroma 61605 only upto 27 A DC with AC signal of at least 5 % of the DC current. EIS tests of a 6 kW electrolyzer with this power supply will result in approximately 20% of its rated current (140 A) and will not shed light on important electrochemical processes and losses occurring at high currents. Using only one Chroma 61605 power supply is not expected to give much information about mass transport losses in a 6 kW PEM electrolyzer which are generally occur at high current densities.

Since the commercial power supplies have current rating of 30 A, three of these can be connected in parallel to achieve the maximum current of 90 A. With three power supplies in parallel, EIS tests upto 80 A are possible with AC perturbation of at least 5% of the DC value. Approximately 57% of the electrolyzer rated current (140 A) is achievable with this setup which may not again result in fruitful information about the

high current losses in the electrolyzer. The limited current can be overcome by connecting more than three commercial power supplies in parallel to achieve the rated current. However, personal conversation with Chroma engineers suggested not to put more than three power supplies in parallel as they may not work correctly.

A programmable AC source such as Chroma 61612 has capability of supplying AC current with DC offset upto 70 A. However, these power supplies are huge (approx. 6 ft tall) and costly (approx. $ 41,000). Two of these power supplies in parallel can fulfill the rated current requirement for EIS tests of a 6 kW electrolyzer stack.

High Frequency Range Power Supply Setup

A toroid current transformer was used to perform the high frequency EIS experiments for the electrolyzer stack. Figure 7 shows the basic toroid transformer core setup and the desired specifications. On the primary side of the core, an amplified AC signal from the signal generator and amplifier is connected to one end and other end is grounded. The DC power supply is connected to the secondary side winding and the other end of the winding is connected to the resistor as a load. The AC signal generates a changing magnetic field in the core of the transformer which causes the DC current to oscillate according to the AC signal. The pure DC at the one end of the secondary winding results in DC with AC perturbation as shown in Figure 7. An amplified AC signal should be large enough to cause the correct amplitude of perturbation on the DC. An AC signal amplitude on the primary side is different for different DC current levels. The perturbation of DC also depends on the turn ratio of primary winding to secondary winding.

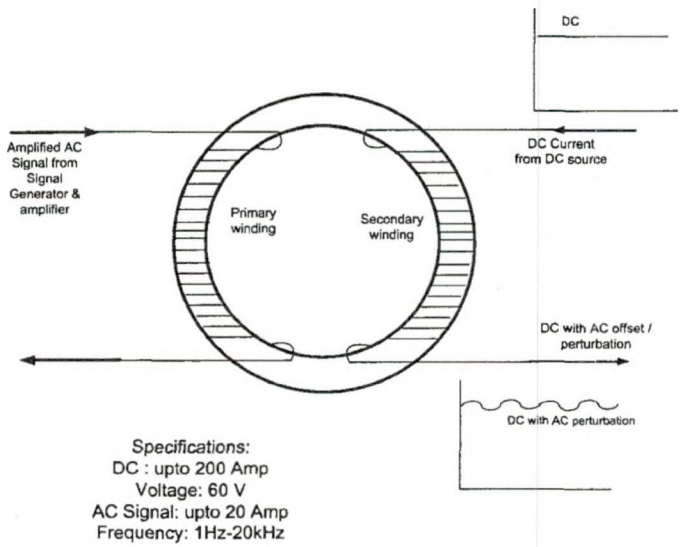

Figure 7: Transformer core specifications

A prototype of this system was tested using a linear DC power supply and MPP type toroid core for a base DC up to 1 A with AC signals up to 0.02 A superimposed on the DC. The system generated output observed on the oscilloscope showed no visual distortions over the frequency range from 300 Hz to 4 kHz. The same toroid was used for high current tests upto 40 A using thicker wire (4 AWG) as shown in Figure 8. Beyond 40 A, the wire coating started melting. Thicker wires than 4 AWG were tried, but winding the core with the thicker wire was very difficult without help of special tools. During these tests it was found that winding the wire on the core by hand is not good practice, and resulted in higher core losses. The main problem was the current running through the primary side winding and the number of turns of 1 AWG wire on the secondary winding. Only about twenty turns of the 4 AWG cable could fit around the transformer core. The primary winding needed a resistance around 1 Ω which requires a high number of turns. When a similar number of turns on each winding were used, the resistance was to low on the primary side to operate the core properly.

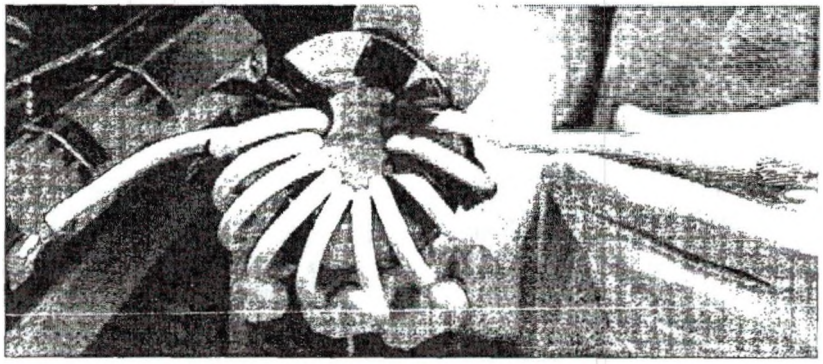

Figure 8: Self-wound prototype toroid core with 4 AWG wire

It was expected that with better winding and a different core material with better magnetic properties, a wider higher quality frequency response could be obtained as compared with the prototype setup. A frequency range from 100 Hz to 20 kHz was expected with the better core material and winding having same design as shown in Figure 7. The winding and design work was outsourced to a commercial transformer designer [48] with the specifications mentioned in the Figure 7.

High current tests upto 65 A were performed using the custom built transformer core, Xantrex power supply, FRA and resistor to ensure its performance. After performing the preliminary tests, the custom built transformer was setup with the electrolyzer system as shown in Figure 9. The primary windings of the transformer are connected across the output of an Audiobahn A2300 HCT audio amplifier [49]. An AC signal with DC offset generated by FRA is an input to the 2400 W audio amplifier. The amplifier is then set to achieve the required amplification of the input AC signal. On the secondary side winding of the transformer core, a cable connects to the Xantrex DC power supply and an electrolyzer stack. A 1 AWG cable connected to the positive output terminal of Xantrex programmable DC power supply (PS 1) wound on the secondary side

of the transformer core with only one turn was connected to the electrolyzer as shown in Figure 10. The amplified AC signal on the primary side generates the desired DC perturbation. This DC current with AC signal on top of it delivered to the electrolyzer on the other side of the secondary winding.

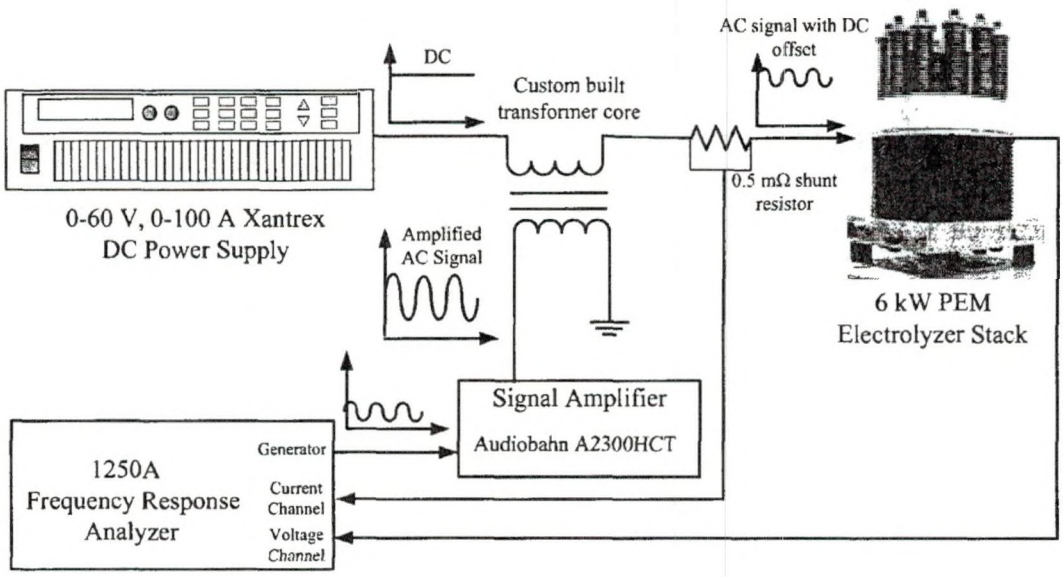

Figure 9: High frequency EIS experimental setup using transformer core for 6 kW PEM electrolyzer

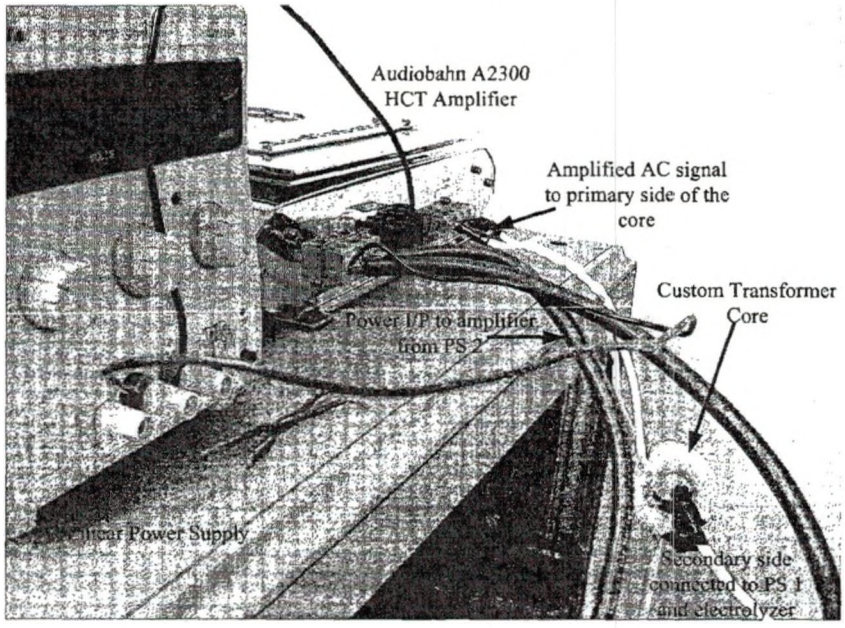

Figure 10: Actual setup for custom transformer core for high frequency EIS tests.

As one of the existing power supplies was modified for low frequency EIS setup, the remaining Xantrex power supply was used for the high frequency setup. For all EIS power supply setups for the electrolyzer, the stack voltage is measured directly across the stack and input into the voltage channel of FRA. The stack current is measured across the 0.5 mΩ shunt resistor to converts the current signal into voltage which is then input to the current channel of FRA. The impedance data is then analyzed using Zplot and Zview program.

CHAPTER 4

RESULTS AND DISCUSSIONS

4.1 PEM Fuel Cell Experimental Results

PEM fuel cell performance is highly dependent on the stack temperature. The products of the fuel cell reaction are electricity, water and heat. The heat emitted due to the exothermic reaction of a fuel cell increases the fuel cell temperature. The heat output is proportional to the rate of reaction, hence is a function of the load current. The PEM fuel cell stack temperature increases with the load current as shown in Figure 11. The PEM fuel cell stack was run for 10 minutes at each load current mentioned in Figure 11 to study the temperature rise behavior of the PEM fuel cell stack. It was observed that the stack temperature becomes stable and does not raise much after 10 minutes. The initial stack temperature depends on the ambient temperature, so care was taken to keep the same starting temperature at all load currents. The starting temperature for these tests was approximately 26.8 °C. The stack temperature was found to increase rapidly for the first 3 minutes. The stack temperature increased from approximately 33 °C at 5 A to 65 °C at 40 A after 10 minutes. The results from these tests helped to determine the steady state operating temperature for the EIS tests of PEM fuel cell stack discussed in the later part of this chapter.

Operating temperature plays an important role in determining the performance of a PEM fuel cell. The higher temperature helps overcome the activation barrier for the fuel

cell reaction resulting in lower voltage losses. At the same current density, with less voltage losses, the fuel cell stack produces more power at elevated temperatures.

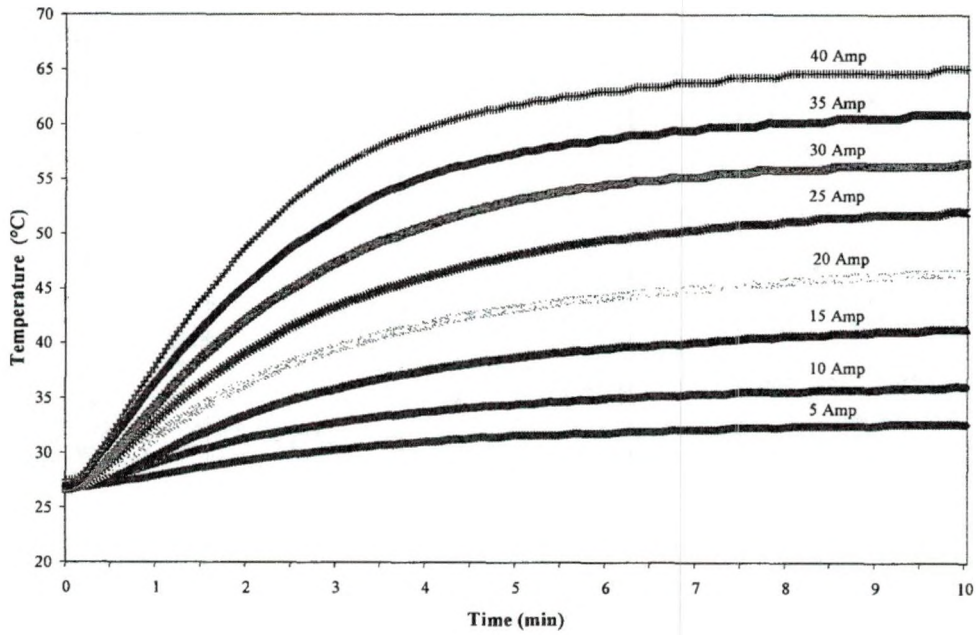

Figure 11: Temperature rise of PEM fuel cell stack at different load currents for the first 10 minutes

I-V data for the 1.2 kW PEM fuel cell at different temperatures is shown in Figure 12. The Nexa™ fuel cell system has an embedded control which imposes difficulties to control of the operating parameters such as temperature and reactants flow rates externally or manually. From the tests conducted previously (Figure 11), the steady state temperature values at particular current density were known. To collect the I-V data at 40 °C, the stack was run at 20 A for some time to achieve 40 °C. As soon as the stack temperature reached and stabilized at 40 °C the fuel cell load current changed to the value of interest to measure the stack voltage at that load current and 40 °C . Loading the stack with lower currents decreases the stack temperature. Therefore, the stack was again loaded at 20 A to bring the stack temperature back to 40 °C and again the voltages were

recorded at the next load current of interest. The same procedure was repeated to obtain the I-V data at 50 °C and 60 °C. The I-V data at lower temperatures were attempted, but maintaining the low stack temperature at higher current levels was found difficult even with the help of external fan cooling.

As can be seen from Figure 12, at all the current levels, the stack voltage is higher at higher temperatures. At no load current, the stack voltage has increased from 41.2 V to 42. 2 V as stack temperature increased from 40 °C to 60 °C. This verifies the increase in the exchange current density (i_o) with increasing temperature. The drop in the cell voltage at the lower exchange current density is explained by Butler-Volmer equation [18]. From these results, it can be predicted that operating at lower temperatures results in lower fuel cell voltages.

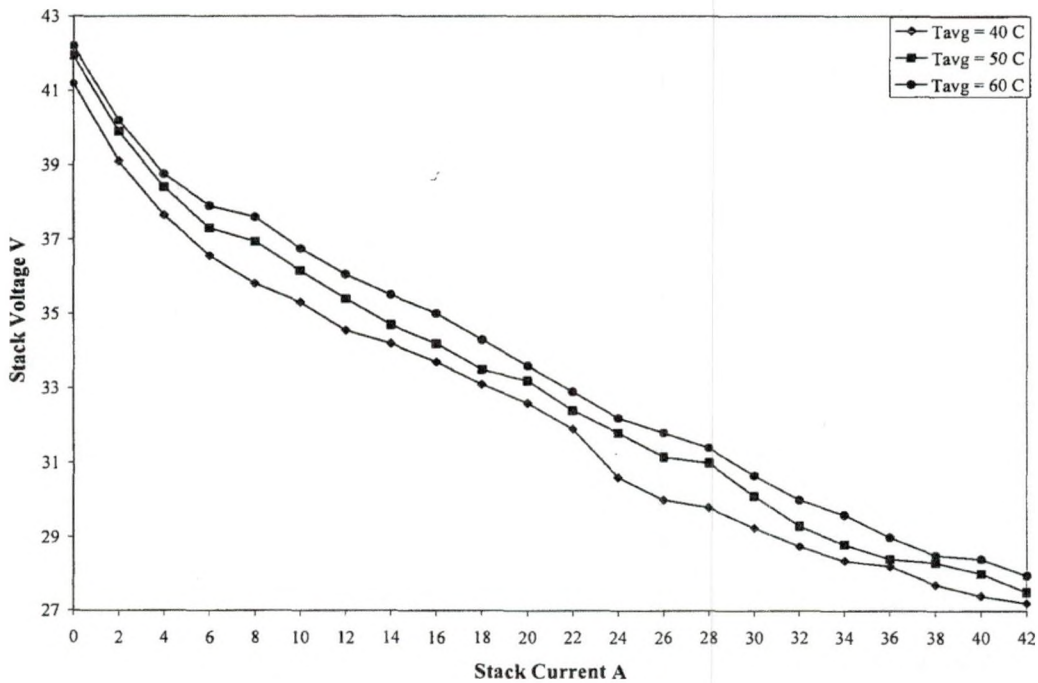

Figure 12: Effect of stack temperature on IV characteristics of 1.2 kW PEM fuel cell stack.

4.2 PEM Fuel Cell EIS Results and Discussion

Impedance data for a 1.2 kW PEM fuel cell were obtained using the EIS experimental set up described in section 3.2 of the previous chapter. Impedance data were plotted as Nyquist and Bode plots for analysis of fuel cell losses and to study its behavior at different loading conditions. The Nyquist plot is a popular technique to evaluate impedance data. In a Nyquist plot, the imaginary part of complex impedance is plotted against the real part at each excitation frequency. Using Nyquist plots, typical impedance spectra exhibit three semicircle loops as shown in Figure 13. Generally, a high frequency loop starts from 20 kHz to 5 kHz. Two overlapping loops can be observed in medium frequency region which starts from 5 kHz to 1Hz. These overlapping loops correspond to anode activation losses and cathode activation losses. At high currents, a third loop can be observed in the low frequency region which represents the mass transport losses. As shown in Figure 13, normally, the cathode impedance is significantly larger than the anode impedance and the cathode impedance can mask the anode impedance [50]. In some cases, anode impedance can be observed as a smaller high frequency loop. However, the high frequency also appears as result of effect of the external artefacts on impedance measurement. This loop should not be confused with the anode impedance loop. The small high frequency loop due to external artefacts is clearly shown in Figure 13.

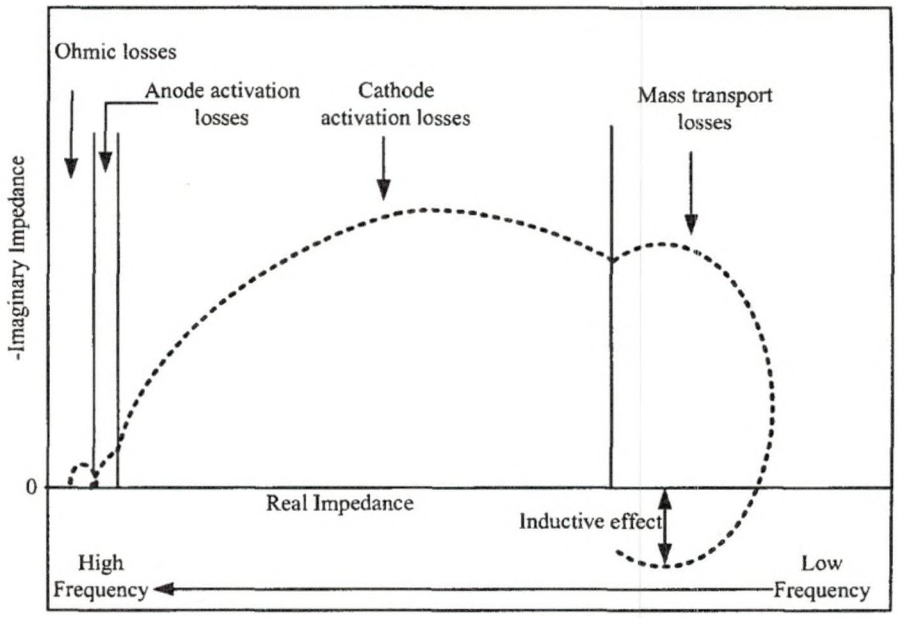

Figure 13: Typical Nyquist plot for PEM fuel cell showing all four losses

The frequency dependence of impedance can be shown by a Bode plot. Impedance magnitude and phase angle Bode plot are shown in Figure 14. The Bode plot has advantage over Nyquist plot for impedance data at higher frequencies. The higher frequency response gets bunched together in Nyquist plot whereas the Bode plot allows studying the higher frequency response better. The Bode magnitude plot is helpful in determining the polarization resistance at different frequencies. At higher frequencies ohmic resistance dominates the impedance and can be estimated from the high frequency horizontal region. At low frequencies, the impedance read on the magnitude axis is the sum of activation and ohmic polarization. The impedance magnitude at higher current reaches the peak value at lower frequencies and then decreases again, which represent the inductive effect.

The Bode phase plot clearly explains the capacitive or inductive behavior of PEM cell at different frequencies. The vertical axis for phase plot is a negative phase angel, so

a phase angle below zero on vertical axis represents the inductive behavior (positive phase angle) and above zero represents the capacitive behavior (negative phase angel). Sometimes, the phase angel plot can be below vertical axis at lower and higher frequencies representing the inductive effects of a PEM cell at those frequencies. At very high frequencies, the phase angel can be zero showing the purely resistive behavior. In general, the Bode plot provides better description of the PEM cell's frequency dependent behavior than the Nyquist plot.

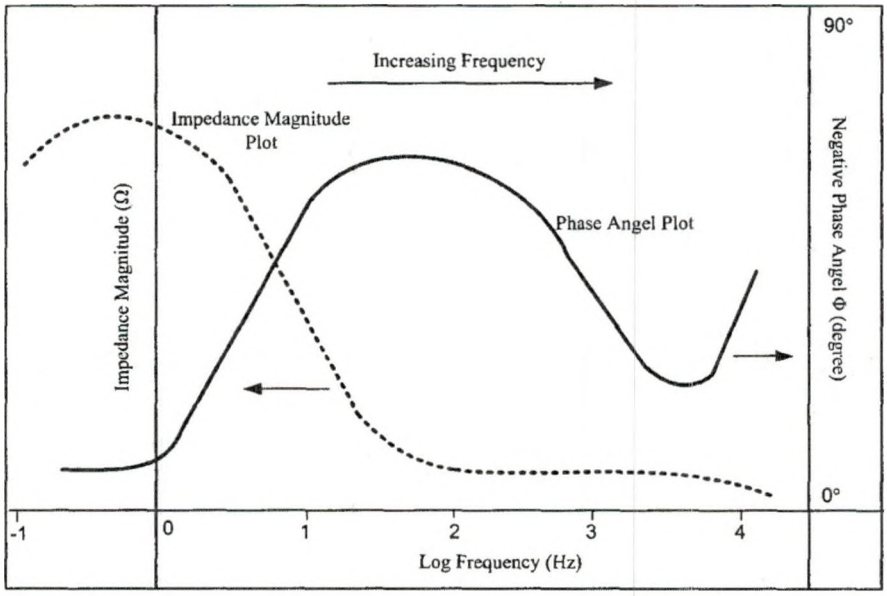

Figure 14: Typical Bode magnitude and phase plot for PEM fuel cell

Nyquist and Bode plots were analyzed for ohmic, activation and mass transport losses at various loading conditions for the whole stack, groups of cells and single cells at different positions in the stack. The effect of the AC amplitude signal, load wiring and stack run time on impedance data are also discussed in the following sections.

4.2.1 Amplitude Selection for Fuel Cell EIS Tests

Selection of the optimal AC signal amplitude is important in fuel cell EIS experiments to obtain a good impedance spectrum. For accurate EIS measurements the

perturbation signal has to be sufficiently small, in the ranges of 5–10 mV peak to peak [51]. However, small AC signals cause minimal perturbation at higher currents which causes difficulties in measuring the response. Without an electrochemical interface to remove the DC offset of the measured current and voltage response, the FRA can not distinguish between noise and response. For EIS experiments of a PEM fuel cell stack at higher currents, a higher AC perturbation is desirable. Wagner et al. [41] used a 200 mA AC signal superimposed a on 5A DC for their study. Jaouen et al. [25] used AC signal amplitude of 5% of the DC current. X. Yuan et al. [45] also obtained good impedance spectra for AC amplitudes of 5%, 10% and 15% of the DC current. X. Yan et al. [42] used an AC signal amplitude of 10% of the DC current in their impedance study of a 2 kW PEM fuel cell stack. For the present study, tests were conducted to obtain impedance spectra at AC amplitudes of 1% to 5%, 7.5%, 10% and 15% of the DC current. The aim was to find the optimal AC signal amplitude. Effects of these AC signals on impedance spectra for a 10 Adc study are shown in Figure 15. All the EIS tests for a 10 Adc were conducted after running the fuel cell stack for one hour at 10 Adc. The same experiment was repeated for different DC current values to confirm the results obtained for 10 Adc. Though 5% and 7.5 % AC amplitude signals resulted in good impedance spectra for 10 Adc, the response was very scattered for low load currents. Also, the impedance spectrum for a 1% AC signal amplitude was very scattered because the perturbation caused by the 1% AC signal was small, making it difficult for the FRA to distinguish between noise and response. Based on results shown in Figure 15, an AC amplitude signal of 10 % of the DC current resulted in a good impedance spectrum for the whole stack current range of

interest. All the remaining EIS tests for the PEM fuel cell stack study were conducted using AC signal amplitude equal to 10 % of the DC currents.

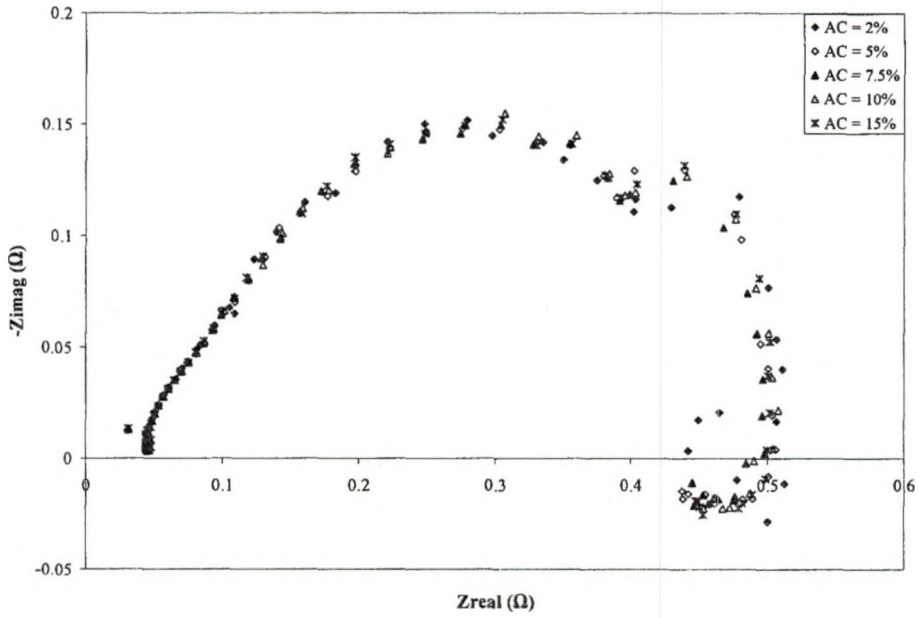

Figure 15: Effect of AC signal amplitude on EIS spectra for 42 cells Nexa stack at 10 Adc

4.2.2 EIS Measurement at Various Stack Run Time

The system under study must be at steady state throughout EIS measurements [28]. It is a common practice to run the fuel cell for some time to achieve steady state before starting each EIS measurement. In this work, efforts were made to find the time for the PEM fuel cell stack to achieve steady state. EIS measurements were taken at intervals of approximately 20 minutes to observe the impedance spectra. Tests were conducted at 0, 20, 40, 60 and 90 minutes during the stack run time. Each test takes approximately 11 minutes to perform at the experimental conditions as explained in the experimental details. The stack was operated at the DC test current continuously in between these tests. As can be seen in Figure 16, the middle and low frequency

impedance loop gets larger as stack run time is increased. A difference between impedance plots at middle and low frequency was observed for the data measured at the beginning (0 minutes) and after 60 minutes as shown in Figure 16. This shows the importance of stack run time when measuring the impedance. Data taken at early stack run times, before the system has a chance to come to equilibrium, can lead to misinterpretation of the data and invalid conclusions. Little difference was observed between the impedance data measured after 60 and 90 minutes of stack run time for the 10 Adc current test with AC signal amplitude of 10 % of the DC current. The same results were obtained for various current levels which verify that for this work, the fuel cell stack has to run for at least one hour before taking EIS measurements.

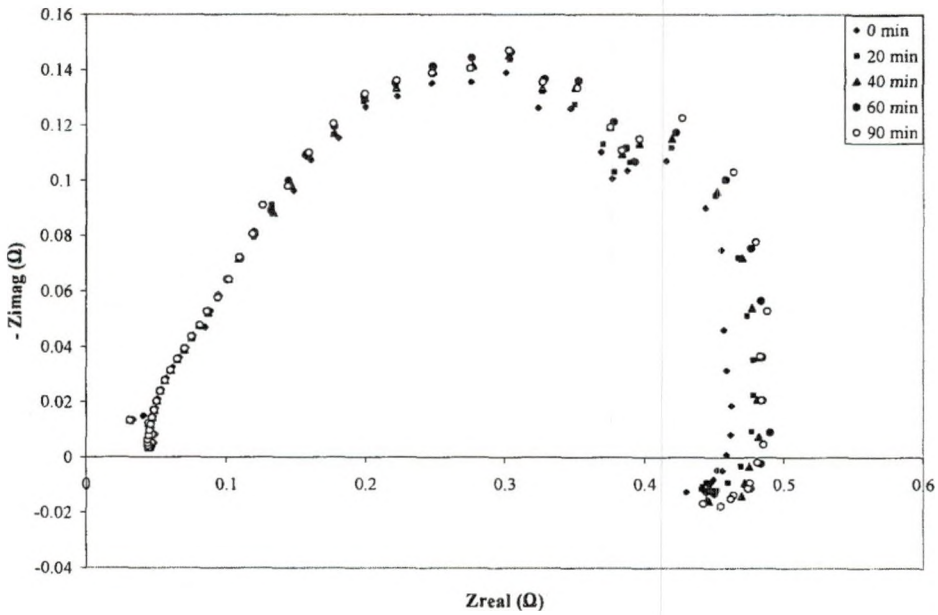

Figure 16: Impedance data recorded at different stack run time for 10 Adc with AC signal of 10 % of DC.

4.2.3 Whole Stack Impedance Data Analysis

The impedance of a 47 MEA stack was measured using the FRA and DC electronic load at different current levels. For this work, two characteristics loops were observed at low load currents (1 Adc – 4 Adc) as shown in Figure 17. The high frequency intercept with the real axis represents the ohmic resistance. The ohmic resistance can be expressed as a sum of contributions from contact resistances and ohmic resistance of cell components. Resistance of cell components includes the ohmic resistance of the membrane, catalyst layer, bipolar plates and contact resistance between them. A small difference was observed in the ohmic resistance of the whole stack with increased currents. The reason for this change may be that at higher currents the membrane was well hydrated. Membrane resistance is the main contributor to the ohmic resistance, and a well hydrated membrane results in a low resistance value at any load.

The smaller first high frequency loop (20 kHz to 5 kHz) was insensitive to current. Researcher's have attributed this high frequency loop to the structural features of the MEA [52], internal ohmic resistance, and the electrode's contact capacitance due to its structure [53] and to the measurement circuits [28]. This high frequency loop is discussed in detail in the later part of this chapter.

Generally, in PEM fuel cells, the cathode activation losses are dominant relative to anode activation losses. This can be attributed to slower kinetics of the oxygen reduction reaction at the cathode and is evident by the large middle and low frequency loop (1 kHz to 0.05 Hz) on the impedance plots such as Figure 17. The changing behavior of the middle frequency loop (1 kHz to 2 Hz) as a function of current is also related to the double layer capacitance within the catalyst layer combined with charge

transfer resistance of the ORR. The charge transfer resistance determines the diameter of this loop. Dependence of charge transfer resistance on electrode potential is given by the Tafel equation [54, 55]. As shown in Figure 17, the diameter of the middle frequency loop decreases at high currents. The third loop representing mass transport losses appeared at 5 Adc and more.

Inductive effects also appeared at high currents and low frequencies. The possible reason suggested by Makharia et al. [56] for this inductive behavior is the side reaction and intermediates involved in fuel cell reactions. However, this low frequency inductive behavior can also be attributed to the time required to make measurements at low frequency, or, to the nonstationary behavior of the fuel cell. The impedance model developed by Roy et al.[57] to account for the reaction mechanism that may be responsible for the inductive response at low frequencies, proposes the formation of hydrogen peroxide as an intermediate in a two step ORR. Antoine et al. [58] showed that the adsorption step involved in ORR of the fuel cell gives rise to this inductive behavior.

The polarization resistance at 1 Hz (i.e. 0 Hz on Log scale) changed from 1 Ω at 1 Adc to 0.38 Ω at 15 Adc as can be seen from Figure 18. The impedance magnitude matched closely at high frequencies and started deviating at approximately 10 Hz (i.e.1 Hz on Log scale). The impedance magnitude showed a continuous increase at low frequencies for current levels of 1 Adc to 4 Adc. However, a change in the shape of the impedance magnitude plot at lower frequencies (< 2 Hz) was observed for 5 Adc and higher. Beyond 5 Adc, the impedance magnitude, after reaching a peak value, started decreasing. This corresponds to the inductive effect observed in the Nyquist plot (Figure

17). The Bode phase plot shown in Figure 19, clearly shows this change in impedance behavior at low frequencies to inductive starting from 5 Adc.

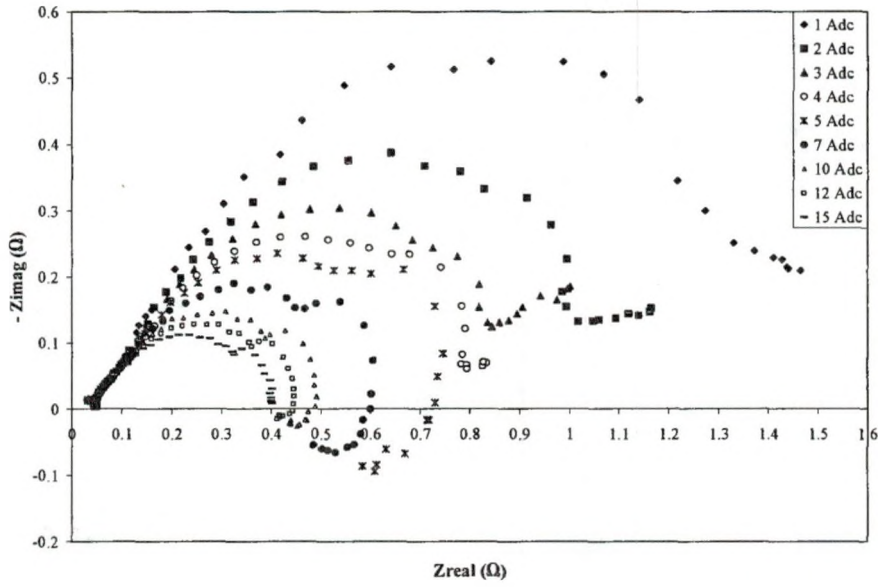

Figure 17: Current dependence of Nyquist plot for the current range 1 Adc to 15 Adc with ac signal amplitude of 10% of DC

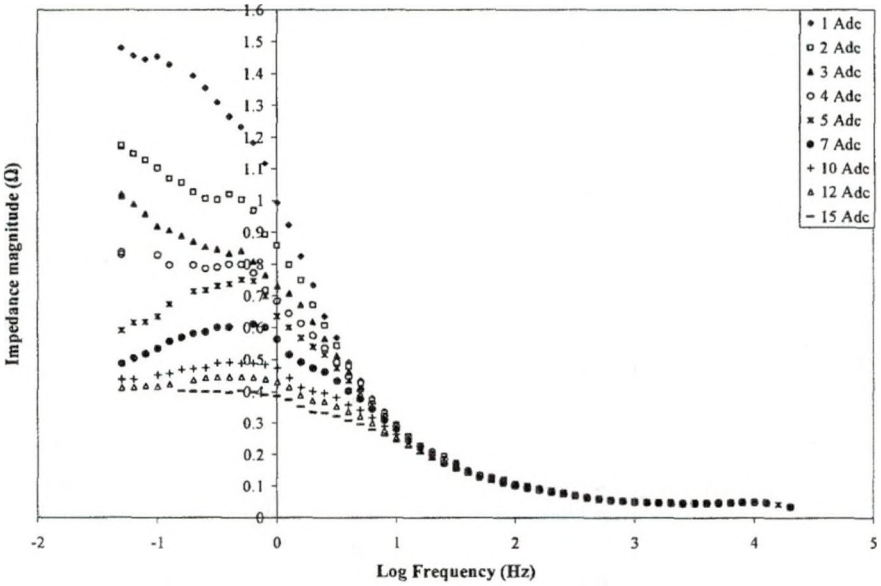

Figure 18: Bode magnitude plot for current range 1Adc to 15 Adc with AC signal amplitude 10% of DC current

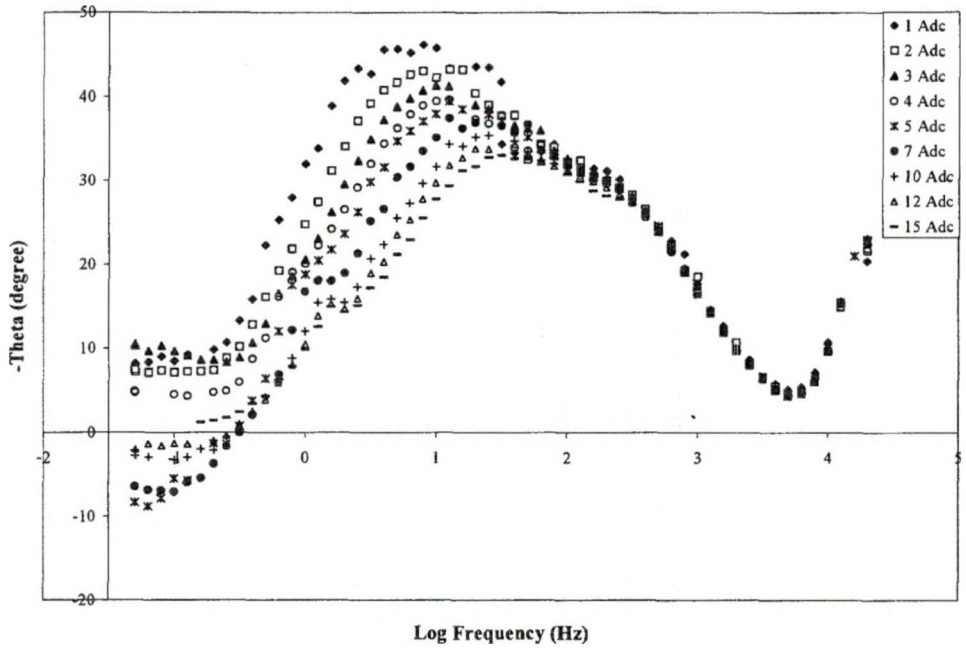

Figure 19: Bode phase plot for current range 1 Adc to 15 Adc with AC signal amplitude 10% of DC

To achieve a high output power, the fuel cell runs at high current densities. However, at high current densities the mass transport losses become more significant. Figure 20 shows the impedance data at high currents (20 Adc - 40 Adc). The mass transport loop gets larger as current increases. The inductive nature of these loops also increases at higher currents. The increased mass transport losses at higher currents can be reduced by modifying the operating conditions such as using a higher reactant flow rate [59]. Chu et al [60] have operated a fuel cell at more than 20 times the stoichometric flow rate. However, in the case of the commercial fuel cell used for this study, the oxidant air flow rate increases in proportion with the current. Therefore an increase in the mass transport losses due to low oxidant air flow rate may not be the reason in case of a commercial fuel cell such as Nexa™. A possible explanation is the accumulation of water in the flow channels of flow fields creating a diffusion layer opposing the oxygen

transport to the electrode. Another explanation for this third low frequency loop is the effect of liquid water formed at the cathode, which affects the transport of oxygen and the hydration effects that limit the water transport in the membrane [61]. Paganin et al. [62] attributed this third low frequency arc to the water transport characteristics in the membrane.

Figure 20 shows that the third arc of the low frequency loop increased in size when current increased from 25 Adc to 40 Adc. However, the size of this loop decreased when current increased from 15 Adc to 25 Adc. At 35 Adc this mass transfer loop was the biggest. Water diffusing through the membrane from the cathode to the anode side increases with the load current. However, at higher current densities, close to rated current, a significant amount of water reaching anode is transported back to the cathode by electro-osmotic drag. The size of the third arc may depend on which one of the water diffusion and electro-osmotic drag mechanisms dominate the process at that current density.

A Bode magnitude plot for high currents is shown in Figure 21. At currents beyond 25 Adc, the impedance magnitude reached a peak at a frequency of approximately 0.63 Hz (i.e. -0.20 on Log scale) and then started decreasing. This decrease corresponds to the inductive effects at low frequencies in the Nyquist plot (Figure 20). Because of higher mass transport losses at higher currents, the magnitude of the peak impedance increased from 30 Adc to 40 Adc. The value of impedance magnitude for higher currents (35 Adc-40 Adc) was very close to that of the low current range of 12 Adc to 15 Adc due to higher mass transport losses.

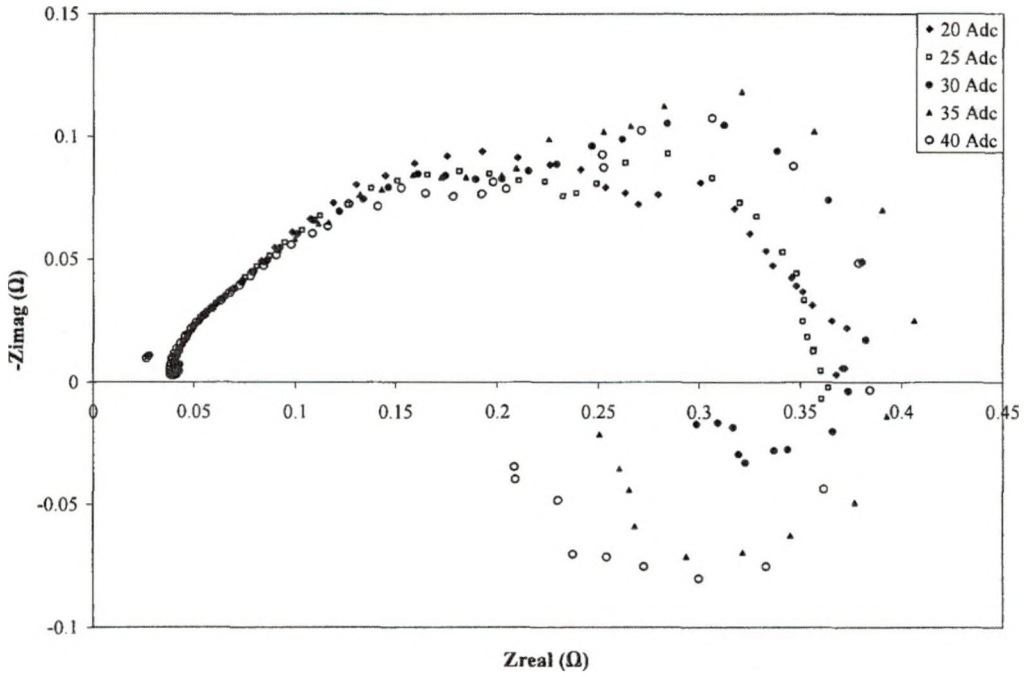

Figure 20: Current dependence of Nyquist plot for current rage 20 Adc to 40 Adc with ac signal amplitude of 10% of DC

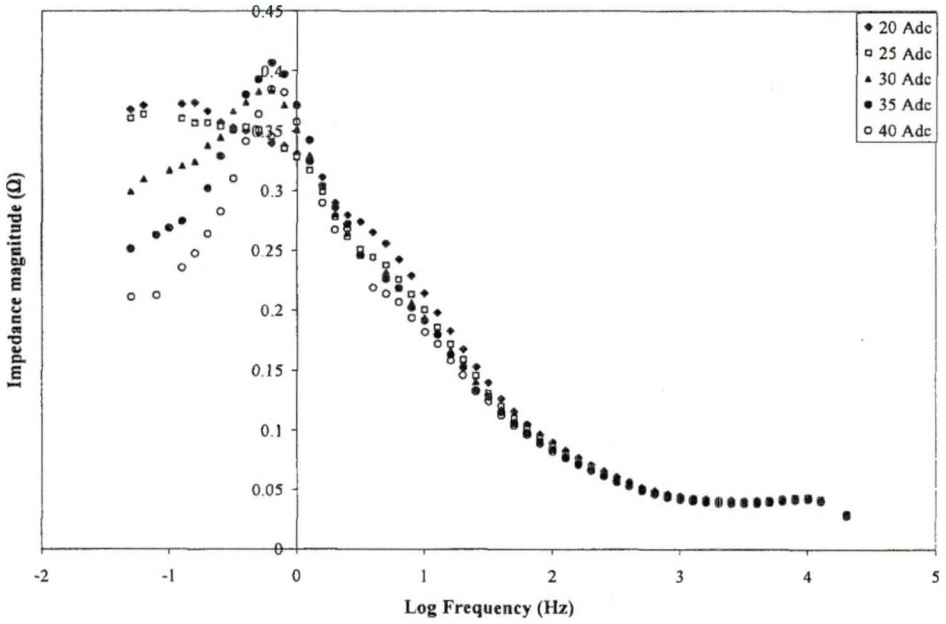

Figure 21: Bode magnitude plot for current range 20 Adc to 40 Adc with AC signal amplitude 10% of the DC

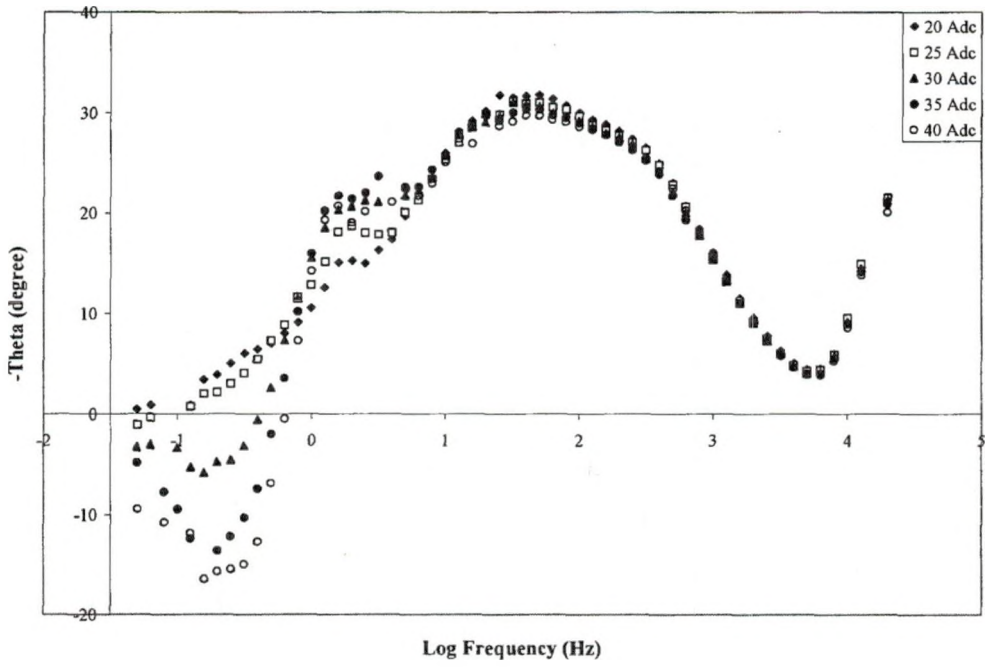

Figure 22: Bode phase plot for current range 20 Adc to 40 Adc with AC signal amplitude of 10% of the DC

Figure 22 shows the Bode phase plot for current range from 20 Adc to 40 Adc. The increase in the positive phase angle with increasing current reflects the increase in inductive effect. The phase angle is near zero for 20 Adc indicating resistive behavior at low frequencies. The probable reason is that at 20 Adc, the diffusion of water from cathode to the anode side is balanced by the water transport by electro-osmotic drag from anode to the cathode.

4.2.4 Group of Cells Impedance Analysis

Several groups of ten cells each were selected starting from the air inlet to investigate the effect of cell position in the stack on impedance data. The cells were numbered from the air inlet side starting from 1. Figure 23 shows the impedance plot for several groups of 10 cells at different location in the stack. For this investigation, a 10

Adc load current was drawn with an AC signal amplitude of 10% of the DC load current. As can be seen from Figure 23, cells located at hydrogen inlet have less impedance than cells located at air inlet side. Not much difference is observed at the high frequency region. At high frequencies, the impedance is mainly resistive. However, at low frequencies, a change is observed in both polarization resistance and the capacitive component from the hydrogen inlet to air inlet side cells. The ohmic resistance did not change much with the cell positions in the stack. Its average value was approximately 9 mΩ for a group of ten cells compared with 41 mΩ for the whole stack.

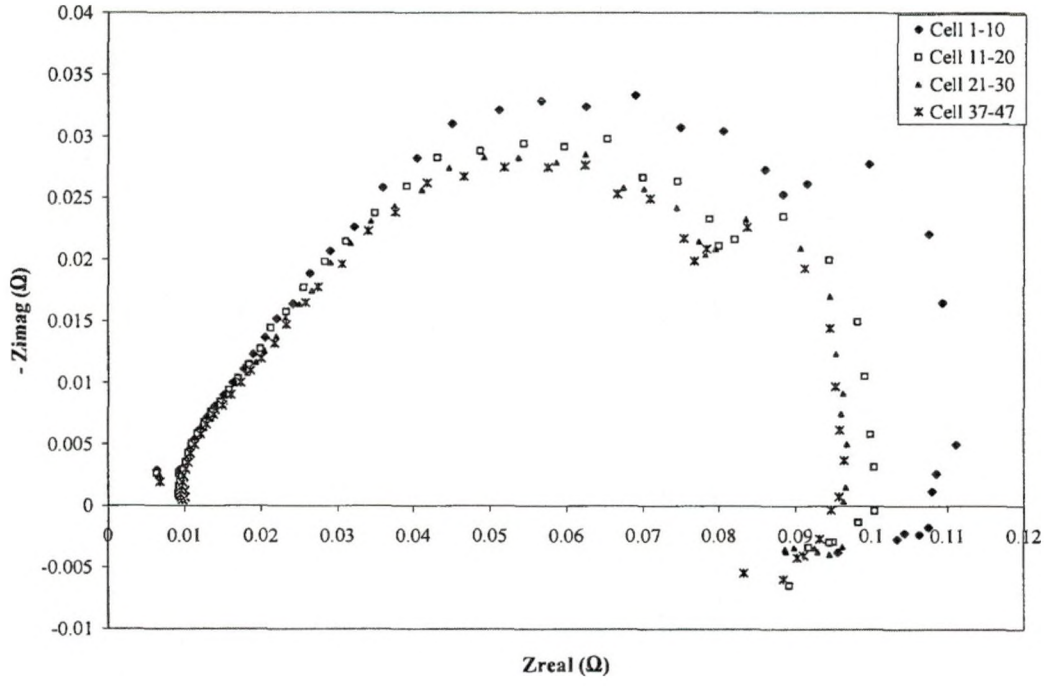

Figure 23: Nyquist plot for group of ten cells at different positions in stack

As shown in Figure 24, all the selected groups of ten cells had the same impedance magnitude at high frequencies. The group impedance values started separating at 100 Hz and continued till 0.05 Hz. At 1 Hz, the impedance magnitude of the group of

cells # 1–10 located at the air inlet side was 17 mΩ higher than that of cells # 37–47 located near the hydrogen inlet. This may be attributed to different values of the double layer capacitance for each group. At high frequencies the impedance magnitude matched closely for different groups of cells. The deviation at low frequencies increased as the capacitive component of the impedance increased.

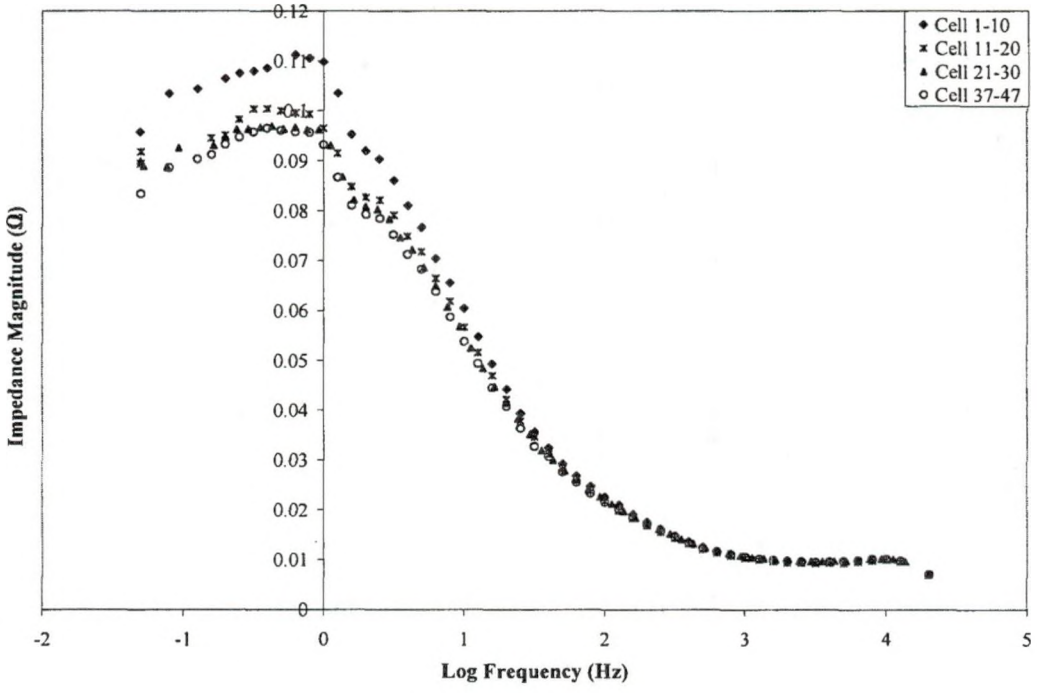

Figure 24: Bode magnitude plot for group of ten cells at different positions in stack

The reason for change in the polarization resistance at low frequencies as observed in the Nyquist (Figure 23) and Bode magnitude plot (Figure 24) with cell positions in the stack is not clear at this point. If a temperature gradient across the stack has caused this change, then the membrane resistance should have also changed. Membrane resistance is a function of temperature and the main contributor to ohmic resistance. However, no changes were observed in the ohmic resistance. One possible

reason for the polarization resistance change with position may be attributed to the non-uniform distribution of current density along the stack.

To further investigate the impedance behavior of cells located at the hydrogen and air inlet side, EIS tests were conducted on two groups of five cells at each end of the stack. Based on the results obtained for group of ten cells at different positions in the stack, the impedance of cell # 1 – 5 was expected to be higher than that of cell # 42 – 47 as shown in Figure 25. The change in polarization resistance from 47 mΩ to 64 mΩ was observed for the group of five cells at the air inlet and the hydrogen inlet side of the stack respectively. The non uniform current density distribution may be the cause of this change in the polarization resistance. The exact reason is unknown at this point.

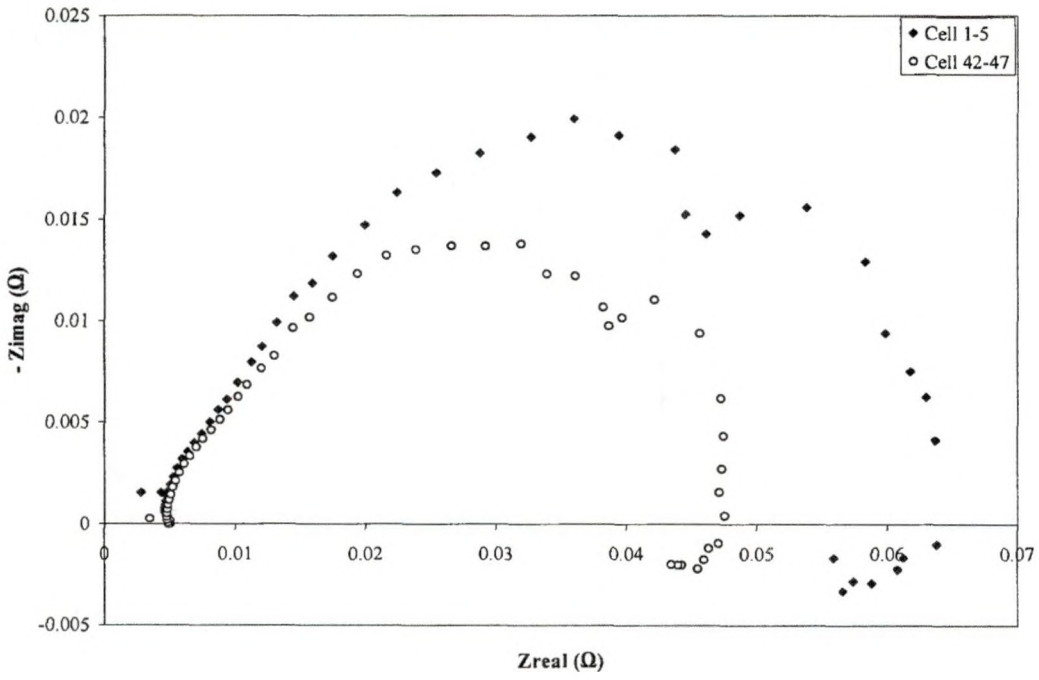

Figure 25: Nyquist plot for group of five cells at either end of fuel cell stack

The effect of increasing the number of cells in a group on impedance spectrum can be seen in Figure 26. EIS testing was started from the air inlet side with a group of first five cells. The numbers of cells in the group were increased from 5 to 10, 20, 30 and 40 starting from the same first cell (cell #1). Both the ohmic and polarization resistances increased from cell # 5 to cell # 40. The ohmic resistance increased approximately from 4 mΩ for group of cell # 1 – 5 to 37 mΩ for group of 40 cells (cell# 1 – 40) as shown in Figure 26.

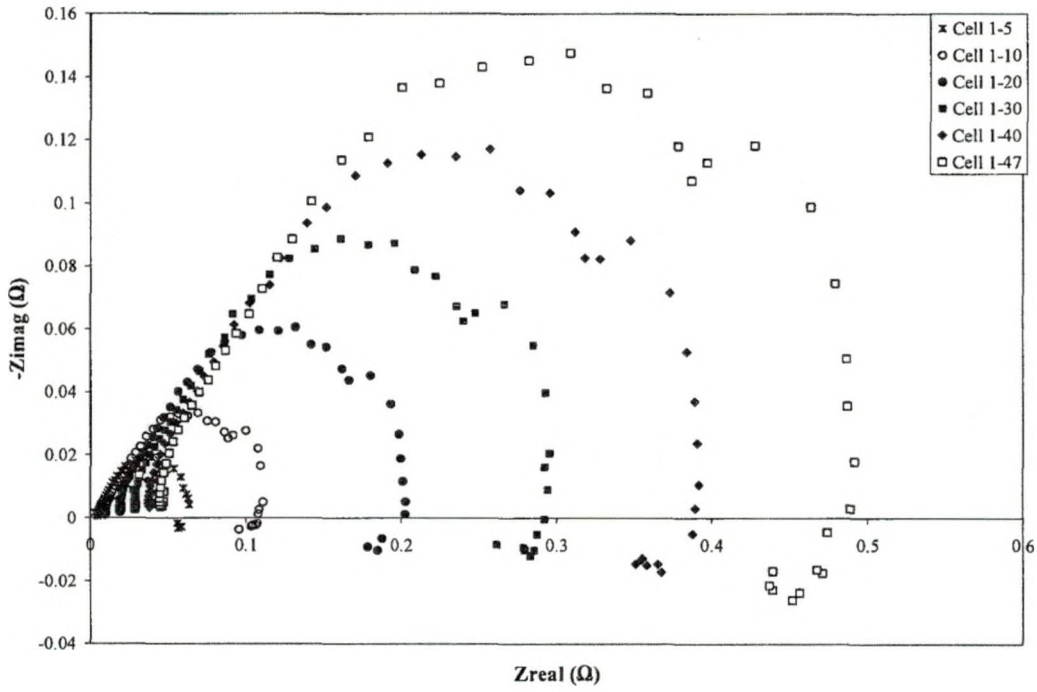

Figure 26: Nyquist plot for group of cells starting from cell # 1

With an increase in the number of cells in a group, polarization resistance is expected to increase. The polarization resistance, measured at 10 Adc with AC signal amplitude of 10 % of DC, was increased from approximately 64 mΩ for a group of the first five cells (cell# 1 – 5) to 390 mΩ for the group of 40 cells (cell# 1 – 40). The polarization resistance for the whole stack (cell# 1 – 47) was approximated to be 488

mΩ. The polarization resistance increased approximately by same amount when number of cells in a group increased by 10 cells. However, the low frequency inductive effects were increased with increasing number of cells in a group. From the previous tests (Figure 23) for a group of cells, it was observed that the inductive effects at low frequency are higher for the cells located near the hydrogen inlet side. The same results can be seen from Figure 26: low frequency inductive effects were increased as we move closer to the hydrogen inlet side. The possible reasons for this low frequency inductive behavior are discussed earlier in this chapter (section 4.2.3). The reason for these inductive effects at low frequency may not be the time required to make the impedance measurements. The probable reason can be the side reactions and intermediates involved in the fuel cell reaction as suggested by Makharia et al. [56]. At the hydrogen inlet side, plenty of hydrogen is available for the reaction so the possibility of side reactions and formation of intermediates is higher than at the air inlet side where the hydrogen is less. EIS studies of single cells located at the hydrogen and air inlet side can reveal this behavior.

The frequency dependence of the polarization resistance for a group of increasing number of cells can be seen from Bode magnitude plot as shown in Figure 27. The difference in the impedance magnitude is observed at all frequencies with increasing number of cells in the group. The difference was small at higher frequencies. However, significant difference can be seen at lower frequencies. With increasing number of cells in a group the impedance magnitude is expected to increase. The impedance magnitude at 1 Hz (i.e. 0 Hz on Log scale) has increased from approximately 57 mΩ to 473 mΩ when number of cells in a group increased from 5 to 47 beginning with same cell (cell #1).

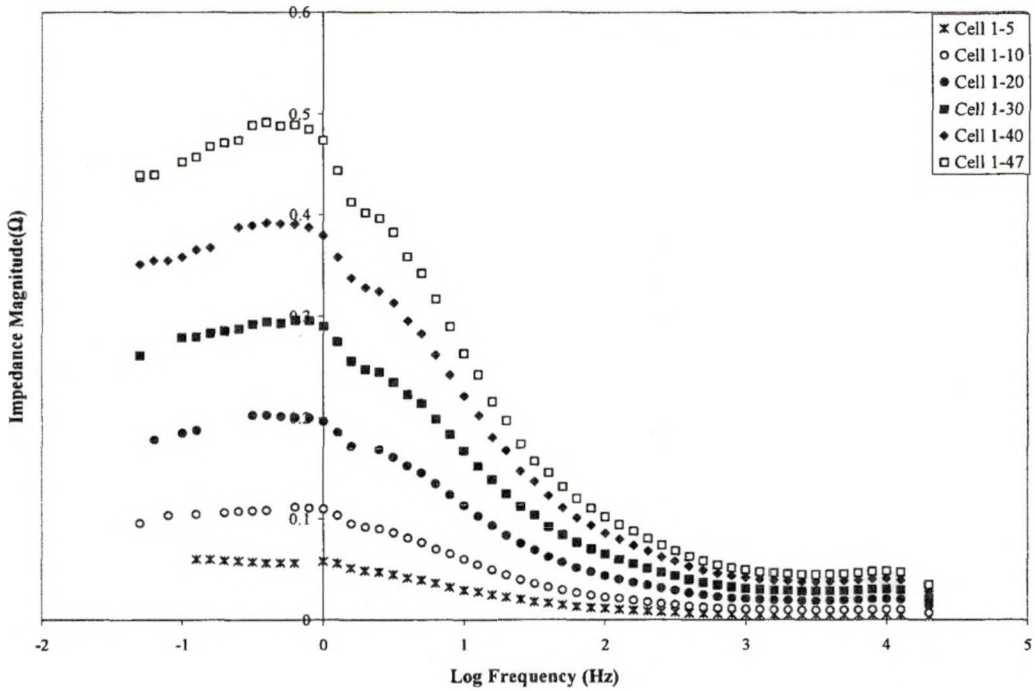

Figure 27: Bode magnitude plot for group of cells from the cell#1 located near to the air inlet side

4.2.5 Single Cell Impedance Data Analysis

Impedance data were taken for single cells located at different locations in the stack at 10 Adc and an AC amplitude signal of 10% of DC current. Cells are numbered from the air inlet side. The observed changes in the impedance spectra for the single cells are shown in Figure 28. As expected from the group of cells impedance study, cells located near the air inlet side showed a higher polarization resistance than cells located near the hydrogen side. The polarization resistance changed from 15 mΩ for cell # 1 to 10 mΩ for cell # 47 which is located nearest to the hydrogen inlet. The possible reason for this may be hydrogen scarcity at the air inlet side cells as they are located far from hydrogen inlet side, or non uniform distribution of the current density. A high frequency inductive behavior was observed for single cells located near the hydrogen inlet.

However, this high frequency inductive behavior was absent for the whole stack tests presented earlier. This inductive effect decreased towards the air inlet side where the high frequency loop started appearing. Thus, at high frequency, the inductive reactance turned into a capacitive reactance from the hydrogen side to the air side cells.

Cells located near the air inlet showed a much large high frequency loop than cells near the hydrogen side. Since the test protocol was the same for all cells tested, the difference noted between cells confirms that the high frequency loop is not solely due to external artifacts, MEA structure, or internal ohmic resistance. Anode activation may contribute to the magnitude of this loop. The scarcity of hydrogen at the air inlet side may result in higher anode activation losses for the cells located near it. I-V data showed better performance for cell # 47 compared to cell #1 which also confirmed the different behavior of these cells. If the high frequency loop were only the result of external artifacts, MEA structure, or internal ohmic resistance, then all the cells should have shown similar loops. Only the cells located near air side resulted in the high frequency loop. The high frequency loop observed for the whole stack (Figure 17 and 20) and groups of cells (Figure 23) is likely the result of contributions from the cells located near the air inlet side

The average ohmic resistance for a single cell was approximately 1 mΩ. The value of the ohmic resistance for a group of 10 cells was approximately 9 mΩ compared to 41 mΩ for the whole stack. The ohmic resistance value of individual cells sums up closely to the whole stack ohmic resistance which agrees reasonably well with the fact that cells are connected in series. Cell # 1, nearest to the air inlet, is the first of all cells that is humidified before entering the stack has the lowest ohmic resistance with the value

of 0.11 mΩ. The ohmic resistance increased for the cells placed farther away from the humidified air inlet. The ohmic resistance increased from 0.25 mΩ for cell # 5 to 1 mΩ for cell # 47. The obvious reason for the lowest ohmic resistance for cell # 1 is that a well humidified membrane offers good conductivity for protons.

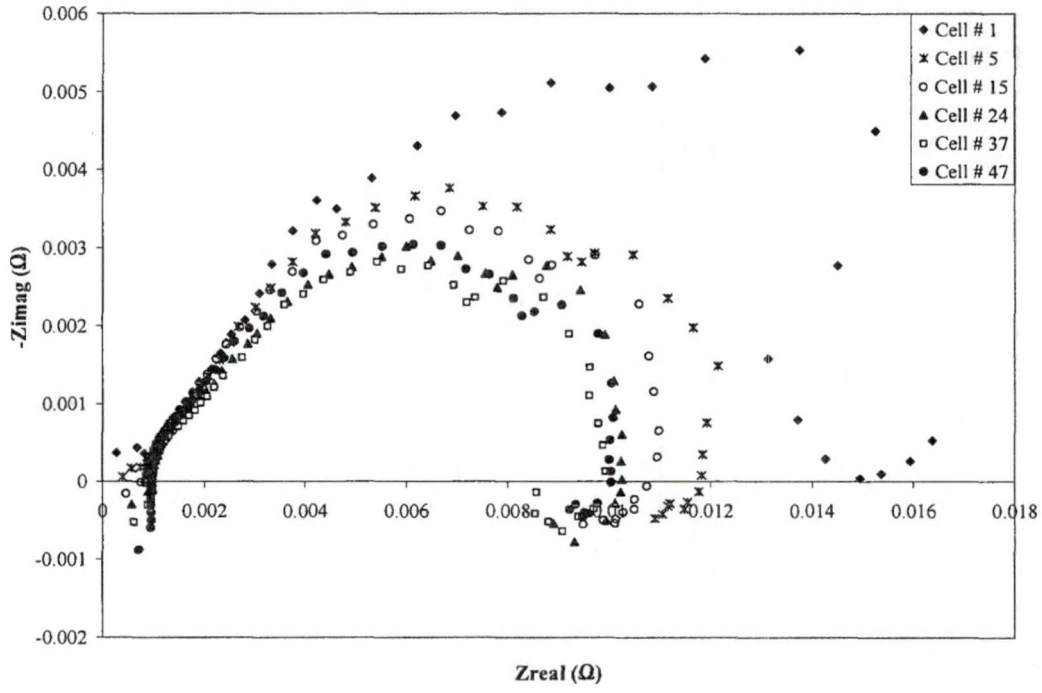

Figure 28: Nyquist plot for single cells at 10 Adc at different locations in the fuel cell stack

In the Nyquist plot (Figure 28), the complex part of the impedance represents the capacitance, and at high frequencies the capacitive reactance is low. The high frequency impedance behavior of single cells at different locations in the stack can be clearly observed in the Bode phase plot as shown in Figure 29. The impedance becomes more resistive as the phase angle gets closer to zero. The positive phase angle at high frequencies for cell #24 through cell # 47 reflects an inductive reactance. However, the cells located near the air inlet showed capacitive reactance instead, seen as negative phase

angles for cells #1 through 15 at the higher frequencies. As discussed earlier, the low frequency inductive effect can be attributed to a two step ORR mechanism and/or the formation of intermediate products in the fuel cell reactions [57, 58].

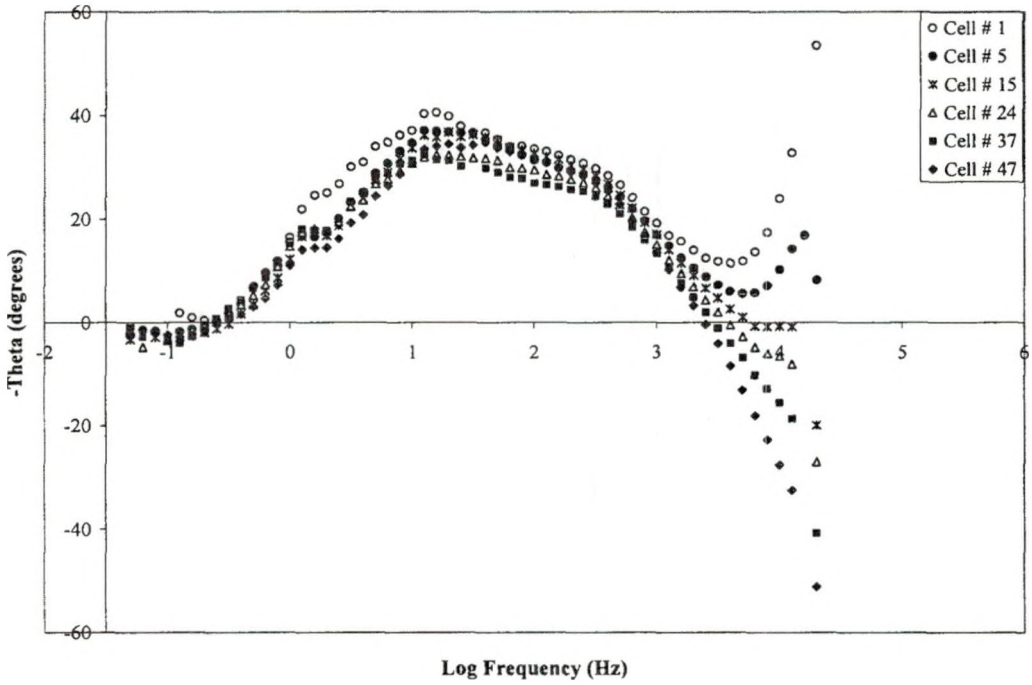

Figure 29: Bode phase plot for single cells at 10 Adc at different locations in the fuel cell stack

Single cell EIS tests were conducted for cell #5, 24 and 42 at various load currents to verify the results obtained for 10 Adc. The purpose of these tests for single cells placed at different locations in the stack is to verify the different inductive and capacitive effects observed at high frequencies for 10 Adc. Figure 30 shows the EIS test for cell # 5 at various load currents. As seen from whole stack EIS tests (Figure 17, Figure 20), PEM fuel cell performs better at high current density and the polarization resistance decreases with increasing current. Similar results were obtained for single cell #5. As load current increased the polarization resistance decreased. Very little change was observed for the ohmic resistance of cell # 5 with increasing current. A small high frequency loop was

observed at all current level for this cell as it is located near the air inlet side. The mass transfer loop first decreased from 5 Adc till 20 Adc then increased with increasing current. The low frequency inductive effects showed the similar trend to that of for whole stack EIS test for various load currents.

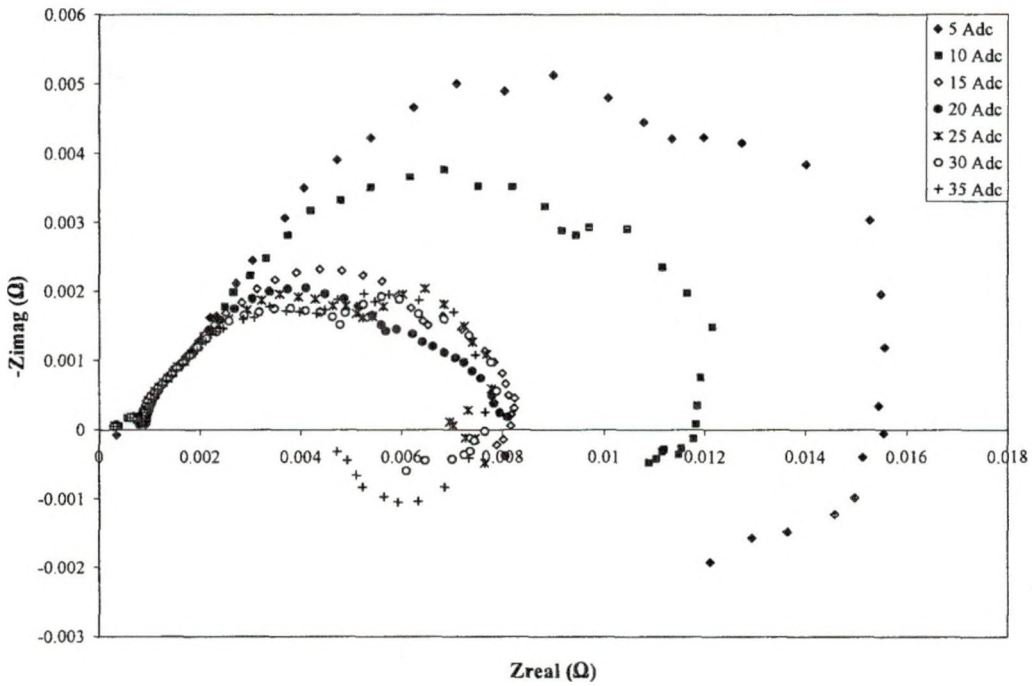

Figure 30: Impedance plot for cell # 5 at various currents

Figure 31 shows the EIS tests for cell # 24, located at the middle of the stack, at various load currents. As can be seen from single cells EIS test at 10 Adc (Figure 28), the high frequency inductive effects appears as we move from air inlet side to the hydrogen inlet side. The high frequency inductive effects were observed instead of small high frequency capacitive loop for cell # 24. The ohmic resistance was almost same for all current levels similar to that observed for cell # 5 (Figure 30). However, the polarization resistance was decreased for the same current when compared to that for cell # 5. At 5

Adc, the polarization resistance for cell # 5 was approximately 15.5 mΩ, compared to 13.4 mΩ for cell # 24. Very little difference was observed in polarization resistance for cell # 24 and cell # 42 for the same load current as shown in Figure 32. The high frequency inductive effects were prominent for cell # 42 at all current levels. These high frequency inductive effects are discussed at the beginning of this section (Figure 28). Very little difference was observed in the low frequency inductive effects for cell # 24 and cell # 42.

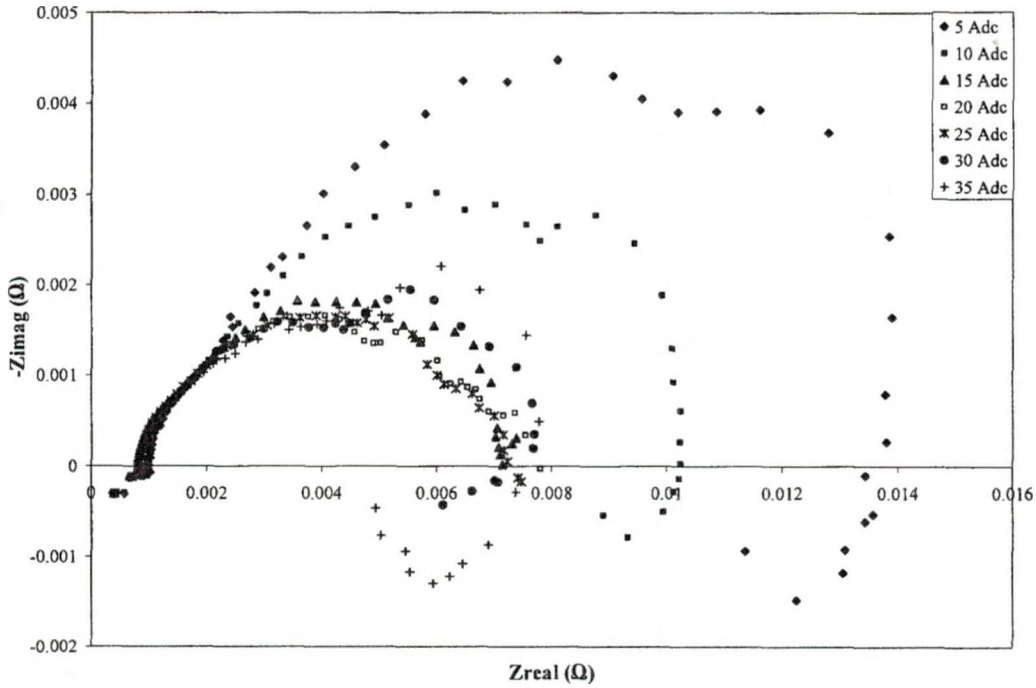

Figure 31: Impedance plot for cell # 24 at various currents

Different high frequency behavior was observed for cell # 1 to cell # 47 at all current levels as explained earlier in Figure 24 – 28. Tests were performed focusing on high frequency behavior for extreme cells located at either end of the stack. Figure 33 shows the high frequency behavior (20 kHz –1 kHz) for cell # 1 and cell # 47 at 10 Adc.

Cell # 1 exhibited total capacitive behavior, whereas cell # 47 showed total inductive behavior. As explained earlier, this behavior changed from capacitive to inductive as cell position moves from air inlet side to the hydrogen inlet side.

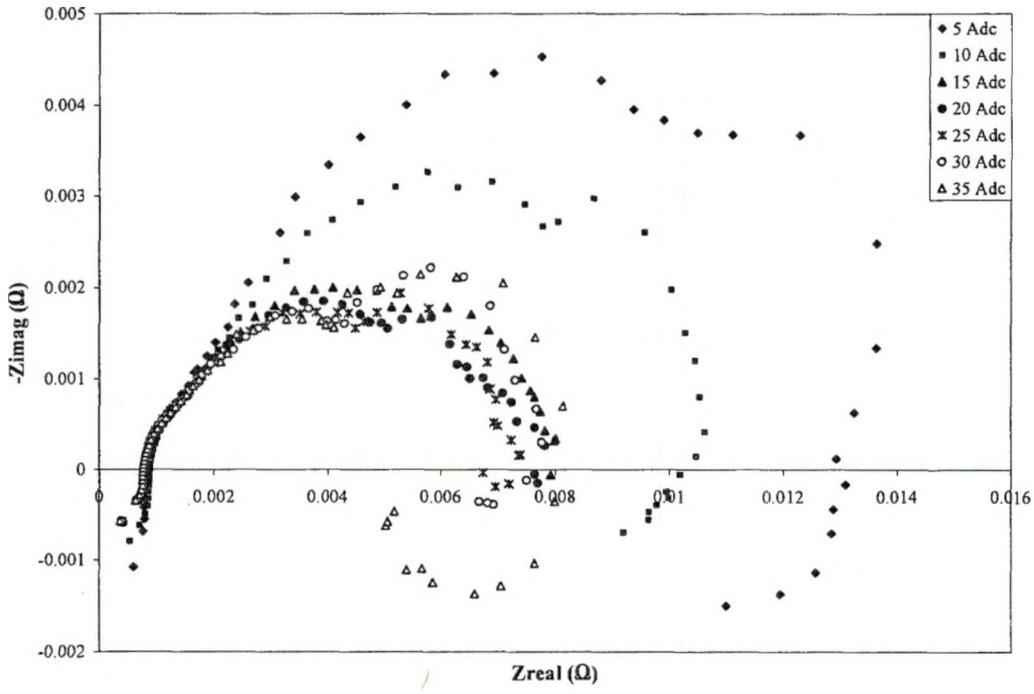

Figure 32: Impedance plot for cell # 42 at various currents

The high frequency behavior of PEM cells is generally attributed to the external artifacts. J.P. Diard et al. [63] concluded that the high frequency inductive behavior is due to the connections and measuring devices. The inductive behavior seen at high frequency is also attributed to the mutual inductance effects of the cables [64]. Had the observed behavior been the result of the experimental setup artifacts, it should have been observed the same for all the cells. However, cells located at different position showed different high frequency behavior.

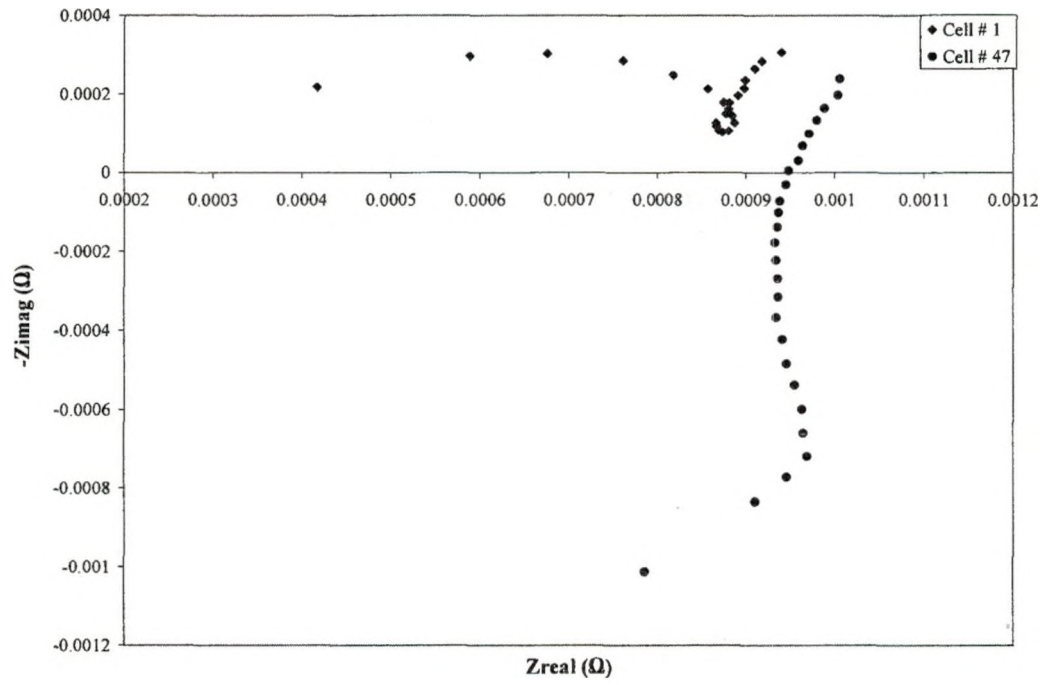

Figure 33: High frequency impedance behavior of single cells located at the extreme ends of the stack at 10 Adc with AC amplitude of 10% of DC

The frequency dependence of the cell # 1 and 47 can be seen in Figure 34. The positive phase difference shows the inductive behavior of the 47th cell. The capacitive behavior of 1st cell is shown by negative phase difference. The anode side reactions may contribute to this high frequency behavior. The major difference in these cells is that plenty amount of dry hydrogen is fed to the anode side of cell # 47 and when it reaches to the anode of cell # 1 it is internally humidified in the fuel cell stack. In addition to this, air fed at the cathode of the cell # 1 is humidified. Thus, it can be assumed that cell # 1 is better humidified than cell # 47, which can be confirmed from the lower ohmic resistance for cell # 1. The amount of hydrogen present at the cell # 1 is lower than cell # 47 as it is located at the opposite end from the hydrogen inlet. To verify the difference between these cells, I-V characteristics were obtained for these cells as shown in Figure 35. With

excess hydrogen, cell # 47 resulted in better fuel cell voltage than cell # 1. In other words, the I-V performance of cell # 47 was found to be better than cell # 1.

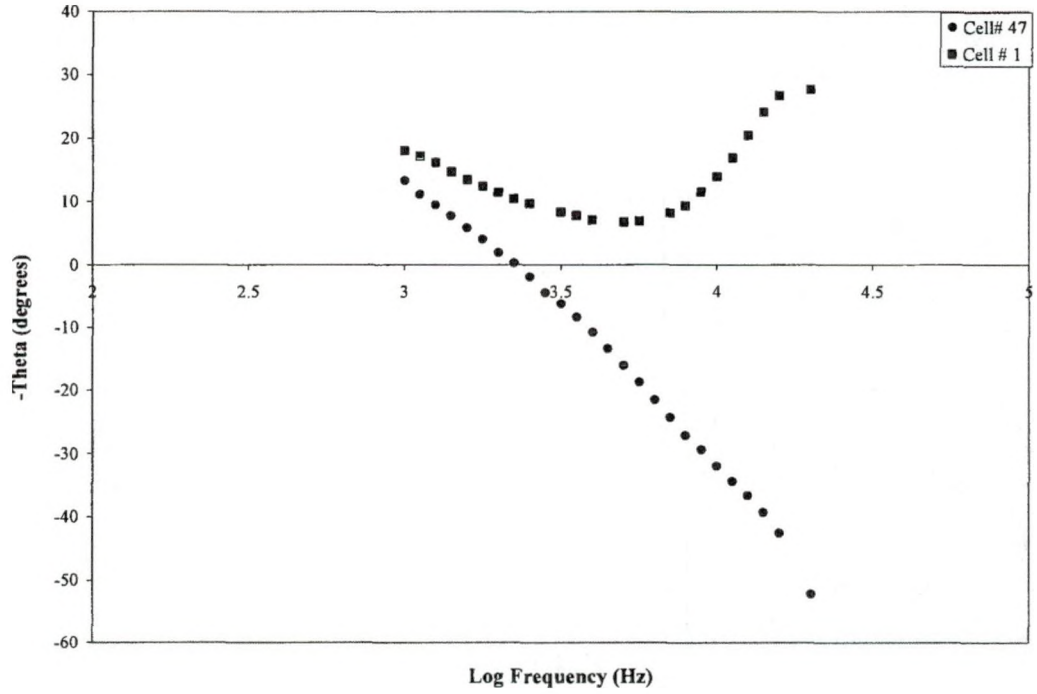

Figure 34: Bode phase plot showing impedance behavior of single cells located at the extreme ends of the stack at 10 Adc with AC amplitude of 10% of DC

The possible reason for this different high frequency behavior of the cell # 1 and 47 can be related to the humidity level of the cells and amount of hydrogen present at the anode side of these cells.

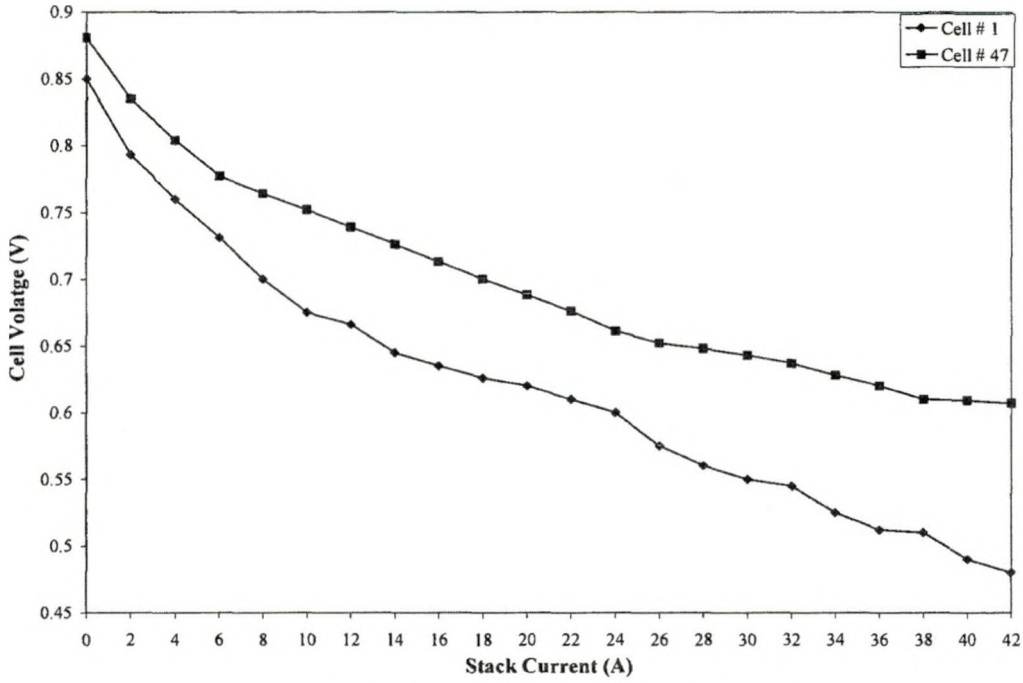

Figure 35: I-V characteristic of Cell # 1 and Cell # 47

4.2.6 Effect of Stack Temperature on Impedance Data

The current voltage characteristics obtained at different temperatures shown in Figure 12 earlier clearly exhibited the different performance of the PEM fuel cell stack with temperature. At higher temperatures the cell voltage was higher because of lower voltage losses than at lower temperatures. The same results were expected for impedance tests at different temperatures. In the case of commercial fuel cells such as Nexa™, temperature control is difficult with the embedded control. The fuel cell stack maintains the certain stack temperature at particular current was shown in Figure 11 and discussed earlier. The EIS measurement at 6 Adc and 10 Adc were performed at respective steady state temperatures and at higher temperatures than steady state as shown in Figure 36. The fuel cell stack was run at higher current to achieve the higher temperature and then the EIS measurements were carried out at 6 Adc and 10 Adc. The stack temperature

decreases during the EIS test to the steady state temperature at that particular current. The EIS measurement takes about 11 minutes to complete. As shown in Figure 36, the polarization resistance decreases with increasing temperatures for both 6 Adc and 10 Adc. At higher temperatures, the activation losses are less than at lower temperatures which results in lower polarization resistances. No difference was observed at higher frequencies at different temperatures. No significant change in the ohmic resistance was observed at different temperatures.

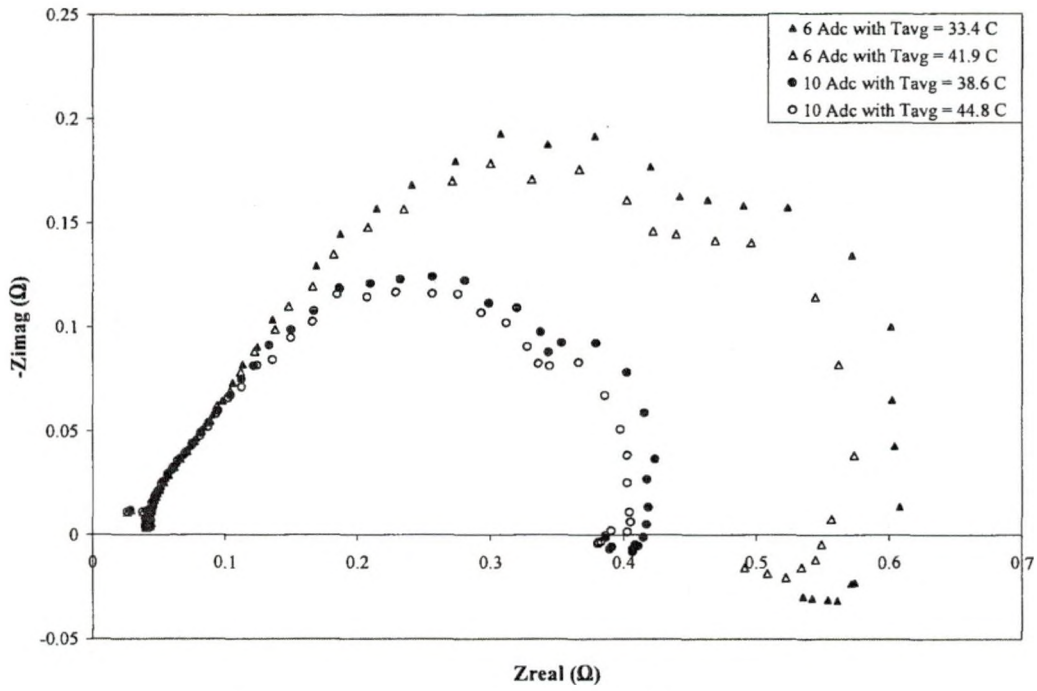

Figure 36: Effect of stack temperature on stack impedance at various currents

4.2.7 Effect of Load Connections on High Frequency Impedance Data

Obtaining good impedance spectra is important in EIS studies. The effects of external wire resistance and connections on impedance spectra are well known. During this study, an effect of load connection wire set up on the high frequency loop was observed. It was observed that when load wires were not wound spirally, the high

frequency loop and the intercept loop of high and low frequency loops were larger (1st set up in Figure 37). The intercept of the high and low frequency loops started shrinking after winding the load wires spirally and making them shorter. The second wiring setup resulted in smaller high frequency loops. It was observed that both the resistive and capacitive impedance components were affected by the load wire setup at high frequencies. No effect was observed on the low frequency inductive behavior from changing the wiring set up. The low frequency inductive behavior is not related to artifacts. Before collecting the final data sets, the load wires connecting fuel cell and the DC load were wound spirally very well and kept as short as possible. The high frequency loop for the final set up was smallest and no change was observed after winding them tighter. This confirms the effect of experimental set up or external artifacts on the high frequency loop. No changes were observed for the low frequency loop, starting from 1 kHz to 50 mHz, with the changes in the load wiring setup. The low and high frequency intercept loops observed from 12 kHz to 1 kHz (typical of EIS spectra) are due to the DC electronic load response to the excitation and/or high frequency artefacts related to the fuel cell structure. This intercept loop needs a more detailed and extensive study.

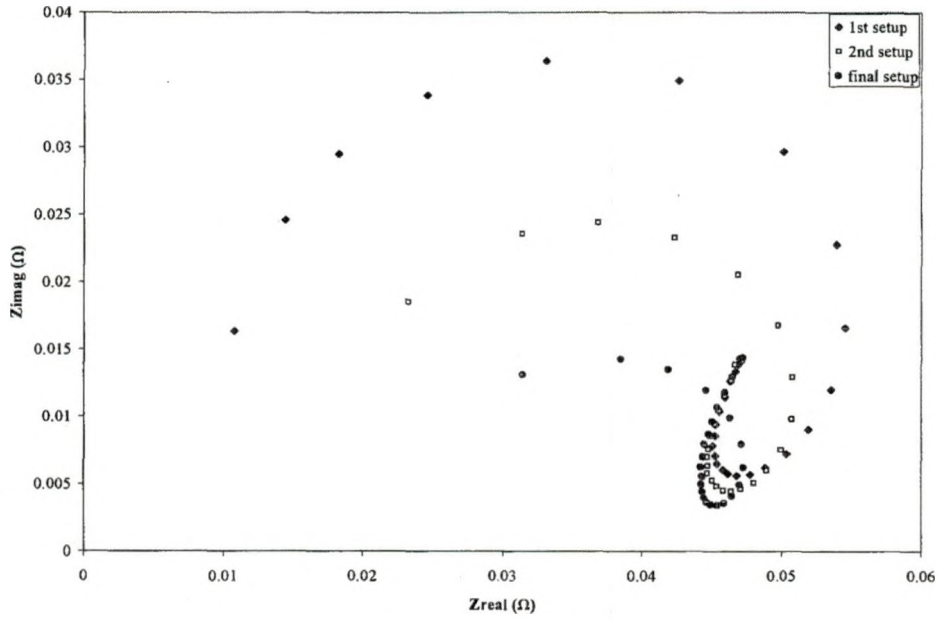

Figure 37: Effect of load connections on high frequency impedance loop

4.3 PEM Electrolyzer Experimental Results

The experimental system for the PEM electrolyzer system built at UND is designed to allow control of various system parameters and enables detailed studies of PEM stack performance and stack characterization, model verification and improved interfacing to renewable energy sources. This system is capable of controlling parameters such as water resistivity, DI water flow rate, DI water temperature to stack, hydrogen system pressure, stack current, and desiccant tube drying cycle.

The off–the–shelf HOGEN40® stack is rated to produce 1.05 Nm^3 of dry hydrogen gas at 200 psig (13.8 atm) per hour. The PEM stack consists of 20 cells connected in series having an active area of 0.093 ft^2 (86.4 cm^2). This results in maximum current density of 1.6 A cm^{-2} at 140 A.

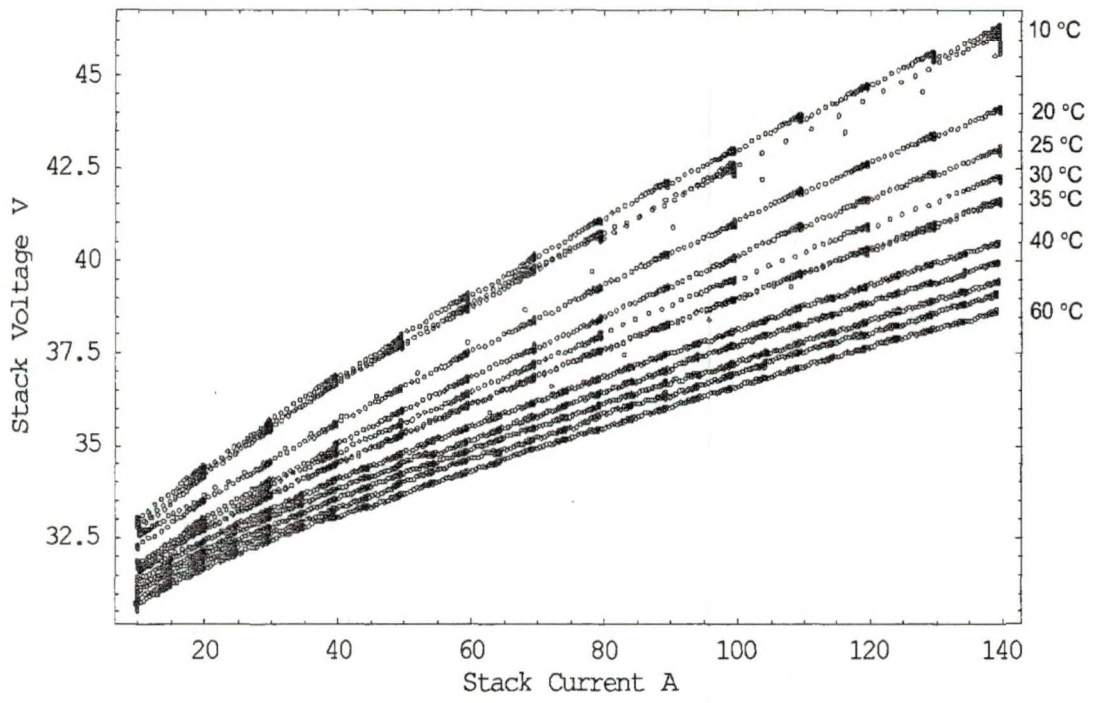

Figure 38: IV characteristic curves at constant cathode pressure (145 psi) at temperature from 10 °C to 60 °C.*

Figure 38 is I-V characteristics of the PEM electrolyzer stack at different temperatures. As shown, for a given current the voltage drops as temperature increases. This increases stack efficiency as activation and ohmic losses are reduced at increased temperature. These losses are known as irreversible potentials. At higher temperature the stack performs better and produces more hydrogen at a given current. These I-V characteristics are used to extract coefficients which represent stack parameters as a function of temperature for PEM stack modeling. Stack parameters such as charge transfer coefficient, exchange current density at anode and cathode and cell conductivity are extracted at various temperatures. This information helps to understand the stack operation better at various temperatures [65].

* All temperatures mentioned in the figure have +/- 0.2 °C error margins. For simplicity they are rounded to whole number.

The beneficial effect of temperature can also be verified by monitoring the increase in pressure in first few minutes of operation at various temperatures by setting the cathode side back pressure regulator at varying pressures. As shown in Figure 39, pressure increases more rapidly at higher temperature indicating more hydrogen production.

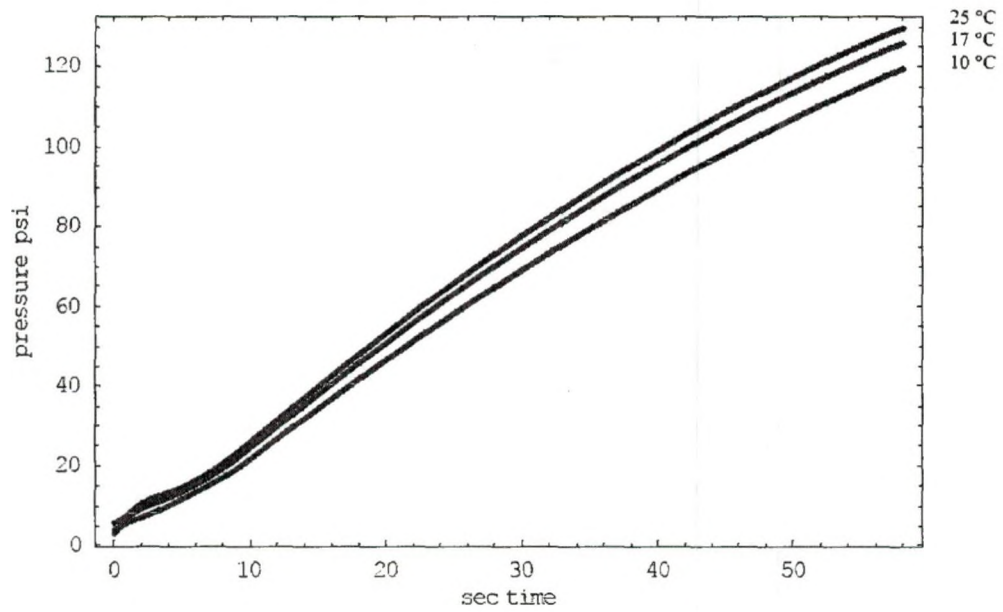

Figure 39: Pressure rise characteristic for first minute when cathode pressure set at 165 psi using back pressure regulator

The expected pressure rise is logarithmic with time, but the beginning pressure rise exhibited an 'S' shaped nature as shown in Figure 40 and Figure 41.

This rise is observed at all temperatures of operation. This rise is observed only upto 12 psi above atmosphere at the beginning of operation. After a few seconds the pressure rises almost linearly.

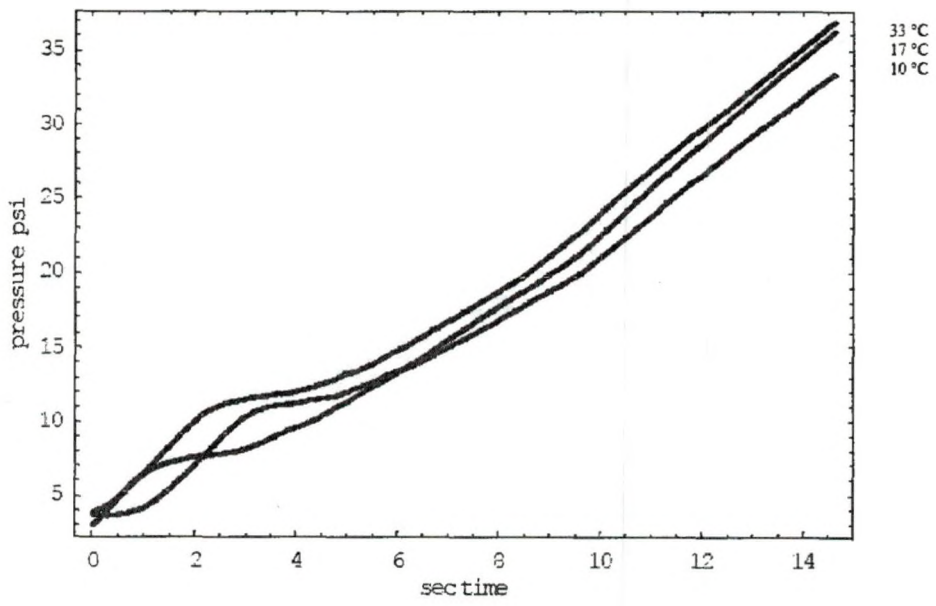

Figure 40: Pressure rise behavior for first few seconds when cathode pressure set at 165 psi using back pressure regulator.

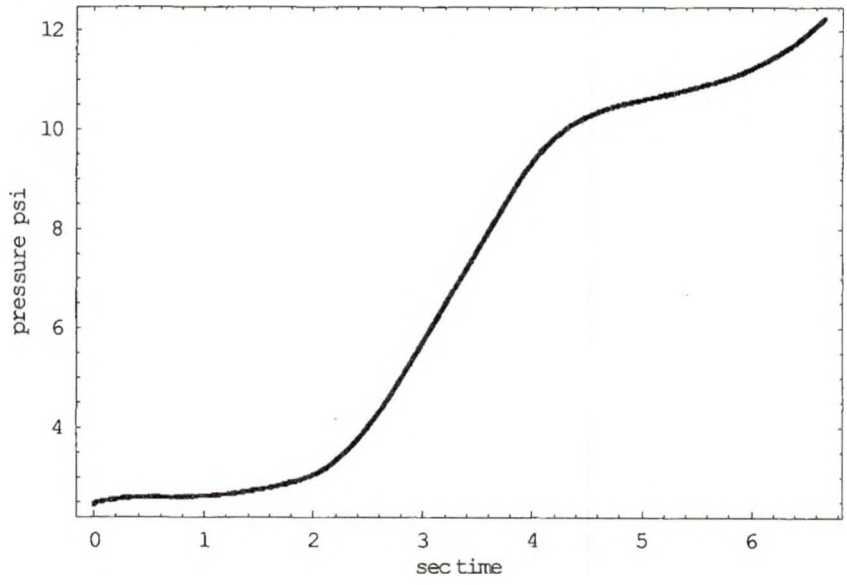

Figure 41: Pressure rise behavior for first 7 seconds at 30°C, cathode pressure set at 165 psi.

The suspects for this behavior are

1. Physical phenomena in stack, such as expansion/contraction of membrane electrode assembly(MEA) or stack structure
2. Catalyst's role in activation energy of the reaction
3. Back pressure regulator behavior
4. Other components between stack and back pressure regulators like high pressure hydrogen-water separator, coalescing filter and two tube desiccant drying system.
5. DC power supplies

The main suspect was DC power supplies, though the response of power supplies is about 2 milliseconds. Tests were performed at 30°C by interrupting the power to the stack supplied by DC power supplies after every 7 seconds. The delay between each step (7 second) was 3-4 seconds. The results for these tests also showed the 'S' shape pressure rise for first step only. The consecutive steps showed the almost linear pressure rise with time.

After detailed study of back pressure regulator (BPR) behavior by repeating the tests at different pressures, it was concluded that BPR is not the cause behind this pressure behavior. Tests results at different pressures showed no change in this behavior with pressure. Possibilities that other equipment mentioned causing this also neglected after doing some more tests.

The remaining suspects are physical phenomena such as contraction or expansion of the cell assembly under the influence of sudden pressure increase and catalyst response time to overcome the activation energy of the reaction. EIS tests of an electrolyzer for a

whole frequency range of 20 kHz to 0.01 Hz can shed some light on this behavior if it is related to the catalyst activity.

4.4 PEM Electrolyzer EIS Results and Discussion

In the absence of an off–the–shelf DC power supply capable of fulfilling the requirements for EIS tests of a 6 kW PEM electrolyzer, EIS tests were performed only for the high frequency (20 kHz to 1 kHz) and low frequency (20 Hz to 0.5 Hz) range using the custom transformer core and modified existing switching DC power supply respectively. The EIS tests were conducted using the experimental setup explained earlier in Chapter 3. The EIS data were plotted as a Nyquist impedance plot for analysis. During all these tests, the stack voltage is measured directly across the stack and current is measured across the 0.5 mΩ shunt resistor. The voltage signal to the corresponding current across the shunt is sent to channel 1 of the FRA and measured stack voltage to the channel 2.

4.4.1 Amplitude Selection for Electrolyzer EIS Tests

For electrolyzer EIS tests, the amplitude of an AC signal should be large enough to cause a voltage perturbation that can be measured by FRA to distinguish it from the noise. As the current is measured across the 0.5 mΩ shunt resistor, the small AC signal results in a very small voltage signal which can not be distinguished from noise. To find the optimal ac signal amplitudes for the EIS tests of the electrolyzer, impedance data at low frequency were collected at various ac signal amplitude of the applied DC current.

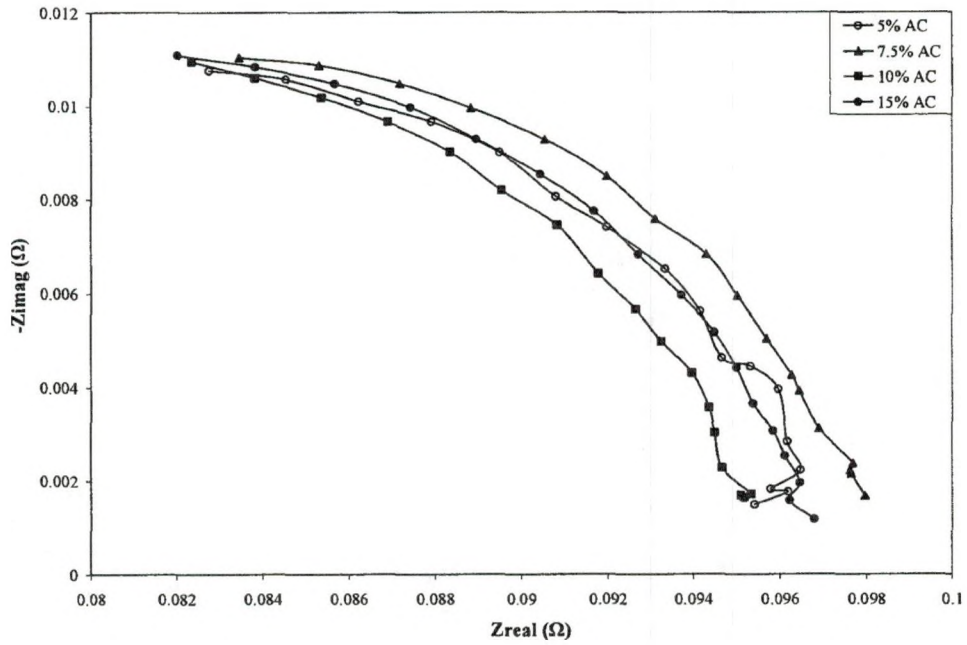

Figure 42: AC signal amplitude selection test for EIS analysis of a 6 kW PEM electrolyzer at 20 Adc

Low frequency impedance data was collected at 20 Adc with 5%, 7.5%, 10% and 15 % ac signal amplitude of the DC as shown in Figure 42. The low frequency impedance data obtained at AC signal amplitude of 5% of the DC was found scattered. However, at 7.5 % and above the impedance data was less scattered. The AC signal amplitude of 7.5 % was not large enough at lower current levels than 20 Adc. At low current levels (< 20 Adc), the perturbation caused by 7.5% AC amplitude signal was very small for a FRA to distinguish between noise and the response signal and the impedance plot observed was very scattered. Also, AC signal amplitude of 15% of the DC limits the EIS test current range at the higher end (70 Adc and beyond). For example, at lower frequencies, 15 % AC signal amplitude would put 12 A peak to peak AC signal on top of 80 Adc. This can cause current to oscillate between 92 A and 68 A. However, at very low frequencies (<1 Hz), the current can oscillate beyond 15% range of that particular

DC current. Thus, the oscillating current may reach the maximum rated output current (100 A) of the DC power supply jeopardizing its safe operation or may cause permanent damage. After repeated tests at various current levels, AC signal amplitude of 10 % of the DC was found optimal the whole current range. All the low and high frequency electrolyzer EIS tests were conducted at the AC signal amplitude of 10% of the DC.

4.4.2 Low Frequency EIS Tests For The Electrolyzer

The low frequency EIS tests were conducted at various current levels with an AC signal amplitude of 10% of the DC. Figure 43 shows the Nyquist impedance plot for the current range from 1 Adc to 3 Adc. As the electrolyzer stack is rated at 140 Adc, not much electrolytic activity can be expected at current levels such as 1 Adc. The low frequency impedance at these current levels is found to increase as current increased.

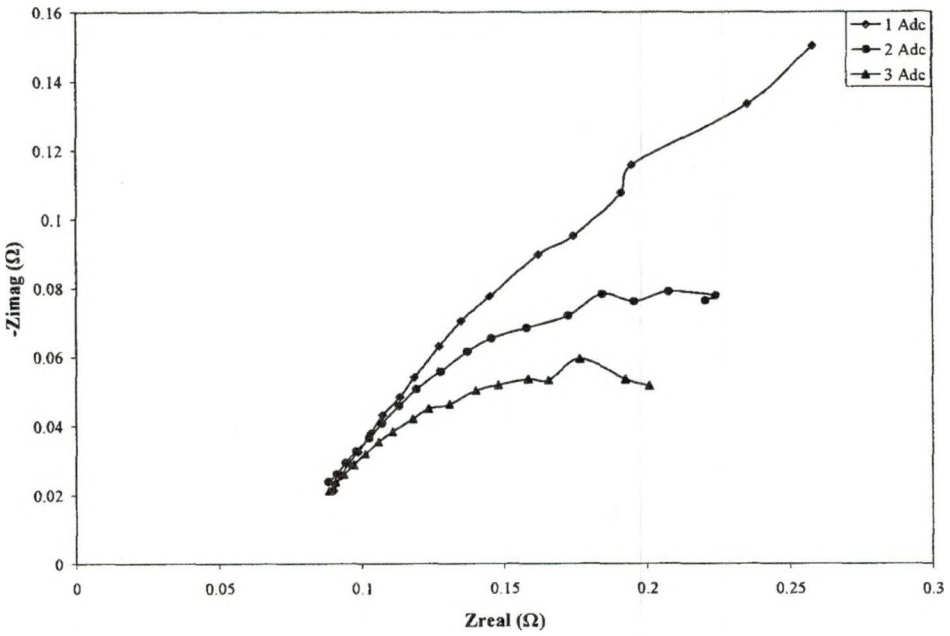

Figure 43: Low frequency electrolyzer EIS tests for the current range 1 Adc to 3 Adc with AC signal amplitude of 10 % of DC

The low frequency impedance data from 5 Adc to 30 Adc is shown in Figure 44. As current increased from 5 Adc, both the real and imaginary part of the impedance decreased. The decrease in impedance with increasing current indicates the lower polarization resistance at higher currents. The shape of the impedance plot for the current range from 5 Adc to 15 Adc is different than from 20 Adc and beyond.

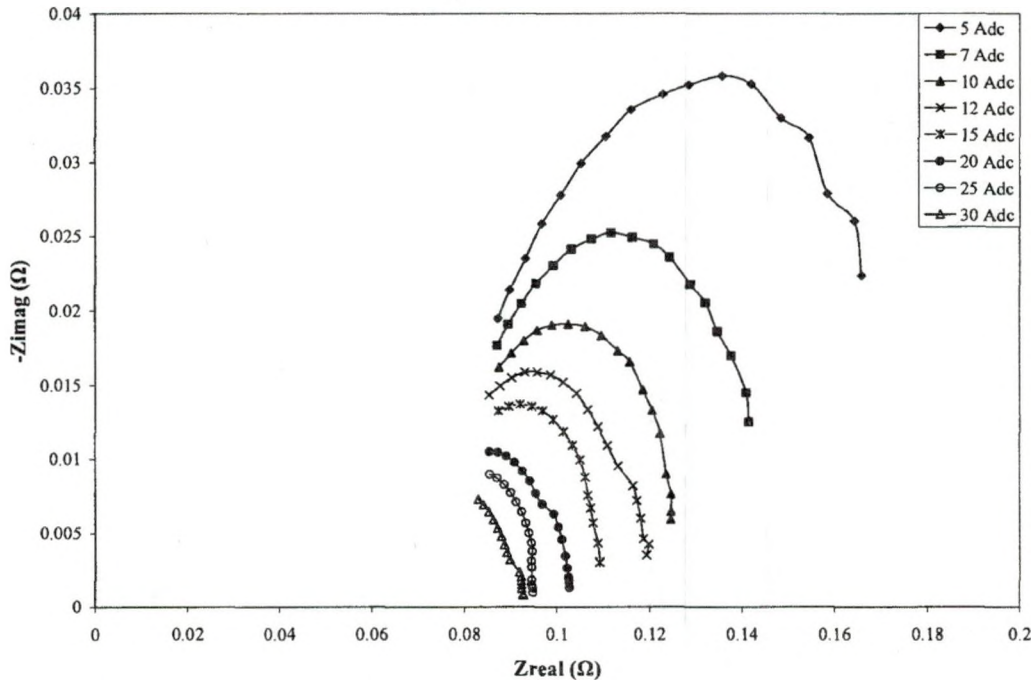

Figure 44: Low frequency electrolyzer EIS tests for the current range 5 Adc to 30 Adc with AC signal amplitude of 10 % of DC

Figure 45 shows the low frequency impedance plot for the current range from 35 Adc to 80 Adc. As explained earlier, only one switching power supply has been modified for the low frequency electrolyzer EIS tests and it is capable of supplying 100 Adc. EIS tests were conducted with 10 % ac signal modulation therefore the current range is limited to 80 Adc for safety reasons. The general trend of impedance data from Figure 44 and Figure 45 show that polarization resistance decreases with increasing current. The

polarization resistance has decreased approximately from 0.104 Ω at 20 Adc to 0.079 Ω at 80 Adc. The low frequency impedance data is found to be little scattered. The possible reason may be the response of the modified power supply at lower frequencies (< 2 Hz) is not very good for higher current ranges.

The tests were repeated to ensure the consistency of the data. Low frequency inductive behavior was observed beyond 70 Adc. It can be concluded from this data that inductive effects would be present at higher currents (beyond 70 Adc) and data from frequency ranges lower than 0.5 Hz (upto 0.01 Hz) can help study these inductive effects. A decrease in polarization resistance with increasing current also indicates the lower activation losses at higher currents. However, at higher current levels close to the rated current (140 Adc), mass transport losses can be decisive for the electrolyzer efficiency.

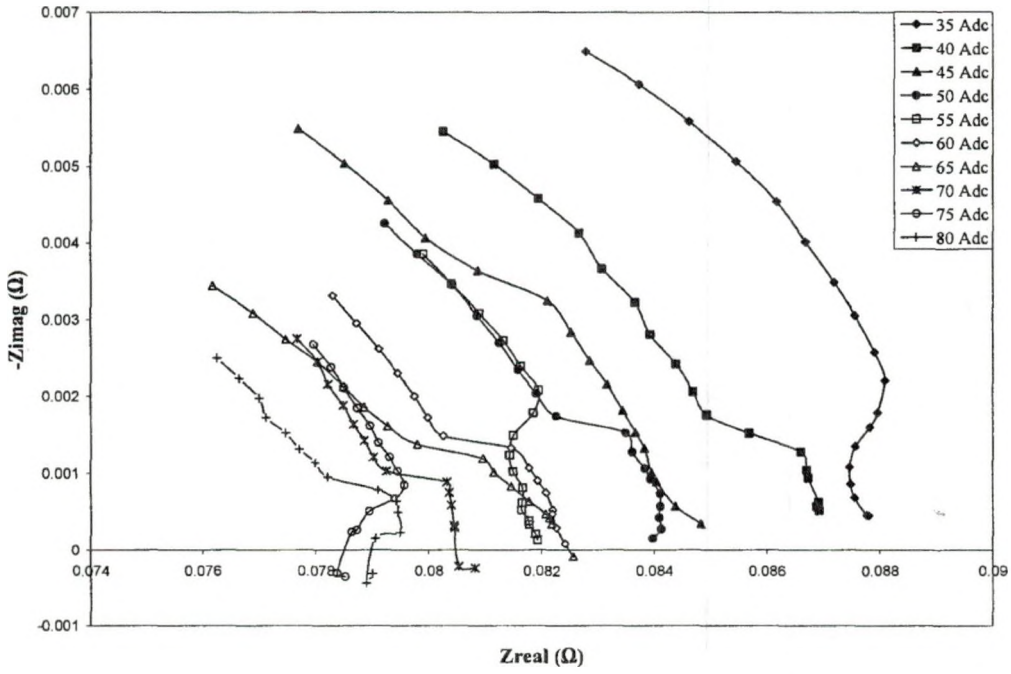

Figure 45: Low frequency electrolyzer EIS tests for the current range 35 Adc to 80 Adc with AC signal amplitude of 10 % of DC

4.4.3 Effect of Pressure on Low Frequency Impedance Data

As discussed earlier in the electrolyzer experimental results section, the operating parameters such as temperature and pressure affect the electrolyzer stack performance. Low frequency EIS tests were conducted to study the effect of stack output pressure on the impedance data. The effect of stack output pressure on electrolyzer impedance can be seen in Figure 46. The low frequency impedance data at 30 Adc and 40 Adc were obtained at cathode open to atmosphere and at 50 psi. The electrolyzer stack output pressure can be controlled using the back pressure regulator as explained earlier in the experimental setup for 6 kW PEM electrolyzer (section 2.2.2). As shown in Figure 46, the electrolyzer stack impedance increases with increasing pressure. This increase in impedance with pressure can decrease the electrolyzer efficiency. This effect of pressure should be considered while building the high pressure electrolyzers. At high output pressures (>1000 psi) the electrolyzer efficiency can reduce significantly. Therefore, there would be a trade–off between the output pressure and efficiency.

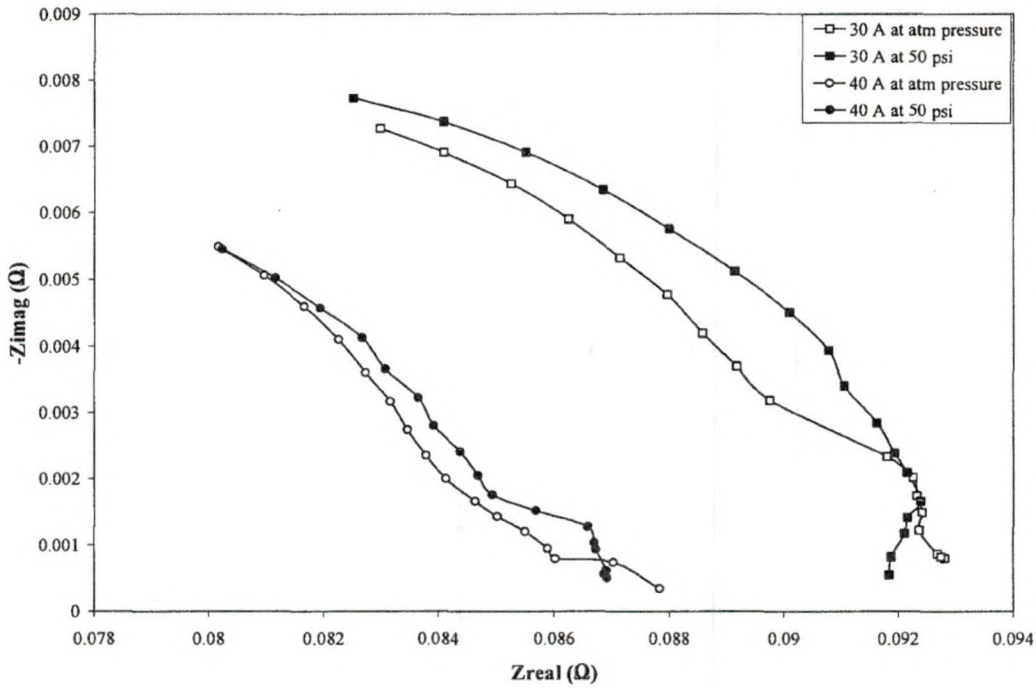

Figure 46: Effect of electrolyzer stack output pressure on the low frequency impedance data at various current

4.4.4 Effect of Temperature on Low Frequency Impedance Data

The electrolyzer performance is dependent on the thermodynamics of the electrolytic reaction. Therefore, temperature is a key operating parameter to influence its performance. As discussed earlier in the I-V characteristics of the electrolyzer (Figure 38), at a particular stack current, the stack voltage decreases with increasing operating stack temperature. This effect of stack temperature on low frequency EIS data is studied at 30 Adc with AC signal amplitude of 10% of the DC. Figure 47 clearly shows a decrease in the polarization resistance with increasing stack temperature. The polarization resistance has decreased approximately from 0.118 Ω at 10 °C to 0.079 Ω at 45 °C. The rate of decrease in the polarization resistance is more at the lower temperatures than at higher temperatures.

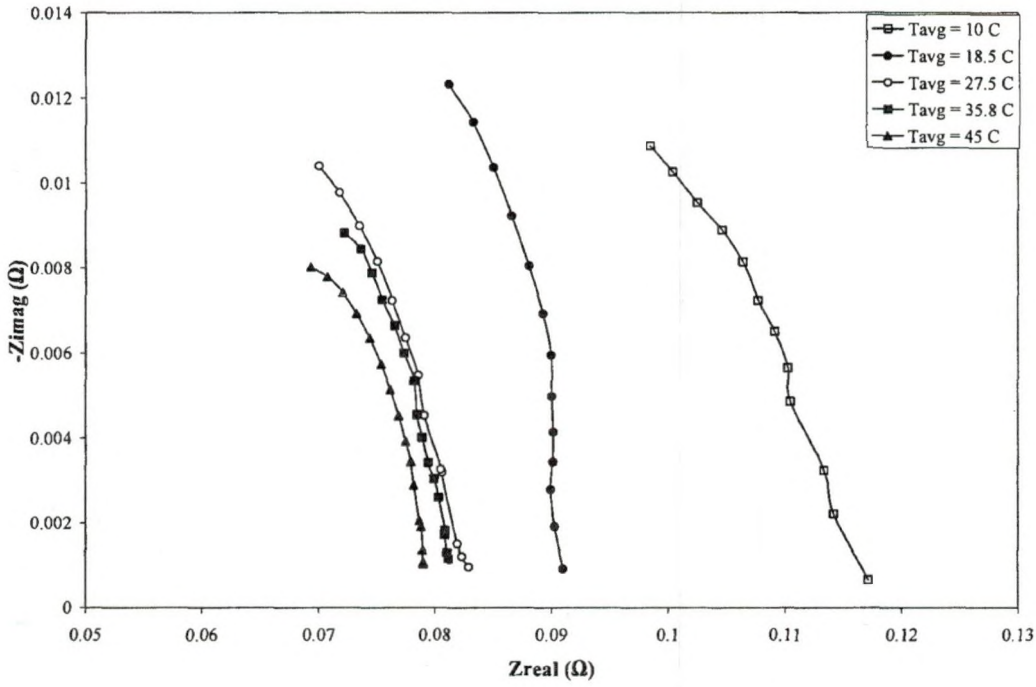

Figure 47: Effect of electrolyzer stack temperature on the low frequency impedance data at 30 Adc with AC signal amplitude of 10% of the DC.

At temperatures higher than 45 °C, the polarization resistance is expected to decrease more. However, the electrolyzer stack operating temperature is limited to 75 °C to 80 °C due to membrane properties constrain. The decrease in the polarization resistance with increasing temperature is an indication of minimal activation losses at high temperatures which can result in high electrolyzer efficiency. The electrolyzer stack temperature is controlled through the DI water temperature; hence any kind of waste heat can be used to increase the DI water temperature to achieve the high electrolyzer efficiency. Increasing the inlet DI water temperature to the electrolyzer with a special heating system will increase the electrolyzer efficiency but may result in low overall system efficiency. Therefore, in case of distributed hydrogen generation, the waste heat from other processes can be used to increase the DI water temperature. Care should be

taken while increasing the DI water temperature, not to pass the hot water through the DI system as some resin beds breaks down at high temperatures (> 60 °C).

4.4.5 High Frequency Tests For Electrolyzer

The high frequency impedance data of a 6 kW PEM electrolyzer was obtained using the EIS experimental setup explained earlier. The impedance data for the frequency range from 20 kHz to approximately 1 kHz was obtained. The high frequency impedance data at various currents is plotted as a Nyquist plot as shown in Figure 48. No significant change in the impedance was observed at high frequencies at various currents. High frequency inductive effects were absent at current levels upto 60 Adc. The electrolyzer EIS test were conducted only upto 60 Adc due to the power supply and amplifier limitations. At higher current levels the amplifier draws lot of current from the switching DC power supply and goes into fault condition when the frequency reaches around 1 kHz. Due to this limitation, the EIS experiments at current level beyond 35 Adc were limited to 1.3 kHz. During the EIS tests beyond 60 Adc, the amplifier drew the current from the DC power supply beyond its specifications which blew out one of the amplifier's capacitors. The impedance plots at various currents starts deviating approximately at 2 kHz and more deviation can be expected as frequency decreases upto 0.1 Hz.

The whole impedance spectrum for the electrolyzer from 20 kHz to 0.5 Hz can be obtained with the three power supply setups as explained in the electrolyzer EIS experimental setup section. The operating procedure to obtain the low and high frequency impedance data at various currents is summarized in Appendix B. It is recommended that

funding be sought to allow the purchase of these power supplies to allow the full EIS spectrum to be obtained.

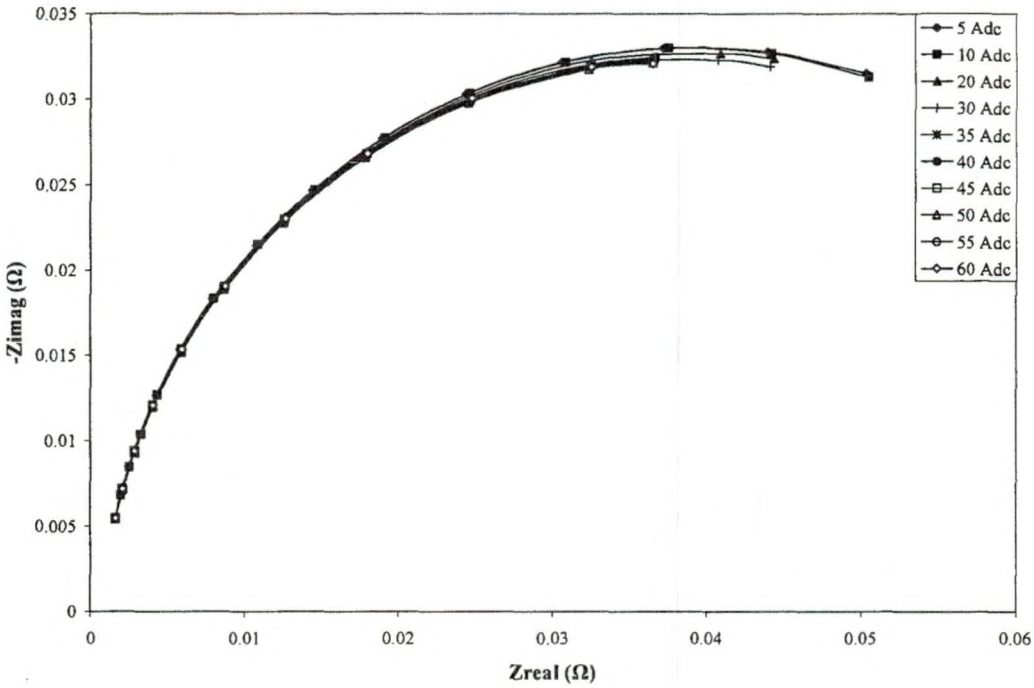

Figure 48: High frequency electrolyzer EIS data for the current range 5 Adc to 60 Adc with AC signal amplitude of 10 % of DC

CHAPTER 5

SEMIEMPIRICAL MODELING OF PEM ELECTROLYZER STACK

The performance of a 6 kW proton exchange membrane (PEM) electrolyzer was modeled using a semiempirical equation. Total cell voltage was represented as a sum of the Nernst voltage, activation overpotential and ohmic overpotential. A temperature and pressure dependent Nernst potential, derived from thermodynamic principles, was used to model the 20 cell PEM electrolyzer stack. An experimental system designed around a 6 kW PEM electrolyzer was used to obtain the current-voltage characteristics at different stack temperatures. A nonlinear curve fitting method was employed to determine the equation coefficients from the experimental current-voltage characteristics. The modeling results showed an increase in the anode and cathode exchange current densities with increasing electrolyzer stack temperature. The membrane conductivity was also increased with increasing temperature and was modeled as a function of temperature. The electrolyzer energy efficiencies at different temperatures were evaluated using temperature dependent higher heating value voltages instead of a fixed value of 1.48 V.

5.1 Thermodynamics of Water Electrolysis

Using electricity, hydrogen generation is achieved by dissociating water molecules into the diatomic molecules of hydrogen and oxygen. The overall water electrolysis reaction can be represented as,

$$H_2O \rightarrow H_2 + \frac{1}{2}O_2 \qquad \Delta H^0_{25} = 285.83 \text{ kJ} \qquad 5\text{-}1$$

where, ΔH_{25}^{0} is the change in enthalpy of the reaction at 25 °C and standard pressure of one atmosphere for liquid water. Electrolysis of one mole of water produces a mole of hydrogen gas and a half mole of oxygen gas. Enthalpy and entropy for the reaction elements are summarized below from thermodynamic property tables [68],

Table 3: Thermodynamic properties for water electrolysis reaction constituents at 25 °C

Property	H_2O	H_2	$0.5\,O_2$	Change in Property
Enthalpy	-285.830 kJ	0	0	$\Delta H = 285.83$ kJ
Entropy	69.61 J/K	130.68 J/K	102.57 J/K	$T\Delta S = 48.7$ kJ

Total energy must be supplied to split the water and to expand the gases, so at 298.15 K and atmospheric pressure this system work is given by

$$W = P\Delta V \qquad 5\text{-}2$$

$$= 101.3\ N/m^2 * 1.5\ moles * 0.0224\ m^3/mol * (298.15/273.15)$$

$$= 3.715\ kJ$$

From thermodynamic principles, the change in internal energy is given by,

$$\Delta U = \Delta H - P\Delta V \qquad 5\text{-}3$$

$$= 285.83 - 3.715$$

$$= 282.1\ kJ$$

But, this change in internal energy must be accompanied by the energy required for expansion of gases, so change in enthalpy (ΔH) is the energy required to accomplish the water electrolysis. Entropy increases in the water dissociation reaction. This amount of energy is represented by $T\Delta S$ and can be provided from the environment. Actual

energy needed to carry out the electrolysis reaction is given by Gibbs' free energy as follows,

$$\Delta G = \Delta H - T\Delta S \qquad 5\text{-}4$$

$$= 285.83 - 48.7 = 237.1 \text{ kJ}$$

This amount of energy must be supplied in a form such as electric energy for the reaction to proceed. The bridge between electrical energy and chemical energy needed to carry out the water electrolysis can be represented by,

$$E = -\frac{\Delta G}{nF} \qquad 5\text{-}5$$

where, E is the electrolysis cell voltage, n is the number of moles of electrons transferred during the reaction (2 for water electrolysis reaction), ΔG is the change in Gibbs' free energy of the reaction and F (the Faraday's constant) is 96,485 Coulomb per mole of electron.

This fundamental equation gives the electromotive force (emf) or voltage required for water electrolysis assuming no losses or irreversibilities.

$$E = -\frac{237100}{2 \times 96485} = -1.23\text{V}$$

The negative sign indicates that energy is required for the reaction. In this way, at standard temperature, one mole of water thermodynamically needs at least 1.23 V to split it into hydrogen and oxygen assuming there are no losses. Adding pressure effects of product gases and water vapor or voltage required for expansion of product gases to this emf results in the reversible voltage (E_{rev}) for electrolysis. Reversible voltage can be represented by Nernst potential [18].

5.2 Modeling

Electrolysis of one mole of water produces one mole of wet hydrogen and half mole of wet oxygen and water vapor. At standard temperature of 298.15 K, water electrolysis needs 1.23 V potential to produce the product gases. The bridge between electrical energy and corresponding chemical energy needed to carry out the water electrolysis can be represented by equation 5-5. Thus, the voltage (E) needed for water electrolysis is directly proportional to the Gibbs' free energy of the reaction. The Gibbs' free energy is in turn dependent on the change in enthalpy (ΔH) of the reaction. Enthalpy is a function of temperature which causes the Gibbs' free energy to vary with temperature, and therefore the potential (E) required to carry out the electrolysis reaction is also temperature dependent. While modeling the electrolyzer, dependence of the reversible potential on the temperature is generally ignored [66]. This can result in inaccurate interpretations of the efficiency and electrolyzer cell parameters such as membrane conductivity, anode and cathode exchange densities, and charge transfer coefficients at the electrodes [66]. Many investigators use a value 1.23 V for the reversible potential while modeling an electrolysis cell or stack, which is true only at standard temperature and pressure.

In this modeling work, efforts were taken to find the dependence of the reversible potential on temperature for low temperature PEM electrolyzers. Experimental I-V characteristics obtained from a 6 kW PEM electrolyzer stack were modeled using Mathematica™ programming software. Nonlinear curve fitting algorithms were utilized to extract the critical parameters such as anode and cathode exchange current densities and membrane conductivity. Temperature dependent equations for the reversible

potential along with equations for activation and ohmic losses from the literature were used to model the experimental I-V data.

LeRoy and Bowen [67] have described the thermodynamics of water electrolysis assuming hydrogen, oxygen, and water vapor behave as ideal gases. The enthalpy of water dissociation reaction is expressed as follows,

$$\Delta H_{t,p} - \Delta H_{25}^0 = [\Delta H_t^0 - \Delta H_{25}^0] + [\Delta H_{t,p} - \Delta H_t^0] \qquad 5\text{-}6$$

where,

$$\Delta H_t^0 - \Delta H_{25}^0 = [\Delta H_t^0 - \Delta H_{25}^0]_{H_2} + 0.5[\Delta H_t^0 - \Delta H_{25}^0]_{O_2} - [\Delta H_t^0 - \Delta H_{25}^0]_{H_2O(liq.)} \qquad 5\text{-}7$$

and

$$\Delta H_{t,p} - \Delta H_t^0 = [\Delta H_{t,p} - \Delta H_t^0]_{H_2} + 0.5[\Delta H_{t,p} - \Delta H_t^0]_{O_2} - [\Delta H_{t,p} - \Delta H_t^0]_{H_2O(liq.)} \qquad 5\text{-}8$$

In these equations, t is temperature in °C, p is the pressure in atmosphere, and ΔH_{25}^0 is the change in enthalpy at standard temperature and is equal to 285.83 kJ

The value for $\Delta H_t^0 - \Delta H_{25}^0$ in equation 5-7 is calculated for different temperatures using following equations [68]

$$\Delta H_t^0 = \langle C_P \rangle_H (T - T_0) \qquad 5\text{-}9$$

where, T is temperature in Kelvin and T_0 = 298.15 K and $\langle C_P \rangle_H$ is defined as the mean heat capacity and is given by

$$\frac{\langle C_P \rangle_H}{R} = A + \frac{B}{2} T_0(\tau + 1) + \frac{C}{3} T_0^2(\tau^2 + \tau + 1) + \frac{D}{\tau T_0^2} \qquad 5\text{-}10$$

where,

$$\tau \equiv \frac{T}{T_0}$$

The coefficients A, B, C and D for hydrogen, oxygen and water obtained from the thermodynamic tables for heat capacities for gases and liquids [68] are as follows

Table 4: Constants for calculating heat capacities of chemical species

Chemical species	A	10^3 B	10^6 C	10^{-5} D
Hydrogen (H_2)	3.249	0.422	-	0.083
Oxygen (O_2)	3.639	0.506	-	-0.227
Water (H_2O) $_{liq.}$	8.712	1.25	-0.18	-

The value for $\Delta H_t^0 - \Delta H_{25}^0$ is calculated using these values at different temperatures. $\Delta H_t^0 - \Delta H_{25}^0$ values plotted as a function of temperature t in °C as shown in Figure 49 and can be represented as:

$$\Delta H_t^0 - \Delta H_{25}^0 = 741 - 51.3\ t - 0.063\ t^2 \qquad 5\text{-}11$$

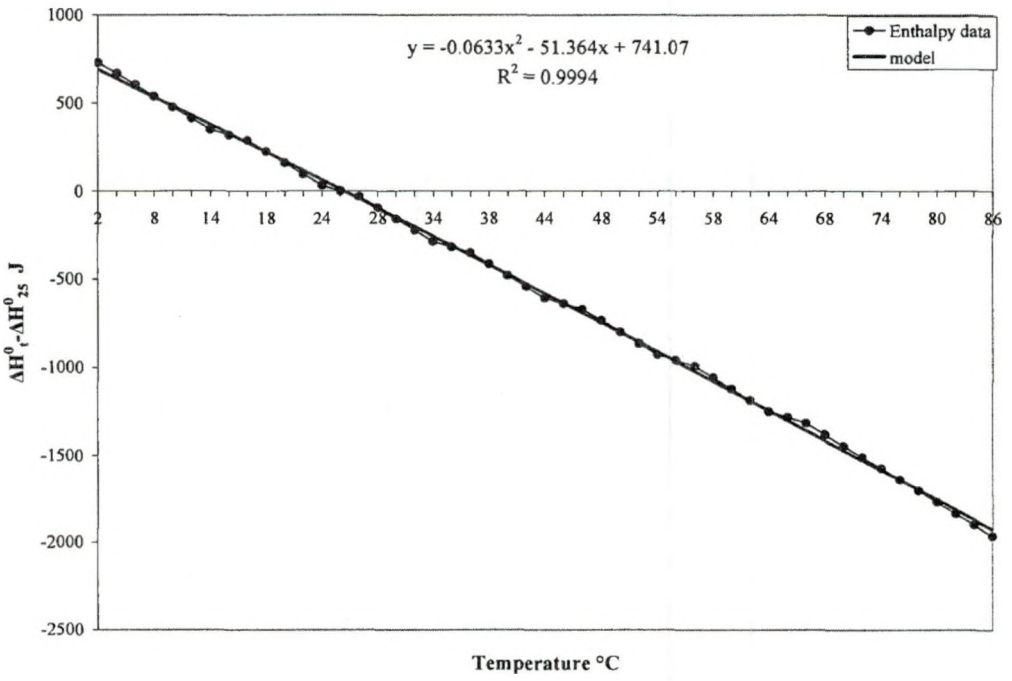

Figure 49: $\Delta H_t^0 - \Delta H_{25}^0$ as function of temperature

The effect of temperature and pressure on the enthalpy of water electrolysis reaction can be seen as an enthalpic voltage and can be expressed as [67]

$$V_t = \frac{\Delta H_t^0}{nF} \qquad 5\text{-}12$$

Substituting for ΔH_t^0 from equation 5-7, V_t can be represented as.

$$V_t = 1.4850 - 2.66\text{x}10^{-4}\, t - 3.28\text{x}10^{-7}\, t^2 \qquad 5\text{-}13$$

The temperature effect of enthalpic voltage can be expressed using above equation 5-13. Also, the higher heating value voltage (V_{HHV}) is defined as [67]

$$V_{HHV,t} = V_t + (\Delta H_t^0 - \Delta H_{25}^0)_{H_2O(liq.)} / nF \qquad 5\text{-}14$$

where, $(\Delta H_t^0 - \Delta H_{25}^0)_{H_2O(liq.)}$ was evaluated using equation 5-9 and 5-10. Values for $(\Delta H_t^0 - \Delta H_{25}^0)_{H_2O(liq.)}$ were calculated using coefficients mentioned in Table 4. $(\Delta H_t^0 - \Delta H_{25}^0)_{H_2O(liq.)}$ is plotted as a function of temperature t in °C as shown in Figure 50.

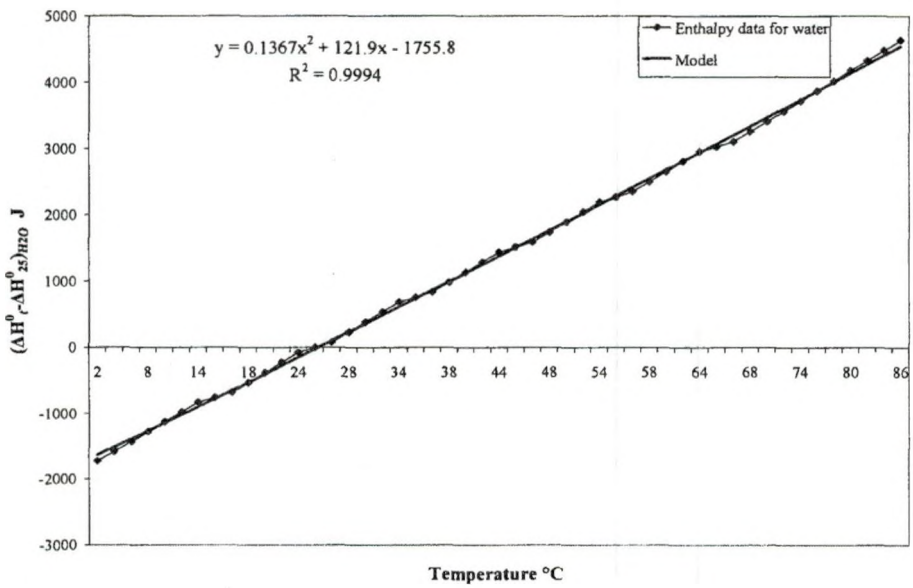

Figure 50: $(\Delta H_t^0 - \Delta H_{25}^0)_{H_2O(liq.)}$ as a function of temperature

$(\Delta H_t^0 - \Delta H_{25}^0)_{H_2O(liq.)}$ can be represented as a function of temperature as follows;

$$(\Delta H_t^0 - \Delta H_{25}^0)_{H_2O(liq.)} = -1755 + 121\,t + 0.136\,t^2 \qquad 5\text{-}15$$

Then, $V_{HHV,t}$ can also be represented as a temperature function by substituting equation 5-15 in equation 5-14 as follows;

$$V_{HHV,t} = 1.47 + 3.65 \times 10^{-4}\,t + 3.80 \times 10^{-7}\,t^2 \qquad 5\text{-}16$$

Equation 5-16 can predict the values of V_{HHV} at respective temperatures to evaluate the V_{HHV} based energy efficiency of electrolyzers.

Thermoneutral voltage (V_{tn}) is a voltage of a perfectly insulated electrolyzer with no net heat input or output. This voltage is equal to the sum of higher heating value voltage (V_{HHV}) and voltage corresponding to the energy required for saturation of hydrogen and oxygen gas with water vapor [69].

In practical situations, if an electrolyzer is operating at cell voltage Vc, then the amount of energy input into the electrolyzer will be nFVc which can be represented as follows [67];

$$nFV_c = nFV_{tn} + Q_{waste} \qquad 5\text{-}17$$

where, Q_{waste} is the waste energy in the form of radiation, conduction and convection which comes out with wet hydrogen and wet oxygen as product of electrolysis.

The thermoneutral voltage (V_{tn}) can be given as

$$nF\,V_{tn} = nF\,V_{HHV} + \phi\,[H_{H_2O(g),t,p^*} - H^0_{H_2O(liq.),25}] \qquad 5\text{-}18$$

where, ϕ is given by

$$\phi = 1.5 \times P^*/(P-P^*) \qquad 5\text{-}19$$

where, P is total pressure and P^* is the vapor pressure of water in atmosphere.

The vapor pressure of water (P^*) at different temperatures were obtained using the steam table [68] to calculate ϕ.

For simplicity, $[H_{H_2O(g),t,p^*} - H^0_{H_2O(liq.),25}]$ is approximated to Y as follows [67]

$$Y = 42960 + 40.7\,t - 0.0668\,t^2 \qquad 5\text{-}20$$

Thermoneutral voltage (V_{tn}) can be expressed in simplified form by substituting equations 5-20 and 5-19 in equation 5-18 as follows,

$$nF\,V_{tn} = nF\,V_{HHV} + \phi\,Y \qquad 5\text{-}21$$

In addition to temperature, the emf (E) of an electrolyzer cell producing wet hydrogen and wet oxygen is also affected by the concentrations of products and reactants. Considering the pressure effects of these gases, the emf of the cell, or the Nernst potential, is given by,

$$E_{Nernst} = E^0_{rev} + \frac{RT}{nF}\ln\left(\frac{P_{H_2}P^{0.5}_{O_2}}{P_{H_2O}}\right) \qquad 5\text{-}22$$

where, E^0_{rev} is the reversible potential without the effect of pressures. In terms of electrical energy supplied to the electrolyzer, equation 5-22 can be written as,

$$nFE_{Nernst} = nFE^0_{rev} + RT\ln\left(\frac{P_{H_2}P^{0.5}_{O_2}}{P_{H_2O}}\right) \qquad 5\text{-}23$$

where, for a given temperature,

$$nFE^0_{rev} = [G^0_{f,H_2} + 0.5G^0_{f,O_2} - G^0_{f,H_2O(Liq.)}] = -\Delta G^0_{f\,H_2O(Liq.)} \qquad 5\text{-}24$$

where, G^0_f is the standard Gibbs free energy of formation. The change in standard Gibbs' free energy of formation of liquid water ($\Delta G^0_{f\,H_2O(Liq.)}$) at 25 °C (298.15 K) is -237.129 kJ and so the value of E^0_{rev} at 25 °C results in 1.2291 V.

From thermodynamic principles [67],

$$\frac{\partial(G/T)}{\partial T} = -\left(\frac{H}{T^2}\right) \qquad 5\text{-}25$$

$$\frac{\partial(E^0_{rev}/T)}{\partial T} = -\left(\frac{V_t}{T^2}\right) \qquad 5\text{-}26$$

The temperature dependent equation for E^0_{rev} was calculated by substituting the value of V_t from equation 5-13 into equation 5-26 and replacing temperature in °C with (T-273.15) to make it in Kelvin. Integrating equation 5-26 results in

$$E^0_{rev} = 1.52 - 1.22 \times 10^{-3}\, T + 1.18 \times 10^{-5}\, T \ln(T) + 5.66 \times 10^{-7}\, T^2 \qquad 5\text{-}27$$

For this work, the partial pressure of hydrogen was calculated based on the total pressure at the cathode ($1x10^6$ Nm^{-2}) and the assumption that the partial pressure of liquid water is equal to its saturated vapor pressure at the given temperature. An assumption is also made that only water vapor and hydrogen exist in the gaseous phase at the cathode and only oxygen and water vapor are present in the gaseous phase at the anode. The total pressure at the anode was assumed to be constant at $1x10^5$ Nm^{-2}. Also, the solubility of hydrogen and oxygen in water are assumed negligible. Ideal behavior of these gases is assumed because of low pressure, hence applying the Dalton's law of partial pressures;

$$P_{O_2} = P_{Anode} - P_{H_2O} \qquad 5\text{-}28$$

$$P_{H_2} = P_{Cathode} - P_{H_2O} \qquad 5\text{-}29$$

The total electrolyzer cell voltage can be represented as,

$$E_{Total} = E_{Nernst} + E_{Activation} + E_{Ohmic} \qquad 5\text{-}30$$

where, E_{Nernst} is given by equation 5-22 and $E_{Activation}$ is an activation overpotential that electrochemical reaction has to overcome for the conversion of reactants to products.

This $E_{Activation}$ is modeled by the Butler-Volmer equation [18]. However, the equation for activation overpotential for this work is not used in its traditional form. The hyperbolic sine approximation to the Butler-Volmer equation used in this work because the hyperbolic form is relatively easy to model using non linear curve fitting algorithms [66, 70]. If one of the exchange current densities (i.e., anode or cathode) is sufficiently larger than the other, then the corresponding activation loss can be neglected [71]. However, for the purpose of extracting the exchange current densities at the anode and cathode from the experimental data obtained for a 6 kW PEM electrolyzer, activation losses at both the electrodes are considered.

$$E_{Activation} = \frac{RT}{2\alpha_A F} Sinh^{-1}\left(\frac{j}{2j_{A,o}}\right) + \frac{RT}{2\alpha_C F} Sinh^{-1}\left(\frac{j}{2j_{C,o}}\right) \qquad 5\text{-}31$$

where, j is the current density, $j_{A,o}$ and $j_{C,o}$ are the exchange current density at the anode and cathode, respectively. α_A and α_C are the charge transfer coefficients (CTC) at the anode and cathode, respectively. The CTC at the cathode is set at 0.5, but the CTC values at the anode have been observed to be a function of temperature and its mean value was used at respective temperatures [65].

The ohmic overpotential, E_{Ohmic}, due to the membrane resistance, is given by

$$E_{Ohmic} = \frac{\varphi}{\sigma} j \qquad 5\text{-}32$$

where, φ is the dry thickness of the electrolyte-membrane (178 μm for Nafion™117) and σ is the conductivity of the membrane (S cm^{-1}).

Substituting for E_{Nernst}, $E_{Activation}$, and E_{Ohmic} in equation 5-30 resulted in following equation which was used to model the experimental I-V data at different temperatures.

$$E_{Total} = E^0_{rev} + \frac{RT}{2F}\ln\left(\frac{P_{H_2}P^{0.5}_{O_2}}{P_{H_2O}}\right) + \frac{RT}{2\alpha_A F}Sinh^{-1}\left(\frac{j}{2j_{A,o}}\right) + \frac{RT}{2\alpha_C F}Sinh^{-1}\left(\frac{j}{2j_{C,o}}\right) + \frac{\varphi}{\sigma}j \quad 5\text{-}33$$

where, E^0_{rev} is given by equation 5-27 as a function of temperature.

Generally, the electrolyzer electrical efficiency (η) is calculated based on the higher heating value voltage using the following equation,

$$\eta = \frac{V_{HHV,t}}{V_C} \quad 5\text{-}34$$

Electrical efficiency is more important than the heat-energy efficiency in terms of the cost of hydrogen production, so research should be focused on reducing the electrolysis cell voltage to bring it closer to the thermoneutral voltage (V_{tn}), enthalpic voltage (V_t), or higher heating value voltage ($V_{HHV,t}$)[72]. This can be achieved by reducing the activation losses and ohmic losses.

5.3 Modeling Results and Discussion

The thermoneutral voltage (V_{tn}) represented by equation 5-21 is a function of $V_{HHV,t}$ (equation 5-16), ϕ (equation 5-19) and Y (equation 5-20). The temperature and pressure dependence of V_{tn} is shown in Figure 51. Thermoneutral voltage decreases with increasing pressure. At higher pressures, thermoneutral voltage increases weakly with temperature, but at low pressures it increases rapidly with temperature. Also, Y does not increase rapidly with temperature, but ϕ does. ϕ decreases with increasing total pressure P and this causes V_{tn} to decrease with increasing pressure.

Enthalpic voltage (equation 5-13), higher heating value voltage (equation 5-16) and thermoneutral voltage (equation 5-21) at 25 atm (367.39 psi) as a function of temperature are plotted in Figure 52. Enthalpic voltage decreases with temperature.

However, $V_{HHV,t}$ and V_{tn} increases with increasing temperature and almost equal till 50 °C. V_{tn} increases rapidly than $V_{HHV,t}$ beyond 50 °C.

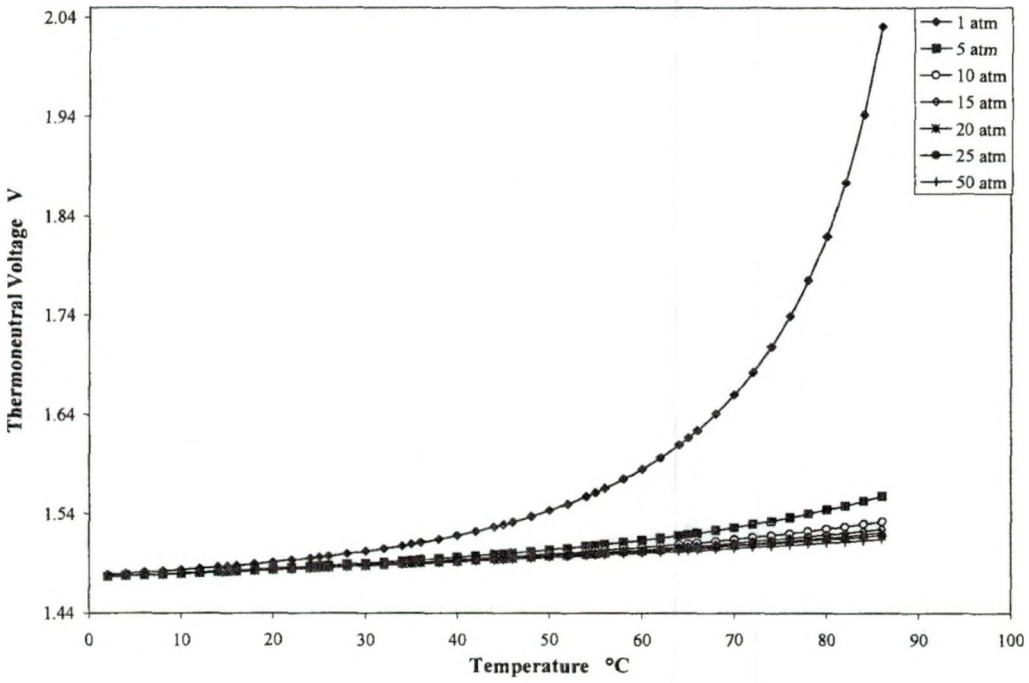

Figure 51: Dependence of thermoneutral voltage on temperature and pressure

Reversible potential without the effect of pressure (E^0_{rev}) from equation 5-27 and the Nernst potential (E_{Nernst}) from equation 5-22 are plotted as a function of temperature in Figure 53. The reversible potential decreases with temperature. The difference between the reversible voltage based on Gibbs' free energy and Nernst potential represents the concentration effects of products and reactants. The difference between these two potentials represents the irreversibilities of the system. Higher temperatures favor the electrolysis reaction, as shown in Figure 53, by decreasing the Nernst potential with increasing temperature.

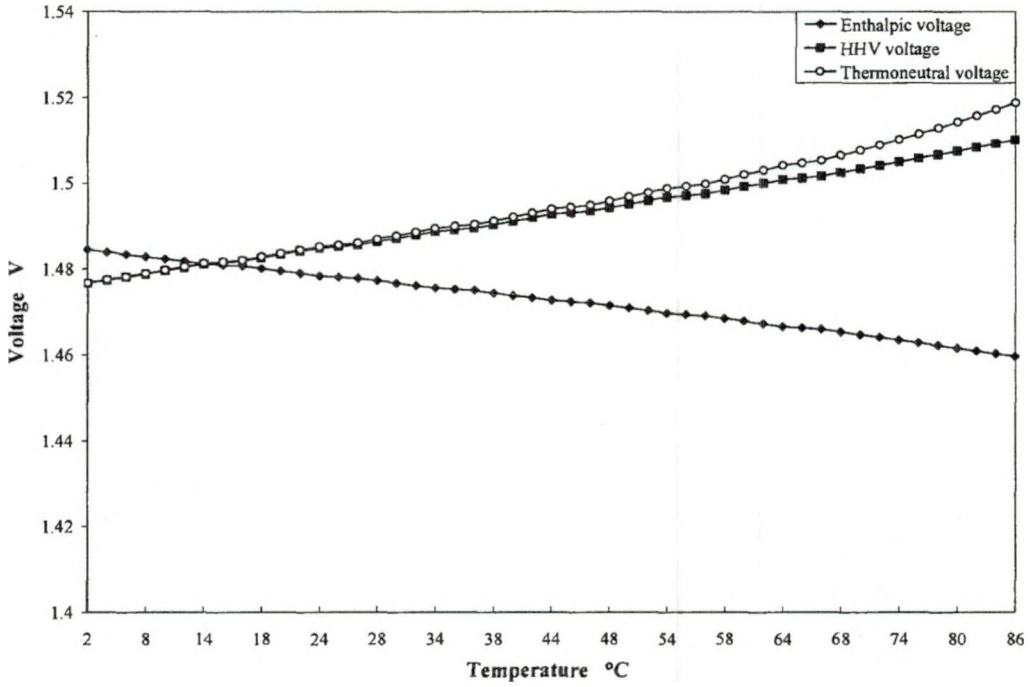

Figure 52: Variation of characteristic voltages of electrolyzer with temperature

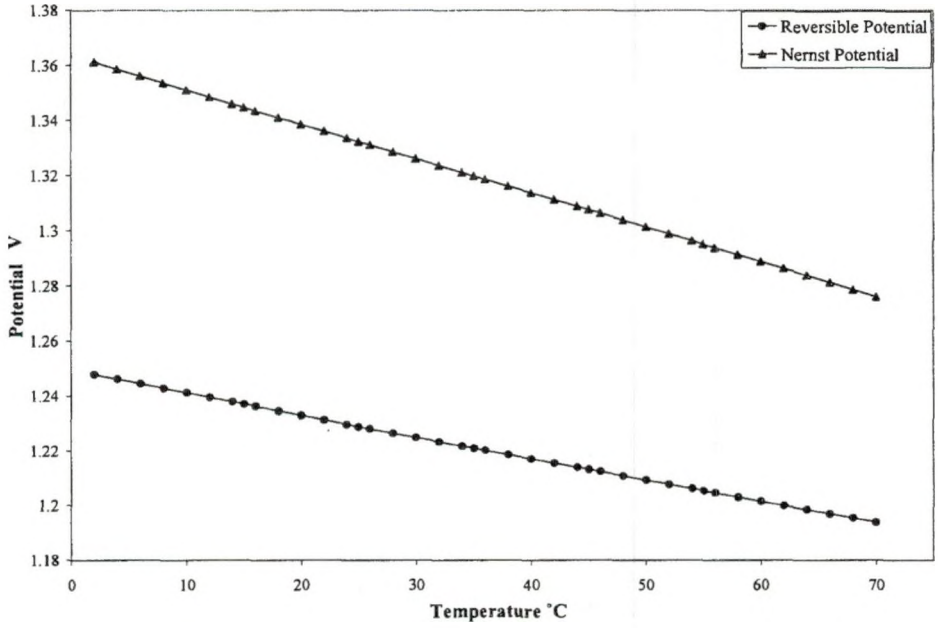

Figure 53: Dependence of reversible potential on temperature

The Nernst potential value has decreased from 1.35 V at 5 °C to 1.27 V at 70 °C. Higher temperatures favor the electrolysis reaction as Nernst potential decreases with temperature.

NREL's milestone report suggests that 80% of the total selling price of hydrogen from large scale electrolyzers is comprised of electricity cost [73].Therefore, improvement in the electrical energy efficiency of the electrolyzers is of prime importance.

The average cell voltage was calculated from the measured stack voltage using the I-V characteristics obtained for various temperatures at 100 A. Single cell voltage was calculated from stack voltage for 20 cells. Equation 5-34 was used to estimate the electrical efficiency of electrolyzer. Higher heating value voltage (V_{HHV}) for various temperatures was calculated using equation 5-16. Many investigators use V_{HHV} value as 1.48 V while calculating electrical efficiency, but V_{HHV} being a function of a temperature, increases with temperature. The estimated value for V_{HHV} at different temperatures was used while estimating the electrical energy efficiency for the electrolyzer using equation 5-34 as shown in Figure 54.

As can be seen from Figure 54, the actual (experimental) cell voltage is higher than the theoretical higher heating value voltage. The difference is most pronounced at low temperatures, resulting in lowest electrical energy efficiency. The cell voltage decreases as the temperature increases, which brings cell voltage closer to the higher heating value voltage resulting in higher electrical energy efficiencies at higher temperature. This confirms that electrolyzers perform better at higher temperatures. In the

case of PEM electrolyzers, the operating temperature is one of the big constraints because of membrane properties.

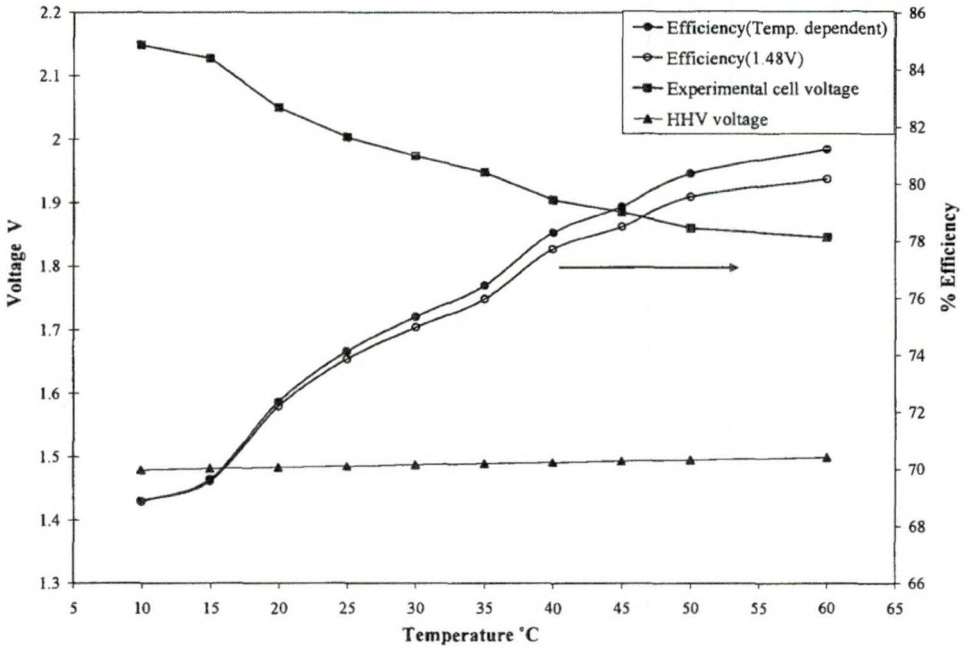

Figure 54: Variation of experimental cell voltage and higher heating value voltage with temperature and electrical energy efficiency at various temperatures at 100 Adc.

To improve the efficiency, the cell voltage should be as close as possible to the higher heating value voltage. This can be achieved by reducing the ohmic resistance using a thinner membrane and by reducing activation losses using better manufacturing processes, material development, and catalyst loading. Reducing heat losses is also required to approach the thermoneutral voltage. The efficiency and performance of PEM water electrolysis can be improved by optimizing the electrocatalysis properties such as active surface area, specific gravity, electronic resistance, and particle/layer structure[74]

The efficiencies shown in Figure 54 were calculated using experimental cell voltages and a constant value of the higher heating value voltage (1.48 V) as well as the V_{HHV} voltage as a function of temperature. A clear difference in efficiencies [Efficiency

(1.48 V) and Efficiency (Temp. dependent)] was observed at higher temperatures using different values for V_{HHV}. This shows that the use of constant V_{HHV}, 1.48 V, may result in a lower efficiency calculation at higher temperatures for PEM electrolyzers.

Nonlinear curve fitting, based on the least square methods, was used to fit the experimental I-V characteristics to determine the exchange current densities at both electrodes and the membrane conductivity as a function of temperature. The NonLinearRegress function in Mathematica was used to extract the coefficients for the semiempirical equation 5-33 using experimental data. NonLinearRegress uses the Levenberg-Marquardt algorithm [75]. The results were also verified with the FindFit function of Mathematica which also uses a nonlinear curve fitting algorithm. The experimental I-V data at different temperatures were modeled using equation 5-33 at respective temperatures. The experimental data for the UND's 6 kW PEM electrolyzer system at different temperatures with the fitted models is shown in Figure 56. The temperatures have +/- 0.2 °C error margin and for simplicity they have been rounded to whole numbers. The CTC value for the cathode is assumed to be equal to 0.5 while fitting the semiempirical equation with the experimental data. But, the anode charge transfer coefficient has been found to vary with temperature as shown in Figure 55 [65].The CTC value for the anode had been reported to vary from 0.1 to 0.6 [18, 76]. The varying CTC value for the anode was used for this modeling.

A semiempirical model represented by equation 5-33 was used to fit the experimental I-V characteristics at different temperatures. The equation coefficients were extracted using the nonlinear regression method. The fitted models using equation 5-33 for each temperature I-V data are shown in Figure 56.

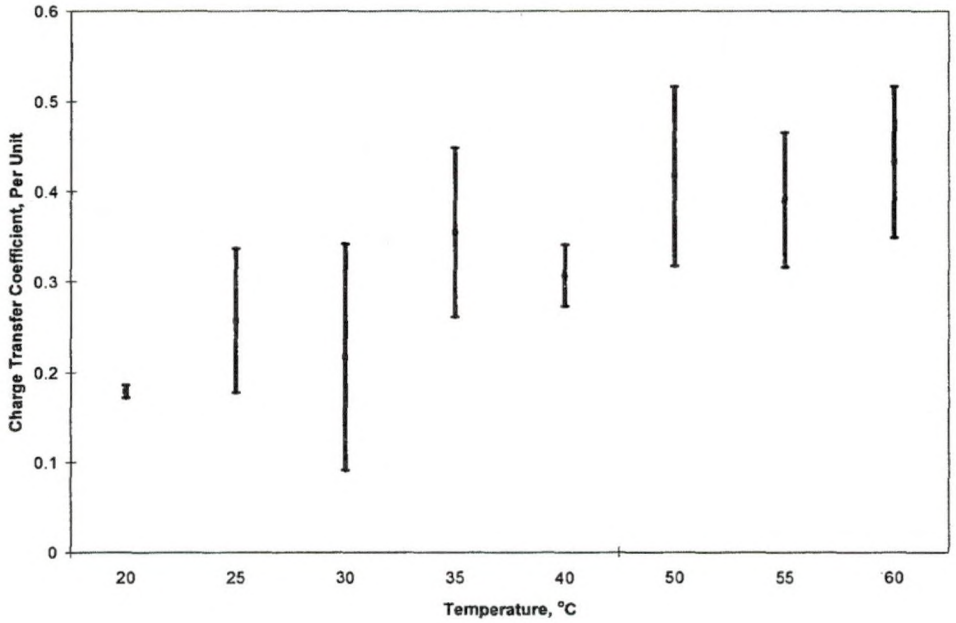

Figure 55: Variation of the anode charge transfer coefficient with temperature [65]

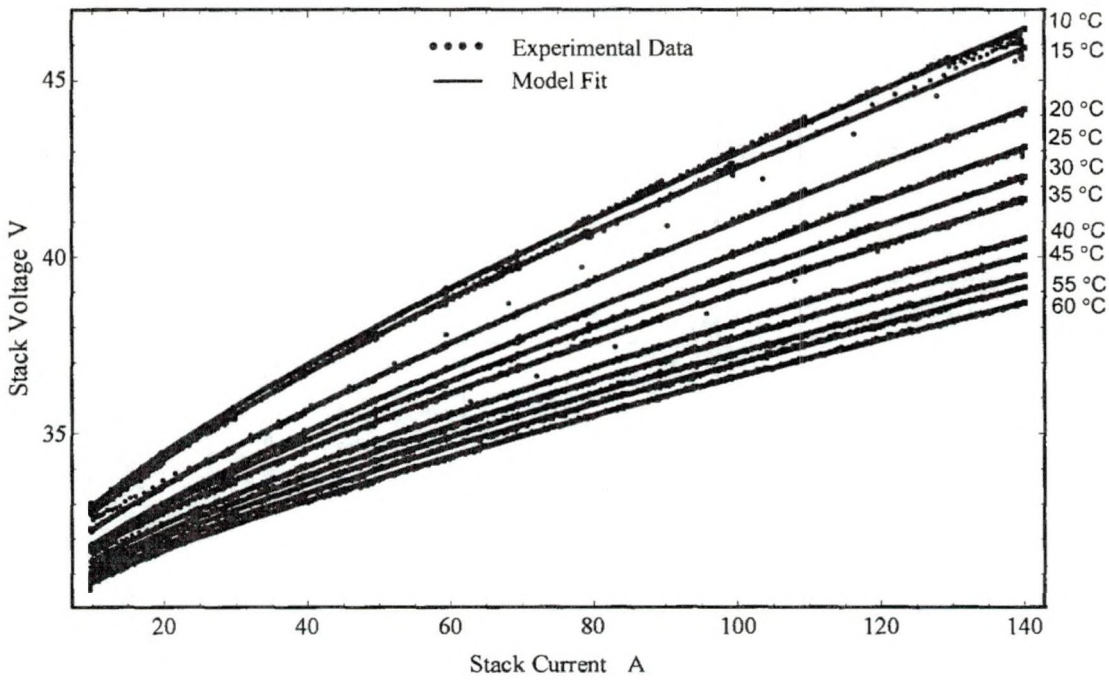

Figure 56: Fitted model with experimental I-V data at different temperatures.

Electrolyzer stack parameters such as the anode and cathode exchange current densities were employed as equation coefficients for modeling the experimental I-V characteristics. The extracted parameters from the modeling efforts are summarized in Table 5. Both the anode ($j_{A,o}$) and cathode ($j_{C,o}$) exchange current densities showed an upward trend with increasing temperature which agrees with the literature[6]. For platinum based electrodes, the exchange current density at the oxygen electrode is 10^{-9} – 10^{-12} A cm^{-2} and that of the hydrogen electrode is 1 x 10^{-3} A cm^{-2} [71]. The exchange current density depends on the electrochemically active surface area and the temperature at the electrode surface. The values in Table 5 for the exchange current densities at the hydrogen (cathode) and oxygen (anode) electrodes showed close agreement with the literature values [18,66,71].

Table 5: Extracted parameters from modeling experimental data

Temperature °C	$j_{A,o}$ (A cm^{-2})	$j_{C,o}$ (Acm^{-2})	σ (Scm^{-1})
10	0.76 x 10^{-5}	0.18	0.058
15	1.11 x 10^{-5}	0.14	0.060
20	1.45 x 10^{-5}	0.27	0.063
25	2.93 x 10^{-5}	0.21	0.065
30	2.00 x 10^{-5}	0.32	0.073
35	2.32 x 10^{-5}	0.23	0.073
40	3.29 x 10^{-5}	0.26	0.085
45	3.87 x 10^{-5}	0.24	0.087
50	4.21 x 10^{-5}	0.24	0.092
55	4.80 x 10^{-5}	0.32	0.093
60	4.93 x 10^{-5}	0.39	0.096

The membrane conductivity, σ, was found to increase with temperature as mentioned in the literature [77]. Figure 57 shows a linear increase in conductivity with temperature. This rise in conductivity was modeled as a function of temperature in °C and can be represented by

$$\sigma = 0.048 + 8.15 \times 10^{-4}\, t + 5.11 \times 10^{-7}\, t^2 \qquad 5\text{-}35$$

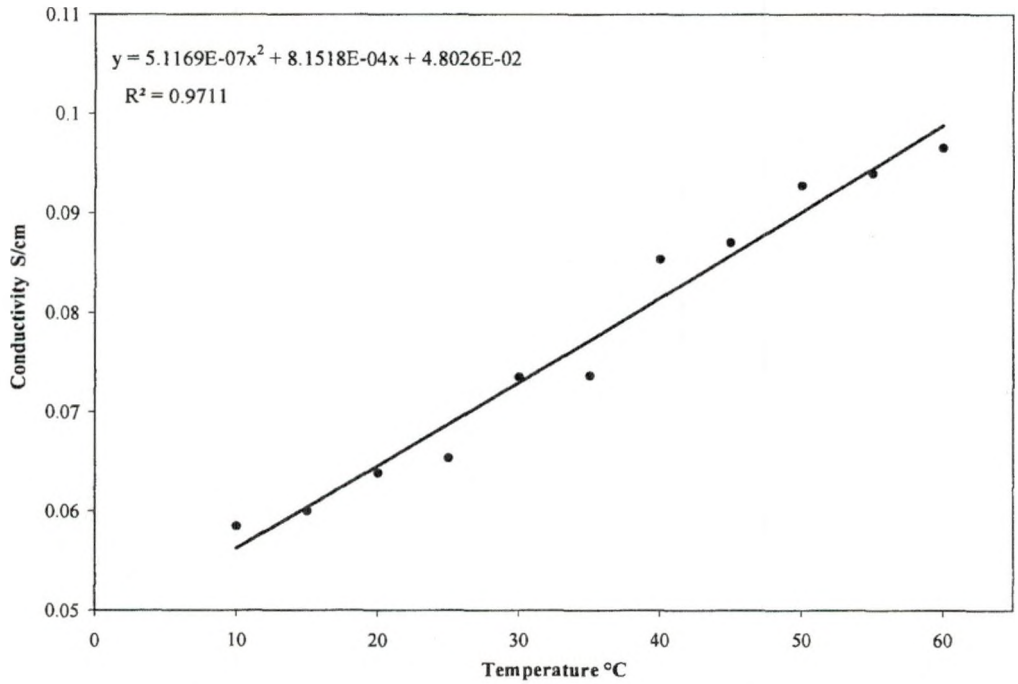

Figure 57: Variation of membrane conductivity with the temperature

The nonlinear curve fitting algorithm method with the semiempirical equation 5-33 developed in this work allows the proprietary values of membrane thickness, conductivity, and the anode and cathode exchange current densities to be determined from experimental I-V characteristics. The use of temperature and pressure dependent Nernst potential in the semiempirical equation helps in obtaining more accurate determination of the electrolyzer cell and stack parameters. The higher heating value voltage, reversible voltage, and Nernst voltage when represented as a function of temperature, can help in future simulations to obtain physically more significant I-V characteristics at different operating conditions.

CHAPTER 6

HYDROGEN CONDITIONING AND ELECTROCHEMICAL COMPRESSION

6.1 Hydrogen Dew point Control

6.1.1 Background

The low volumetric energy density of hydrogen can overcome by storing hydrogen in compressed gaseous form. Mechanical compressors used to achieve this compression require dry hydrogen. Also, some hydrogen applications such as fuel cells, metal storage cylinders, and power plant electric generator cooling require hydrogen gas with a low dew point. The power plant electric generator cooling using hydrogen gas require a dew point between -40 and 0 °C [78, 79]. Compressed storage in metal cylinders requires a low hydrogen dew point to prevent water condensation inside the cylinder to avoid the tank corrosion which can result in a leak or other tank failures. The composite fiber storage tanks are free from the corrosion problem due to water content in hydrogen, however equipment both upstream and downstream can get affected with the water present in hydrogen [80].

Distributed Energy System's (DES) (Formerly Proton Energy System) PEM electrolysis equipment utilizes an adsorption drying system to remove water vapor from the hydrogen product gas. The electrolysis system built at UND's renewable hydrogen test facility utilizes a two-tube desiccant drying system to achieve a dew point of product hydrogen gas at -65 °C. The two-tube desiccant system uses one tube at a time to dry the hydrogen from the PEM electrolyzer stack. The 10% of the dried hydrogen from one tube

is diverted to another tube to remove the water from the adsorbent. This hydrogen with water vapor is then vented which result in overall system efficiency loss. UND's PEM electrolysis system is capable of producing approximately 2 kg per day of hydrogen (1 $Nm^3\ hr^{-1}$). The loss of the produced hydrogen can account to 0.2 kg per day (26,840 BTU or 7.86 kWh based on HHV). Based on the nearly constant hydrogen system pressure and fixed orifice design of the desiccant drier, roughly 0.1 $Nm^3\ hr^{-1}$ of dry hydrogen will be consumed regardless of operating current. This impacts electrolyzer efficiency more when operating at lower current densities by consuming a larger percentage of the hydrogen product gas [80].

An alternative method to reduce and control the dew point of hydrogen utilizing the thermoelectric coolers (TEC) was proposed by Harrison [6]. The idea was to use TECs to cool the saturated hydrogen gas by passing it through the large surface area cold plates, allowing the water vapor to condense and then remove condensate using coalescing filters. This TEC based design may offer an alternative drying option for hydrogen, with the ultimate goal of improving the efficiency which reduces the overall cost of PEM electrolyzer systems and thus the dollars per kg of hydrogen product gas. The two-stage cold plate and thermoelectric cooler design can offer other operational benefits over desiccant system, such as continuous operation without need for changing exhausted desiccant, compact system with better design, precise control over hydrogen dew point using feedback temperature control system. The TEC based system may offer other benefits depending on the application for which the hydrogen is being produced. Detailed system design, TEC working principle, thermodynamic modeling and

comparison of TEC system with two tube desiccant system is summarized by Harrison [6].

6.1.2 Experimental Setup

The following describes the experimental system tested at UND. The proposed experimental setup is shown in Figure 58.

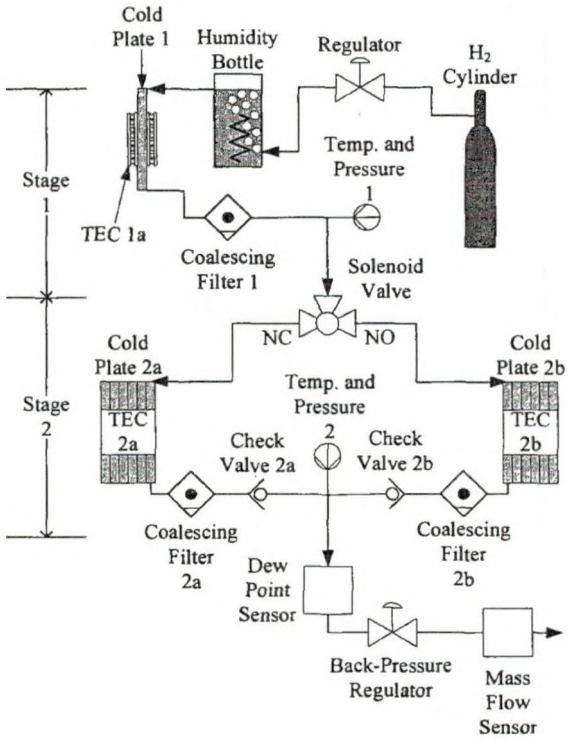

Figure 58: Proposed experimental setup [6]

The experimental setup described here differs in 'Stage 1' from what has been proposed previously [6]. Initially, the plan was to use a cooling fan for dissipating the heat from the first stage TEC. During the test runs, it was found that cooling fan is not an efficient way to remove the heat from hot side of TEC. The fan was not able to keep the hot side of TEC to the lower temperatures for the cooler side of TEC to condense the water vapor in the cold plate. After few minutes of operation, both sides of TEC were

found to be hot which was making the cold plate hot. Extreme hot temperature can damage the TEC. Therefore, a water cooling block was used instead of cooling fan for the first stage cold plate assembly (CPA). A CPA consists of a high-surface-area cold plate (CP), TEC and water-cooled heat sink. However, it was observed during the test runs that, the first stage TEC was getting to cold, below freezing, which could result in the formation of the ice to block the hydrogen flow. It was decided that the first stage TEC would be run with ON and OFF cycle by discontinuing the power supplied to it using the LabView control.

Hydrogen gas leaving a PEM stack is assumed to be fully saturated with water vapor at temperatures above ambient (20 °C). Output hydrogen from a PEM stack passes through the high pressure hydrogen-water separator to remove liquid water by gravity. This saturated gas stream feeds into the first stage cold plate assembly. A back-pressure regulator at the output of the system is adjusted to achieve the desired hydrogen flow rate. The entire system incorporates three cold plate assemblies in two stages. For this proof–of–concept testing, an operating pressure of 50 psig, flow rate of 1 $Nm^3\ hr^{-1}$, and saturated hydrogen gas around 35 °C is used for the TEC-based drying system.

Figure 59 shows the actual experimental system, which uses two stages of cooling to reduce and control the dew point to a theoretical -35 °C. Stage 1 has saturated hydrogen gas as its input and uses one TEC module to reduce the dew point to 5 °C. Stage 2 requires two CPAs in parallel to achieve dew points below the freezing point. A temperature feedback control loop will allow maintaining these temperatures at a desired value. Coalescing filters are located immediately downstream of each CPA to remove liquid water from the process. The TECs were oversized in the experimental system as

compared to calculated results to account for heat losses. The calculated results using thermodynamic principles are summarized in [80]. Temperature, pressure, dew point and mass flow sensors are used to monitor the system parameters. The capital cost of proposed TEC system based on retail prices is approximately same as Distributed Energy Systems desiccant drying system that was obtained to perform comparison testing.

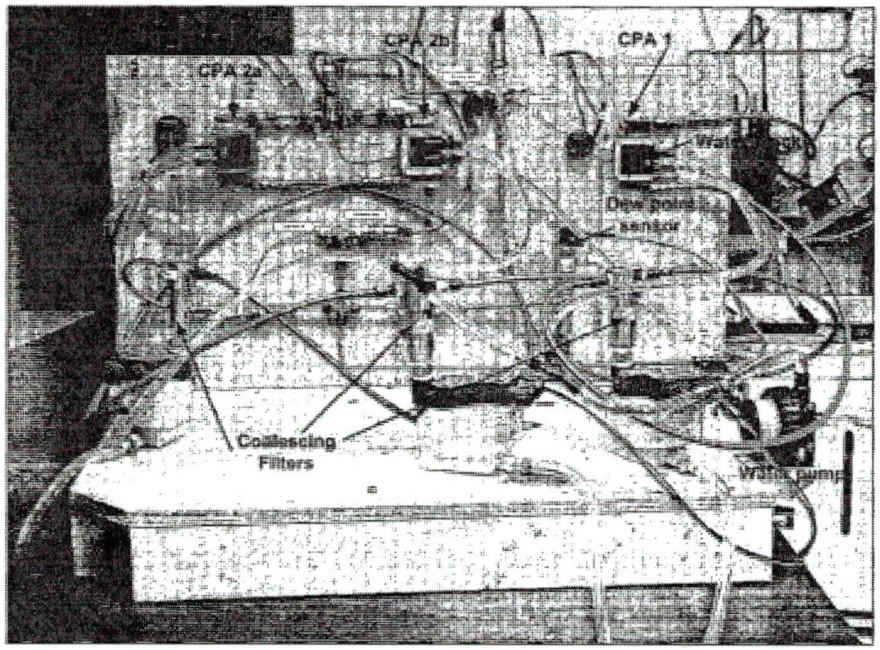

Figure 59: Actual experimental setup for two stages TEC based dew point control system for hydrogen from PEM electrolyzer.

6.1.3 Theory of Operation

In Stage 1, the saturated hydrogen gas from the high pressure hydrogen water separator passes through cold plate 1 (CP1) where the water vapor is condensed. The goal of Stage 1 is to remove most of the water vapor in the hydrogen gas and allow the second stage to operate at lower temperatures for longer periods of time before switching between the parallel CPAs branches. The operation and temperatures of the TECs are

controlled using Lab View programming. Care is taken to avoid freezing water in the channels of first-stage TEC by discontinuing the power supplied to it using LabView control. However, instead of using the ON and OFF cycle, the continuous operation of the first stage TEC can be possible by lowering the current supplied to TEC using the fuzzy control. The 3-way solenoid valve at the beginning of Stage 2 switches between the two parallel-connected CPAs, CPA2a and CPA2b. Temperatures below freezing are expected in Stage 2.

The hydrogen pressure is monitored at the inlet and the outlet of Stage 2. When a predetermined pressure differential is developed between Stage 2 input and output, the hydrogen gas is diverted to the parallel CPA (for example, from CPA2a to CPA2b). Next the polarity of TEC 2a is reversed to melt the ice from the restricted CP channels. When the flow in CP 2b becomes restricted, gas flow is diverted back to CP 2a and the process repeats. In the case of TECs, the heating process is faster than the cooling process. Hence, during the melting stage the cold plate gets overheated which results in longer time to cool down. Temperature feedback for process optimization using fuzzy controller can be utilized during the melting stage to avoid over-heating the CP and to anticipate the crossover to cool the CP in advance.

Water-cooled heat sinks were chosen based on their exceptional ability to dissipate the high density of heat pumped/generated by TEC devices and the readily available source of water and DC electricity in an electrolysis system. This approach seemed to be a natural selection for dissipating the sensible and latent heat required to condense and desublimate water vapor from the hydrogen product and remove the waste heat of the TECs.

System operation is monitored and controlled with a computer-based data acquisition system. A LabView-based user interface acquires and archives analog inputs and controls the operation of the solenoid valve, water pump, and polarity control and operation of the TEC devices. Pressure, temperature, dew point and mass flow sensors monitor the performance of the system. The enclosure shown in Figure 60 controls the operation of TEC system with the help of the data acquisition system. The enclosure consists of two 15 V and one 12 V linear DC power supplies, seven DC 6321 buffer or I/O modules, one AC 6421 buffer, and four electromechanical relays (EMR). All I/O modules are mounted on two MS-4 boards. 15 V DC powers supplies the required power for the TECs operation while a pump is powered with 12 V DC supply. The logic signal generated by SCXI 1163 Digital Output is send to the I/O modules which acts as switch. The I/O modules turn the pump, SV and TECs ON and OFF. TEC 2a and TEC 2b operate in normal and reverse polarity mode as explained earlier. The electromechanical relays help reversing the polarity of the TECs by reversing the polarity of the voltage supplied to them. As shown in Figure 60, EMR 1 and EMR 2 help running the TEC 2b in reverse and normal polarity mode respectively. EMR 3 and EMR 4 control the polarity of TEC 2a in reverse and normal mode respectively. The detailed wiring diagram and operating procedure for dew point control system is summarized in Appendix C.

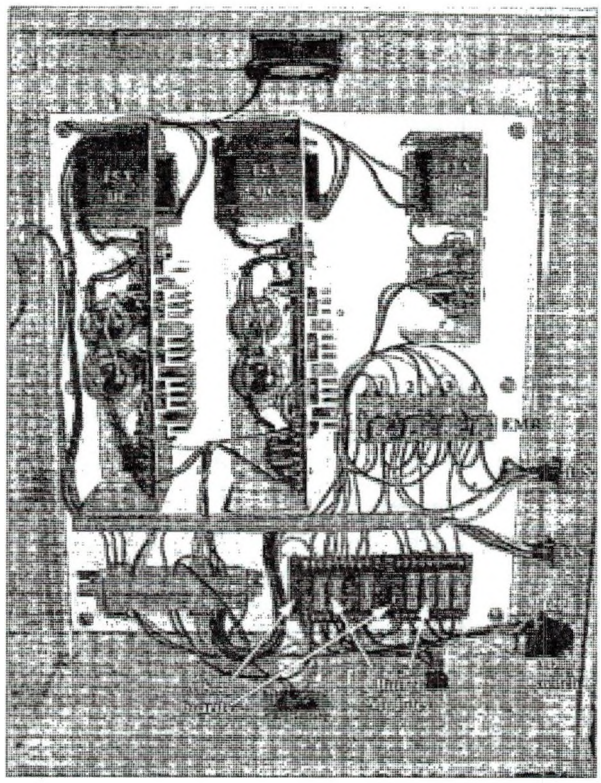

Figure 60: TEC enclosure to control the dew point control system

6.2 Electrochemical Hydrogen Compression

The need for clean sustainable energy system and advancement in fuel cell technologies and usage in recent years has attracted more attention to an efficient renewable hydrogen production and compression technologies. Hydrogen as an energy carrier suffers from its low volumetric energy density in transition to a hydrogen economy. The most technically challenging barrier in building a hydrogen economy is the development of safe, compact and cost effective hydrogen storage technology [81]. As discussed earlier in Chapter 2, hydrogen can be stored by several methods including gaseous hydrogen storage, as a liquid, in metal, in glass micro spheres or in carbon nanotubes. Each storage method has different advantages and disadvantages. Gaseous

hydrogen has low volumetric energy density [about 25% of that of the gasoline] but remains the preferred method to store the hydrogen for specific applications. The low volumetric energy density of hydrogen can be improved by compressing it at high pressure. This compression achieved with an energy efficient hydrogen compressor can improve energy efficiency of the system [82]. Compressed gaseous storage is a well-known and economical method to store hydrogen. The most common approach of mechanical compression is limited due to obstacles such as high energy use, wear-and-tear of moving parts, hydrogen embrittlement, noisy operation, bulky equipment, and contamination of the gas, typically with compressor lubricants [7]. Use of an electrochemical system such as PEM cells is an alternative means to compress hydrogen. In low power applications, the efficiency of PEM cells is high compared to mechanical compression [83]. The other advantages of an electrochemical system approach are noiseless operation, purified hydrogen and simplicity of the system cooling [84]. These advantages make it a promising hydrogen compression technology for the future. An electrochemical compressor can also serve as an intermediate step to mechanical compression to increase compression capacity and energy efficiency by reducing number of compression stages [85].

6.2.1 Principle of Electrochemical Compression

Figure 61 explains the working principal of electrochemical compression. The application of a potential difference causes hydrogen at pressure P_A to oxidize at the anode to protons (H^+), transport through the polymer membrane and reduce to hydrogen at the cathode at pressure P_C.

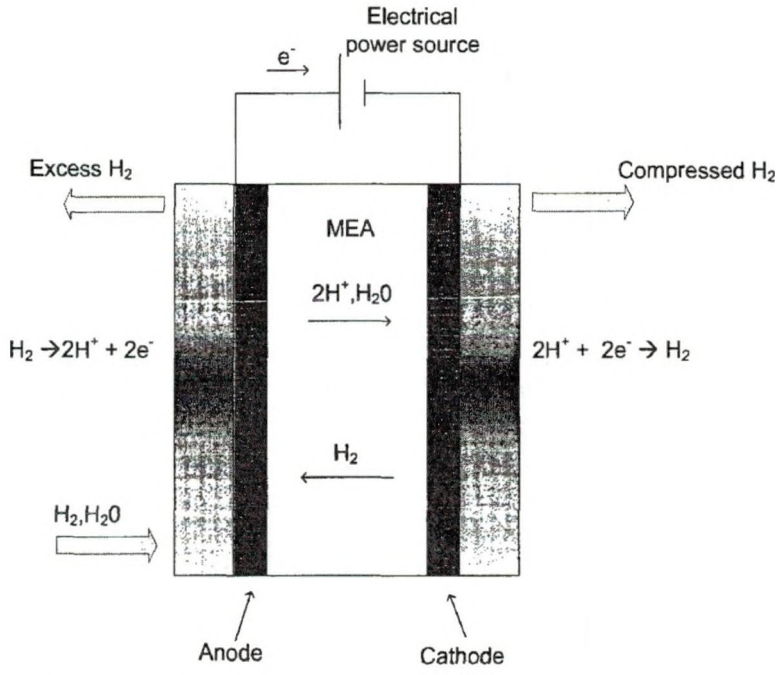

Figure 61: Polymer electrolyte membrane (PEM) hydrogen compressor

The hydrogen being produced by proton reduction in the confined cathode space is compressed and discharged at high pressure. As the polymer membrane is selective for hydrogen ion, inert gas components can not cross the membrane. Hence, these components are removed from the compressed gas. Moreover, since the electrochemical compressor does not have any moving parts, it minimizes the maintenance. Flexibility in sizing of cells allows this compressor to achieve a high efficiency [85].

6.2.2 Proposed Experimental Setup

Figure 62 shows the proposed experimental setup for electrochemical compression of hydrogen from the PEM electrolyzer system. The membrane of the electrochemical cell must be well hydrated to maintain the ionic conductivity; hence the hydrogen must be humidified before feeding to the anode. This can be achieved either by humidifying hydrogen from the storage tank using a humidity bottle or using the product

hydrogen gas from the PEM electrolyzer system, conditioned to compress electrochemically. The product hydrogen from PEM electrolyzer can be assumed to be 100% saturated. It can be conditioned using a thermoelectric cooling system, discussed in the earlier part of this chapter, to the required humidity level to electrochemically compress using a PEM cell assembly [80].

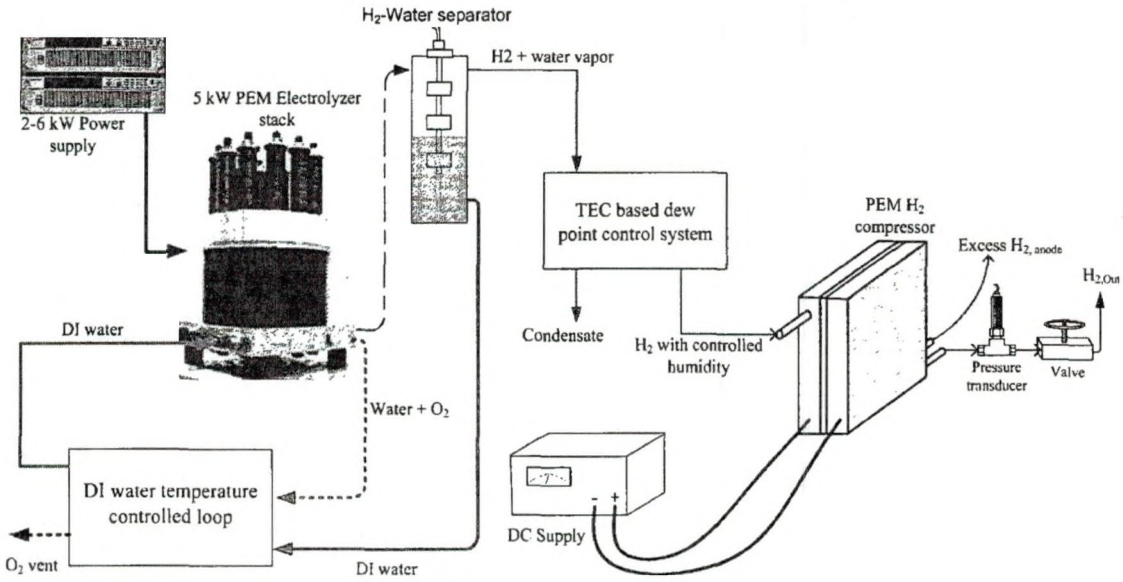

Figure 62 : Proposed experimental setup for electrochemical compression

6.2.3 Discussion

Water Management

To maintain the ionic conductivity, the electrochemical cell membrane must be hydrated. The proton conductivity is directly proportional to the water content in the membrane. Hydrogen from the storage tank must first be humidified before feeding to the anode to avoid the dehydration of the membrane. If using the product hydrogen from PEM electrolyzer system, it must be conditioned to maintain required humidity level. Water in the hydrogen stream should not be so high as to flood the electrodes. The water

crossing the membrane accumulates at the cathode, since the protons dehydrate during the formation of hydrogen. Because of the pressure difference, this water diffuses back from cathode to the anode. To avoid flooding at the electrodes, the inlet water at the anode must be controlled carefully with less water fed through anode inlet. Water vapor related to the saturation pressure at operating temperature and fed with hydrogen is sufficient to maintain the membrane saturation and ionic conductivity.

Membrane Electrode Assembly

Because of high pressure difference across the membrane, a special construction consideration is necessary for the anode and cathode flow fields to stabilize the membrane electrode assembly (MEA) of the PEM cell compressor. Figure 63 shows the components of single cell electrochemical compressor. It consists of the anode and cathode endplates, seals, and flow field for the anode and cathode with MEA. The deformation of MEA is unavoidable at high pressures, for this reason it is necessary to construct the cathode flow field with a special flexible graphite sheet. The flexibility of graphite compensates the deformation of the MEA. It helps to keep to stable electric contact of cell housing, flow fields and MEA [84].

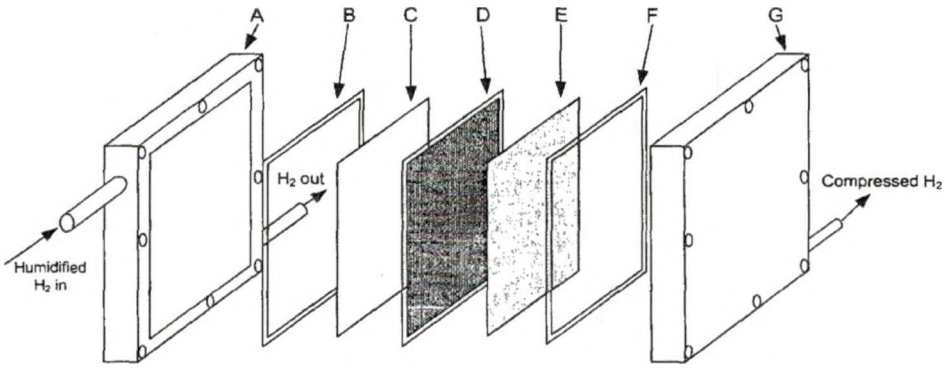

A- anode endplate
B,F- seal
C-anode flow field with gas diffusion layer
D-membrane electrode assembly
E-cathode flow field with gas diffusion layer
G-cathode endplate

Figure 63: Single cell of the electrochemical compressor

Back Diffusion of Hydrogen

The pressure difference between the electrodes promotes the back diffusion of molecular hydrogen from the cathode to the anode side. The back diffusion rate is important for efficiency calculations, as the compressor efficiency decreases with increasing back diffusion. The back diffusing hydrogen that increases the pressure at the anode side varies with varying cathode pressure and cell temperature. This back diffusion increases linearly with increasing pressure difference across the membrane [83]. This back diffusion rate can be measured by amount of compensating current to keep the anode pressure constant [84]. Higher temperature and pressure difference increases the hydrogen back diffusion as shown in Figure 64.

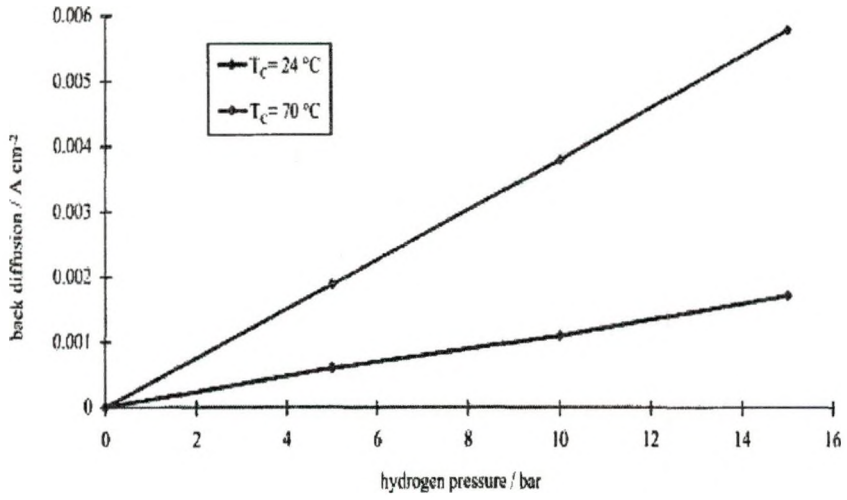

Figure 64 : Hydrogen back diffusion versus pressure difference at different temperature [83] *.

The relation between gas diffusion rate (dn/dt) and membrane thickness (x) is given by diffusion coefficient (Dn).

$$\frac{dn}{dt} = -DnA\frac{dc}{dx} \qquad 6\text{-}1$$

The hydrogen back diffusion can be determined at open circuit voltage and $Pc > P_A$. Because of the additional back diffused hydrogen the pressure at the anode increases. This additional increase has to be compensated by a reduction of total anode pressure. This can be done by the pumping of hydrogen from the anode to the cathode via protons (H^+) by adding more current to the anode. This compensation current can be given by Faraday's law as follows [84]

$$\gamma_{a-c}^{H^+} = \frac{i_{a-c}}{zF}\frac{V_0 T}{T_0} \qquad 6\text{-}2$$

* Reprinted from *Electrochimica Acta*, Vol. 43,No. 24, B.Rohland, K. Eberele et al; " Electrochemical hydrogen compressor", pp.3841-3846,1998, with permission from Elsevier.

where, $\gamma_{a-c}^{H^+}$ represents the migration of protons from anode to the cathode because of applied potential (ml min^{-1}), z is number of charge transfer, F is Faraday constant (96,485 C mol^{-1}), V_0 is standard molar volume (22.4 L mol^{-1}), and T_0 is a standard temperature (273.14 K).

In the most likely case the anode is at atmospheric pressure, then the excess pressure due to back flow of hydrogen results in gas flow out of anode outlet. The compensation current supplied by an external source equalizes the back diffusion current to prevent hydrogen escape from anode. The back diffusion can not be avoided completely and as it decreases the pressure difference across the membrane, it decreases the efficiency of the hydrogen compressor.

6.2.4 Mathematical Modeling and Results

Nernst Potential

The total voltage of the PEM cell includes the Nernst potential, the polarization voltage and the IR drop or ohmic resistance. The Nernst potential depends on the pressure difference between the cathode side and the anode side. This equilibrium potential is given by equation 6-3.

$$E_{Nernst} = E_0 + \frac{RT}{2F} \ln\left(\frac{P_C}{P_A}\right) \qquad 6\text{-}3$$

where, P_C and P_A is the cathode and anode pressure respectively, E_0 is a standard potential.

Overpotentials

These are the irreversibilities that have to be overcome by applied potential to a PEM cell before oxidation and reduction of hydrogen can begin. For a PEM cell working

as an electrochemical compressor only activation and ohmic overpotentials are significant. The activation polarization is the overpotential that has to be overcome by an electrochemical reaction before the reaction can occur. This process is modeled by Tafel equation. The Tafel equation for an electrochemical process with non zero activation polarization at each electrode can be described by following equations

$$E_{Act\,Anode} = \frac{RT}{2\alpha_a F}\ln\left(\frac{i}{i_{oa}}\right) \qquad 6\text{-}4$$

$$E_{Act,Cathode} = \frac{RT}{2\alpha_c F}\ln\left(\frac{i}{i_{oc}}\right) \qquad 6\text{-}5$$

where, i is the operating current density in A cm^{-2}, α is the charge transfer coefficient at the anode and cathode and is assumed equal to the symmetry factor (i.e. 0.5) for both electrodes. The magnitude of activation overpotential is a function of the exchange current density at the anode (i_{oa}) and exchange current density at the cathode (i_{oc}). The exchange current densities are a measure of the activity at the anode and cathode prior to the application of potentials. Generally, the kinetics of hydrogen electrodes are rapid. But in case of PEM cell compressor, a slightly slower kinetics of the reduction at the cathode can be observed as compared to the oxidation at the anode [84]. This can be explained due to slower kinetics of the Volmer–Tafel mechanism [84]. Theoretically calculated anode and cathode overpotentials increase with increasing current densities as shown in Figure 65. The anode and cathode exchange current densities from literature [86, 66] are used for this modeling work.

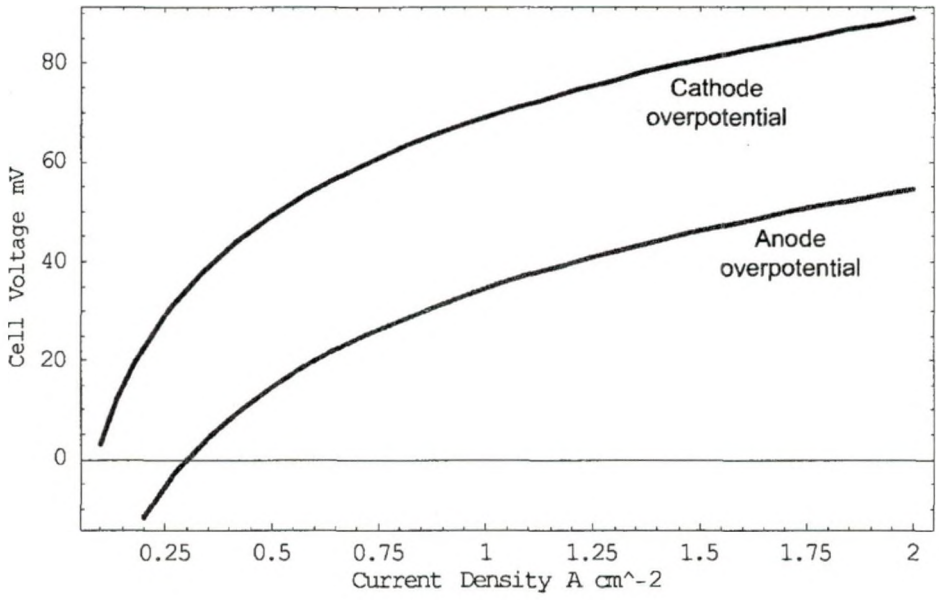

Figure 65: Polarization of PEM compressor electrodes

The constant resistance experienced across the applied voltage to the PEM cell is represented as ohmic overpotential. The magnitude of ohmic loss depends on electrode material, electrolyte material and interface between electrode and electrolyte. Manufacturing processes and techniques are an important factor in keeping this overpotential minimal.

The ohmic overpotential is modeled by the following equation,

$$E_{Ohmic} = \frac{\varphi}{\sigma} i \qquad 6\text{-}6$$

where, φ is the membrane thickness (cm), σ is the cell conductivity (S cm^{-1}), and i is the operating current density. The membrane conductivity is a function of temperature. For this work, the conductivity is estimated using following equation [65]

$$\sigma = 0.0007 \times t + 0.0574 \qquad 6\text{-}7$$

where, t is temperature in °C.

The total cell voltage of PEM cell compressor includes Nernst potential, the polarization voltage and the ohmic losses and therefore can be represented theoretically by equation (6).

$$E_{Total} = E_{Nernst} + E_{Act} + E_{Ohmic} \qquad 6\text{-}8$$

Combining equations 6-3 through 6-6 the cell potential is given by

$$E_{Total} = \mathrm{E}_0 + \frac{\mathrm{RT}}{2\mathrm{F}}\ln\left(\frac{P_C}{P_A}\right) + \frac{\mathrm{RT}}{2\alpha_a \mathrm{F}}\ln\left(\frac{\mathrm{i}}{\mathrm{i}_{0a}}\right) + \frac{\mathrm{RT}}{2\alpha_c \mathrm{F}}\ln\left(\frac{\mathrm{i}}{\mathrm{i}_{oc}}\right) + \frac{\varphi}{\sigma}\mathrm{i} \qquad 6\text{-}9$$

where the dry membrane thickness (φ) used is 178 μm (for Nafion™ 117) and the charge transfer coefficient at anode and cathode is 0.5.

Calculated total cell voltage and Nernst potential over a pressure range is shown in Figure 66. To simplify modeling work, the anode pressure is assumed to be constant at 1 atm (14.7 psi). The calculations were done at 60°C.

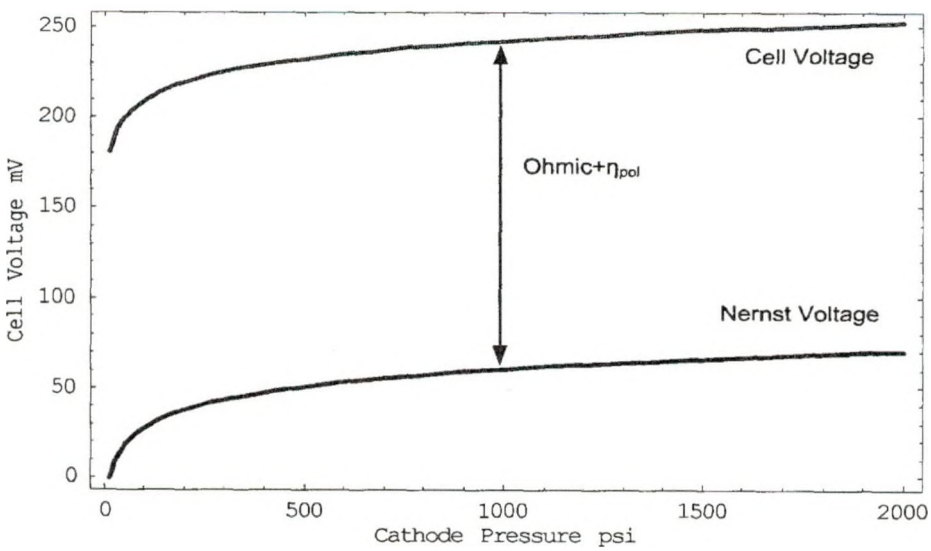

Figure 66: Cell voltage versus hydrogen pressure at the cathode.

However, in a real situation the assumption of constant anode pressure can not be true. Because of the high pressure difference across the membrane promotes the back diffusion of molecular hydrogen from cathode to the anode side as discussed earlier. The back diffusion rate is important for efficiency calculations, as the compressor efficiency decreases with increasing back diffusion.

As can be seen from Figure 67, the main contributor to cell voltage are ohmic and activation polarizations. Efforts were taken to estimate the contribution of each of these polarizations towards the total cell voltage at various operating current densities. Figure 67 shows these contributions to the total cell voltage. The ohmic voltage almost amounts to the cell voltage.

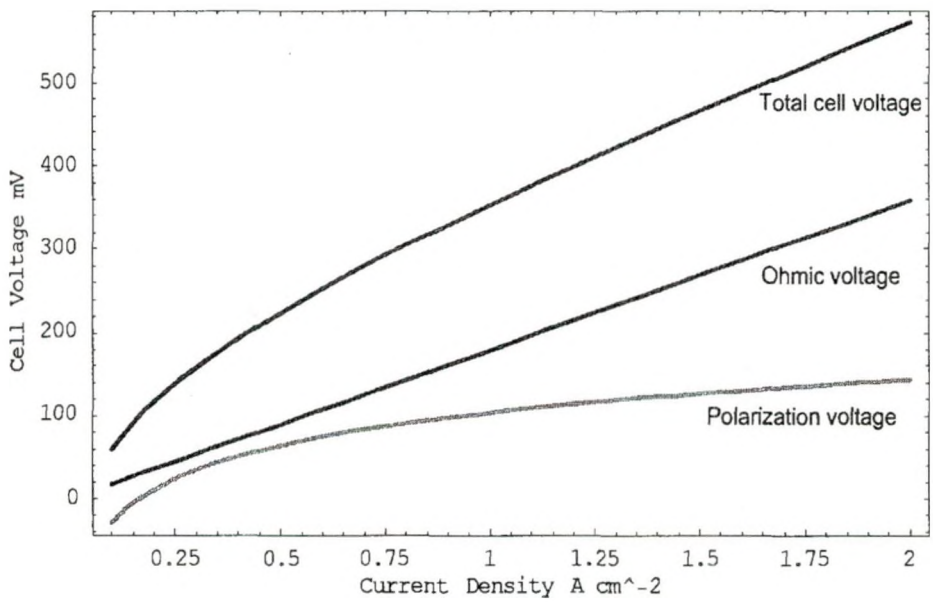

Figure 67: I-V characteristics of PEM cell compressor.

More energy is required to compress the same amount of hydrogen to a higher pressure. Therefore it is expected that cell voltage increases with increased product pressure. To verify this, cell voltages were calculated at varying cathode pressures and

plotted at different operating current densities as shown in Figure 68. For these calculations the anode pressure is assumed constant at 1 atm (14.7 psi) and product pressure at the cathode is varied from 250 psi to 2000 psi.

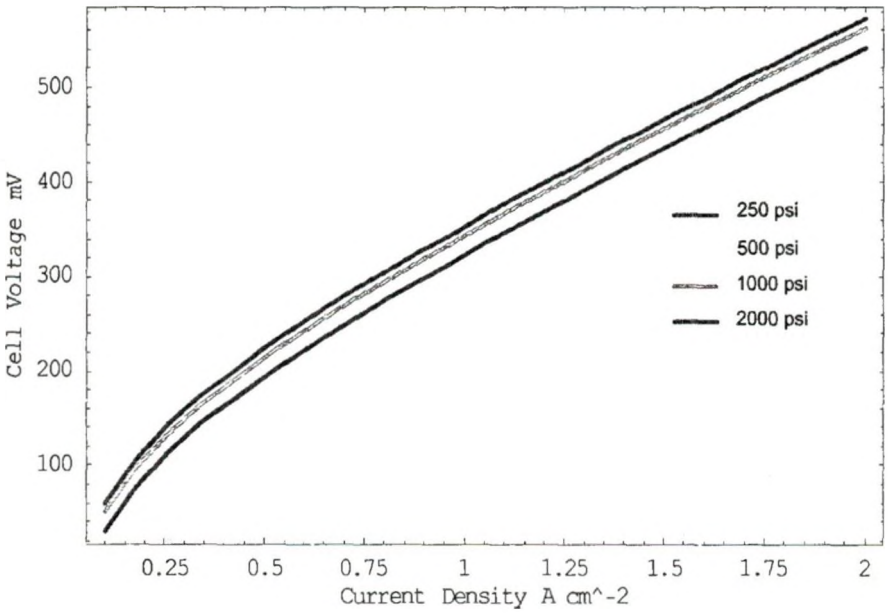

Figure 68: Cell voltage of PEM cell compressor at various product pressures.

As expected, a higher cell voltage at higher pressure shows more energy requirement to compress hydrogen to an elevated pressure. In practical situations, the voltage differences are small at low current densities and more significant at higher current densities [85]. Also, the experimentally measured voltage can be greater than that calculated by equations because of increased resistance of the cell. Higher pressure difference between anode and cathode causes expansion and contraction of the material inside the cell which results in increase of contact resistance and therefore leads to higher voltages [85].

Mechanical Compression Comparison

The calculation of the work required to compress the hydrogen to the high storage pressure is complicated because of the factors such as hydrogen does not behave as an ideal gas at high pressures and compression process is done in stages with cooling between these stages. Many investigators consider compression of hydrogen as an isentropic process to simplify the calculations. They assume during compression there is no heat exchange between compressor and environment and the process is reversible. Assuming hydrogen behave as an ideal gas, the isentropic work to compress hydrogen gas from pressure P_1 to P_2 is given by following equation [68].

$$W_{s\ (isentropic)} = \frac{RT_1\gamma}{\gamma - 1}\left[\left(\frac{P_2}{P_1}\right)^{\frac{\gamma-1}{\gamma}} - 1\right] \qquad 6\text{-}10$$

where, T_1 is the temperature of hydrogen in Kelvin at pressure P_1 and γ is the specific heat ratio of the gas (C_p/C_v). Specific heat ratio (γ) is assumed to be independent of temperature. For diatomic gases such as hydrogen, γ has approximate value of 1.4. But, since adiabatic hydrogen compression is not reversible process, isentropic compressor efficiency can be accounted for deviation from ideal behavior. Therefore, the actual compressor work can be given by [68]

$$W_{Actual} = \frac{W_{s\ (isentropic)}}{\eta_{adiabatic}} \qquad 6\text{-}11$$

where, $\eta_{adiabatic}$ is the adiabatic efficiency of the compression process. Its value is approximately 75% -80% [7]. Finally, the actual energy required by the compressor (i.e. electrical consumption) is calculated considering the mechanical efficiency of the compressor to be 90% [7] and is shown in Figure 69 for product pressure upto 10000 psi.

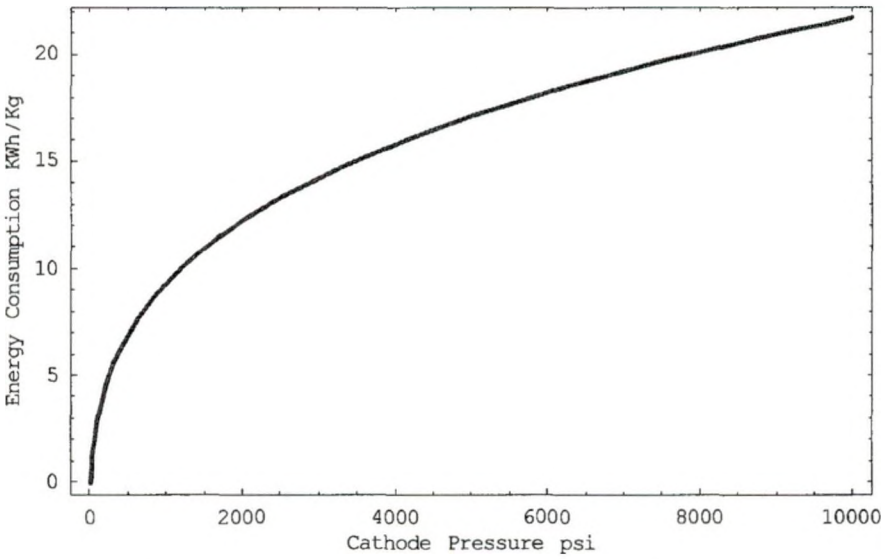

Figure 69: Energy consumption for mechanical compressor.

As can be seen from Figure 69, the mechanical compression requires more energy to compress the hydrogen gas at lower pressure ranges than at elevated pressure ranges. In other words, mechanical compression is more efficient for compressing gases from 4,000 psi to 10,000 psi than from atmospheric pressure to 4,000 psi.

Electrochemical Compression Energy Consumption

The total cell voltage for a PEM cell compressor can be calculated using equation 6-9. The work required for the compression process can be calculated at different current densities by multiplying the total cell voltage by the respective current density and total active area. The calculations were done for current density of 0.7 A/cm^2 and active area of 30 cm^2. The anode pressure is assumed to be constant at 14.7 psi. The calculations were done for inlet hydrogen flow rate of 4 kg/h. To account for real time losses the efficiency of PEM cell compressor is assumed to be 70%.

Calculated energy consumptions for both the mechanical and electrochemical compressor for a product pressure range upto 2,000 psi are shown in Figure 70. The

energy consumption for an electrochemical compression is lower than for mechanical compression at low pressure range. Therefore, the efficient electrochemical compressor can serve as an intermediate step between electrolyzer and mechanical compressor to increase the whole system efficiency. Electrochemical compression can also reduce the number of compression and cooling stages resulting in more efficient compression process.

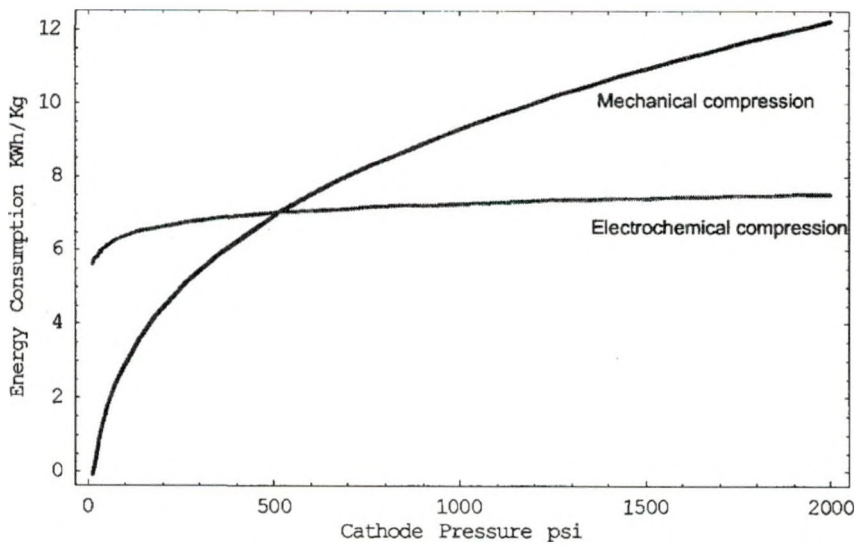

Figure 70: Comparison of energy consumption by mechanical and electrochemical compressor.

To compress the hydrogen from atmospheric pressure to 10,000 psi using mechanical compression alone theoretically requires 22 KWh/Kg of H_2 as shown in Figure 69. Calculations showed that electrochemical compression requires 7.5 KWh/Kg of H_2 energy to compress hydrogen from atmospheric pressure to 2,000 psi. If electrochemical compressor is used as an intermediate step between electrolyzer and mechanical compression to compress hydrogen upto 2,000 psi and then mechanical compression from 2,000 psi to 10,000 psi, the energy saving can be as high as 5 KWh/Kg

according to theoretical calculations. The energy required for cooling stages during mechanical compression have not been considered for these calculations. Thus, significant amount of energy can be saved using the electrochemical compressor as a primary step before the mechanical compressor to achieve the high pressurization.

CHAPTER 7

SUMMARY AND RECOMMENDATIONS

Characterization of PEM fuel cell and PEM electrolyzer stacks were performed to study the performance losses using an electrochemical investigation technique called electrochemical impedance spectroscopy (EIS). EIS was found to be an effective tool to characterize the PEM fuel cell and PEM electrolyzer at both the cell and stack level. EIS data was analyzed to differentiate the contributions of ohmic, activation and mass transport losses. It was observed that PEM cells stack level EIS results differ from cell level results.

Performance and properties of a single fuel cell were found different than the stack. Single fuel cell performance was dependent on the position of a cell in the stack and concentration of hydrogen. PEM fuel cell losses were also dependent on the operating current densities. No significant change was observed for ohmic loss for whole stack with changing currents. However, activation losses were decreased with increasing currents. The contribution of mass transport loss found to be dependent on the dominance of one of the water transport mechanisms at that current density. Mass transport losses were significant at higher currents.

The effect of experimental setup on high frequency behavior of the PEM fuel cell was observed and minimized by employing a better experimental setup. The high frequency behavior changed with the position of the cells in the stack. Therefore, it was concluded that humidity level and amount of hydrogen present at the cells should have an

effect on the high frequency behavior of the cells. Larger AC signal amplitude was used for EIS studies of PEM fuel cell stack than single cell EIS studies reported in the literature. The results of EIS experiments were found a function of stack run time. The optimum stack run time for the studied PEM fuel cell stack to achieve the steady state was concluded to be an one hour.

In the absence of an off–the–shelf power supply capable of performing EIS studies of a 6 kW PEM electrolyzer at a rated current of 140 Adc for a frequency range of 20 kHz to 0.5 Hz, electrolyzer EIS studies were performed successfully using the FRA, modified linear DC power supply (20 Hz to 0.5 Hz) and a custom build transformer core (20 kHz to 1 kHz). EIS tests results confirmed that the electrolyzer is more efficient at elevated operating temperatures. High output pressure of hydrogen is desirable to reduce the compression cost. However, EIS tests results for the electrolyzer showed more losses with increasing output pressure resulting in lower efficiency.

The performance of a 6 kW PEM electrolyzer was modeled using a semiempirical equation consisting of a temperature and pressure dependent Nernst potential, derived from thermodynamic principles. Temperature dependent equations for reversible potential and higher heating values voltage helped in obtaining accurate electrolyzer parameters and electrical efficiency. Anode and cathode exchange current densities and membrane conductivities at various temperatures were extracted using the semiempirical modeling.

A novel technique based on thermoelectric coolers to control the dew point of hydrogen was developed and tested. The user interface to control this dew point system was developed using LabView. An alternative method to an energy intensive mechanical

compression of hydrogen using the PEM cell compression was evaluated using theoretical modeling. The energy comparison study of the PEM cell compressor with mechanical compressor showed the energy saving by using PEM cell compressor before the mechanical compressor, by reducing the number of compression stages.

Recommendations

UND's Renewable Hydrogen Test Facility has two 1.2 kW PEM fuel cells. For this study, only one fuel cell was used for characterization. However in real situations, two or more fuel cells can be put in parallel or series to balance the larger loads. Two 1.2 kW PEM fuel cells can be connected in parallel to perform the dynamic analysis and EIS tests to study their performances. If operated in parallel, an electronic controller can be build for optimal power distribution depending on the performances of the fuel cells.

The whole impedance spectrum for the electrolyzer for a frequency range of 20 kHz to 0.5 Hz can be obtained using the three power supply setups as explained in the electrolyzer EIS experimental setup. It is recommended that commercial power supplies capable of performing EIS experiments for the range of 1.5 kHz to 15 Hz be sought to allow the full EIS spectrum to be obtained. The existing Xantrex power supply 'PS2' can also be modified the same way as 'PS1' to make it capable of performing the low frequency (20 Hz to 0.5 Hz) EIS tests. These modified power supplies can be connected in parallel to perform the electrolyzer EIS tests up to its rated current (140 A).

EIS studies of a 6 kW PEM electrolyzer can be performed for whole stack, group of cells and single cells. The electrolyzer has 20 cells with the pick off points for voltage measurement at each cell. The performances of single cell can be evaluated and compared to that of the whole stack and group of cells.

It is recommended to observe the water level in the smaller external water tank after shutting the electrolyzer system and before leaving the lab. Sometimes even after the proper shutdown of the electrolyzer system, one of the solenoid valves may not get tightly closed and water from the oxygen-water separator can start flowing into the external tank. This downward water flow may cause the external tank to overflow and water spill on the lab floor. In the case of the system going into the fault condition, the system must be restarted to follow the proper shutdown procedure summarized by Harrison [6].

A TEC based dew point control system for hydrogen can be made more efficient by employing fuzzy logic control and a temperature feedback loop. This can avoid the freezing of water in the channels of the first stage TEC and overheating of the second stage cold plates during the melting stage of the operation. The fuzzy logic can control the current supplied to the TEC depending on their temperature feedback.

APPENDIX A

Operating Procedure for Fuel Cell EIS Tests

The following steps should be followed to perform the EIS tests of 1.2 kW PEM fuel cell. The fuel cell start-up steps are as follows:

1. Connect the dc power supply (40 V and 10 Amp) to fuel cell as shown in Nexa™ fuel cell manual.
2. Connect fuel cell to computer (COMP 2) through RS 232 cable. Nexa™ fuel cell has RS 485-RS232 converter. Connect RS 232 cable to this converter and one of the COM ports of COMP 2.
3. Run the NexaMON OEM Labview program from Start-All Programs-NexaMON OEM-NexaMON OEM on the COMP 2
4. Adjust the supply voltage of dc power supply in the range of 24 V to 27 V. The supply voltage should not be more than 27 V, else fuel cell will go into error mode with 'Non-Restarting Error'. Refer the fuel cell manual for the further details of the error.
5. Make sure RS 485-RS232 converter is powered up.
6. Turn on the dc power supply, then LED on the control board will be on.
7. Select the proper communication port such as COM1, COM2, ... from 'Serial Port' selection under COMMUNICATION box located right bottom corner of the NexaMON OEM program.
8. Start the communication by switching the toggle switch located next to ' Serial Port'. If selected COM port is correct, colored lines will appear on the graph area and Start Line indicator located on the left side will turn green. If selected port is not correct, nothing will appear in the graph area and Serial T/O located exact below the Start Line indicator will turn red.

9. If selected com port is not correct, then turn the Communication Start toggle switch to Off state. Select the different comp port; turn the Start switch to On state.
10. Repeat the steps 8 and 9 till communication starts. Refer the manual if problem persist.
11. Successful communication will indicate "STANDBY" with green back light in the 'State' field located at the left corner of LabView program. 'Failure' field will indicate "NO FAILURE" with green back light and also in the 'Selftest Fault'.
12. Before supplying hydrogen to the fuel cell stack from hydrogen tank, make sure all vales or regulators are in tightly close position. Then turn the 1st regulator to open position as shown in Figure 71. The 1st pressure regulator dial should show pressure upto the range 2000 psi depending upon the amount of hydrogen left in the tank. 2nd dial should show pressure to the range of 30 psi.

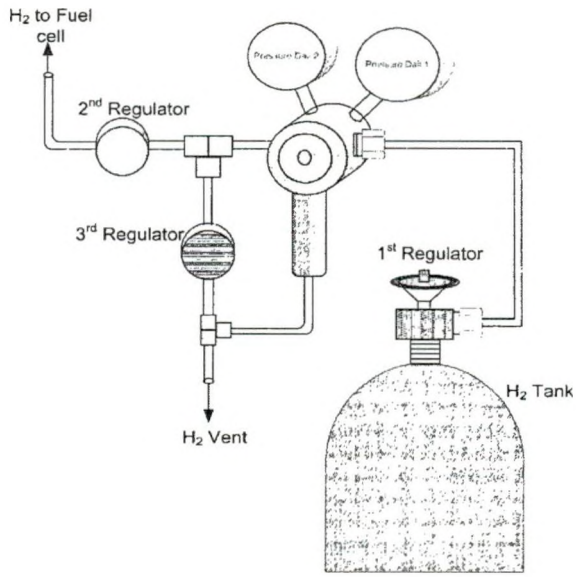

Figure 71: Hydrogen tank-regulator setup for UND's hydrogen fuel cell test facility

13. Open the second valve to supply hydrogen to fuel cell. Do not touch the 3rd valve. 3rd valve should be at tightly closed position.
14. Make sure there is no hydrogen leak every time before you run the experiments using the hand held hydrogen leak detector. This safety procedure is MUST every time before running the fuel cell.
15. Turn "ON" the fuel cell Run switch located near the stack after setting the electronic load.
16. Start up procedure last for 30-40 seconds. When fuel cell starts running, 'State' field in the LabView program says "Running"

While doing EIS tests for fuel cell, electronic load doesn't have to run using the Chroma softpanel. Instead, load is controlled by Zplot using 'External waveform' mode. Refer to Chroma 63200 user manual for details. Chroma 63203 can be operated in two modes, 520W and 5200W. As Nexa™ fuel cell is rated at 1200 W, load has to operate in both modes while performing EIS tests. Low current tests up to 15A can be done in low current setting mode (0-60 A). For higher current tests, load needs to configure for higher current setting mode (0-600 A). Chroma 63203 electronic load set-up steps for EIS tests are as follows:

1. Connect the load to the 1250 FRA using BNC type connector cable. Connect this cable to 'LO' terminal of the FRA Generator located on the back side of FRA and then other end to 'V Ext' terminal located at the back of the electronic load.
2. If current is measured at the load then connect "I Mon" located on back of DC load to one of the analyzer channel of FRA using BNC type cable. Connect to 'LO' terminal of FRA.

3. Put the shorting BNC type plugs to 'HI' terminals of FRA Generator, Channel 1 and Channel 2.
4. Make connections using BNC type cable and alligator or banana type cables to input the measured voltage at the stack to the remaining analyzer channel.
5. Connect the FRA to Comp 2 using GPIB-USB-HS cable.

After connecting the FRA to DC load, follow the following steps to change the DC electronic load settings from front panel to perform EIS tests at low or high currents.

1. Turn the main switch on. LCD displays zero for current, voltage and power.
2. Press 'Sys' and then 'Enter' till you reach 'Ext Wave enable'. Press '1' and then 'Enter' to enable this option. The green LED on front panel for Ext wave will be on. Keep the rest of the settings to default values.
3. Press 'Conf./Local' button to set up the current limits. Select option '1. High' by pressing numerical key '1' and then 'Enter' for "CC, CP, V range".
4. Then select 'Von Point' voltage to anything higher than 0, but lower value (e.g. 1–5 V). This value tells DC load to start drawing the current when the voltage is more than 'Von'.
5. Select option '2.NO' for 'Von Latch Enable'.
6. For low current setting of DC load, enter the 'CV Current Limit' to 60 A and then press 'Enter'.
7. Select option '1. Plus' for 'Sign of Voltage'.
8. Select option '1. Power' for 'Power/Ohm Select'.
9. Select option '1.Value' for 'Spec Entry Mode'

10. Keep all other values to default. Refer to the DC load manual for making any other changes.
11. Press "Range" button on front panel to select the current range. For low current tests upto 15 A. Low current range have to be selected. For higher currents, select high current range.
12. For low current range selection, press "Range" button then keep the values for 'CCHA' and 'CCHB' to 0.00 by entering from numeric pad if required or else press 'Enter'.
13. Select between 'CCLA' and 'CCLB' by pressing "A/B" button located next to "Range".
14. After keeping 'CCHA' and 'CCHB' values to zero. Enter 'CCLA' value to 60 and 'CCLB' to zero.
15. Keep '∫CCL' value to default 0.01 A/ μS.
16. Enter 50 V for 'High' and 1 V for 'Low' under 'CCL Voltage Spec'
17. Keep the rest of options to default settings.
18. For high current range selection, keep 'CCLA' and 'CCLB' to zero and enter 100 A for 'CCHA' and 0 for 'CCHB'. Rest of the settings can be kept same as for low current range setting.

After setting the electronic load to the required load current tests and connecting to FRA, run the FRA using Zplot® software from COMP 1. The following steps should be followed to run the FRA using Zplot.

1. Make sure Zplot software USB key is inserted into COMP 1.
2. Open and run the Zplot program on COMP1.

3. To setup the FRA correctly with the Zplot, go to 'Setup' menu and then select 'Zplot..' submenu from drop down list. Setup Zplot window will appear. Select the 'Solartron 1250/1254(2 Channel)' from the drop down menu under Type. Set the GPIB address to '4'.
4. In the Setup Zplot window, select 'Manual Interface' under 'Pstat/Gstat or Interface' tab from dropdown list. Do not change anything under the Multiplexer tab.
5. Check the GPIB communication by pressing 'Test GPIB' button on Setup Zplot window. If communication is successful, 'Test passed' message will be displayed. Check the GPIB connection and setting in case of test failure.
6. To setup the instrument, go to 'Setup' then 'Instrument' submenu and select the 'Analyzer' tab on Setup Instrument window. Keep the values for 'Range', 'Coupling', 'Input' and 'Outer' to the default. Select the proper channel location for both the channels, generally 'Rear'. Set the integration time to 10 sec.
7. On the Setup Instrument window, select the 'Manual Interface' tab to set the correct Normalization Factor (multiplier). For low current setting of DC electronic load, the normalization factor should be -0.16667 and for high current setting for DC load this factor should be -0.016667.
8. Keep the electrode area to 1 cm^2 under 'Cell' submenu of 'Setup'.
9. With manual interface selected, Zplot does not allow to select 'Ctrl I' tab on main Zplot window. Select the 'Ctrl E: Sweep Freq' tab to set the frequency range. Enter the corresponding DC potential (volts) and AC amplitude (mV) values from experimental design Table 6 for fuel cell. The corresponding potential value in volts of the required DC current should be entered in the DC bias and the required ac signal

amplitude % (e.g. 5%, 7.5%, 10 %) of the DC current (mA) value converted in mV should be entered for the ac amplitude in Zplot.

10. Finally, sweep the frequency using 'Sweep' function under 'Measure' menu tab.

Table 6: DC potential and AC amplitude signal values for fuel cell EIS tests

A	V	mA	mV	mA	mV	mA	mV	mA	mV
DC	Vdc	5%	Vac	7.50%	Vac	10%	Vac	15%	Vac
0.5	0.08333	25	4.1665	37.5	6.2498	50	8.333	75	12.4995
1	0.16666	50	8.333	75	12.5	100	16.666	150	24.999
1.5	0.24999	75	12.4995	112.5	18.749	150	24.999	225	37.4985
2	0.33332	100	16.666	150	24.999	200	33.332	300	49.998
2.5	0.41665	125	20.8325	187.5	31.249	250	41.665	375	62.4975
3	0.49998	150	24.999	225	37.499	300	49.998	450	74.997
4	0.66664	200	33.332	300	49.998	400	66.664	600	99.996
5	0.8333	250	41.665	375	62.498	500	83.33	750	124.995
6	0.99996	300	49.998	450	74.997	600	99.996	900	149.994
7	1.16662	350	58.331	525	87.497	700	116.662	1050	174.993
8	1.33328	400	66.664	600	99.996	800	133.328	1200	199.992
9	1.49994	450	74.997	675	112.5	900	149.994	1350	224.991
10	1.6666	500	83.33	750	125	1000	166.66	1500	249.99
12	1.99992	600	99.996	900	149.99	1200	199.992	1800	299.988
15	2.4999	750	124.995	1125	187.49	1500	249.99	2250	374.985
18	2.99988	900	149.994	1350	224.99	1800	299.988	2700	449.982
20	3.3332	1000	166.66	1500	249.99	2000	333.32	3000	499.98
25	4.1665	1250	208.325	1875	312.49	2500	416.65	3750	624.975
30	4.9998	1500	249.99	2250	374.99	3000	499.98	4500	749.97
35	5.8331	1750	291.655	2625	437.48	3500	583.31	5250	874.965
40	6.6664	2000	333.32	3000	499.98	4000	666.64	6000	999.96

APPENDIX B

Operating Procedure for Electrolyzer EIS Tests

The operating procedure for EIS study of 6 kW PEM electrolyzer is divided in three setups namely: Low frequency setup, Middle frequency setup, and High frequency setup. The operating procedure to run the electrolyzer is detailed by Harrison [6]. All the steps in the operating procedure to run the electrolyzer system should be followed except the supplying power to the electrolyzer. For EIS tests the DC power supplies are not controlled using the LabView program for the electrolyzer system. However, to run the electrolyzer system properly and for safe shut down of the system, the current and voltage should be entered in the respective fields under the 'PS & Data Acq' tab of the LabView program. The 'PS Output Control' switch should be turned to 'ON' position before starting EIS experiment. Failure to do so can cause improper operation and solenoid valves for water control and desiccant dryer won't be functioning properly.

The electrolyzer system is run using COMP 2, while FRA is run through Zplot using COMP 1.

Operating Procedure for Low Frequency Setup

The Xantrex DC power supply named as 'PS 1' has been modified to perform the low frequency EIS tests of the 6 kW PEM electrolyzer as discussed earlier in Chapter 3. Only PS 1 should be connected to the electrolyzer .Following steps should be performed to carry out the low frequency EIS tests:

1. Connect the DC power supply, PS 1 to the FRA Generator using BNC connector cable at one end and striped wires at the other end.
2. Insert the striped wire ends into the B1 and B4 terminal of the programming line inputs at the back of the PS 1.

3. Connect a shunt resistor (specification: 100 A, 50mV) in series with electrolyzer using the 1 AWG main cable connected to the positive terminal of the PS 1.
4. Make the connections to measure the voltage across the shunt resistor and to input to the Channel 1 of the FRA (either at the front or back)
5. Electrolyzer stack voltage can be measured directly across the stack by connecting the measurement cable to the positive and negative terminal of the stack.
6. Input this measured stack voltage to the Channel 2 of the FRA (either front or back)
7. Turn the power supply PS 1 on. Enter the 'Menu' to select the analog input range to 0-10 V and 'Analog I' to control the current. Voltage will be controlled from the front panel. Put the PS 1 in remote mode by using LCL/RMT switch from the front panel. Refer the Xantrex Power supply manual for details.
8. Press the 'Out On' switch to supply the power to the electrolyzer only when the electrolyzer system is running and ready for the EIS tests.
9. Turn on the FRA.
10. Enter the required value for the DC offset in V and AC signal amplitude in mV summarized in following table in the respective fields of the Zplot program.
11. If electrolyzer system is ready, press the 'Out On' switch on the PS 1.
12. Start sweeping the frequency between 20 Hz to 0.5 Hz using the Zplot software.

A	V	mA	mV	mA	mV	mA	mV	mA	mV	mA	mV	mA	mV	mA	mV
DC	Vdc	1%	Vac	2%	Vac	3%	Vac	5%	Vac	7.50%	Vac	10%	Vac	15%	Vac
1	0.1	10	1	20	2	25	2.5	50	5	75	7.5	100	10	150	15
2	0.2	20	2	40	4	50	5	100	10	150	15	200	20	300	30
3	0.3	30	3	60	6	75	7.5	150	15	225	22.5	300	30	450	45
4	0.4	40	4	80	8	100	10	200	20	300	30	400	40	600	60
5	0.5	50	5	100	10	125	12.5	250	25	375	37.5	500	50	750	75
6	0.6	60	6	120	12	150	15	300	30	450	45	600	60	900	90
7	0.7	70	7	140	14	175	17.5	350	35	525	52.5	700	70	1050	105
8	0.8	80	8	160	16	200	20	400	40	600	60	800	80	1200	120
9	0.9	90	9	180	18	225	22.5	450	45	675	67.5	900	90	1350	135
10	1	100	10	200	20	250	25	500	50	750	75	1000	100	1500	150
12	1.2	120	12	240	24	300	30	600	60	900	90	1200	120	1800	180
15	1.5	150	15	300	30	375	37.5	750	75	1125	112.5	1500	150	2250	225
20	2	200	20	400	40	500	50	1000	100	1500	150	2000	200	3000	300
25	2.5	250	25	500	50	625	62.5	1250	125	1875	187.5	2500	250	3750	375
30	3	300	30	600	60	750	75	1500	150	2250	225	3000	300	4500	450
35	3.5	350	35	700	70	875	87.5	1750	175	2625	262.5	3500	350	5250	525
40	4	400	40	800	80	1000	100	2000	200	3000	300	4000	400	6000	600
45	4.5	450	45	900	90	1125	112.5	2250	225	3375	337.5	4500	450	6750	675
50	5	500	50	1000	100	1250	125	2500	250	3750	375	5000	500	7500	750
55	5.5	550	55	1100	110	1375	137.5	2750	275	4125	412.5	5500	550	8250	825
60	6	600	60	1200	120	1500	150	3000	300	4500	450	6000	600	9000	900
65	6.5	650	65	1300	130	1625	162.5	3250	325	4875	487.5	6500	650	9750	975
70	7	700	70	1400	140	1750	175	3500	350	5250	525	7000	700	10500	1050
75	7.5	750	75	1500	150	1875	187.5	3750	375	5625	562.5	7500	750	11250	1125
80	8	800	80	1600	160	2000	200	4000	400	6000	600	8000	800	12000	1200
85	8.5	850	85	1700	170	2125	212.5	4250	425	6375	637.5	8500	850	12750	1275

Operating Procedure for High Frequency Setup

To obtain the high frequency (20 kHz--1 kHz) EIS data, both the Xantrex power supplies needed. One power source supplies power to the electrolyzer stack while the other supplies power to the amplifier. Following procedure should be followed to obtain the high frequency EIS data.

1. Make the connections as shown in Figure 9 and Figure 10. Connect the primary side of the transformer core wire to the either left (L) or right (R) speaker output of the amplifier.
2. Secondary side of the core has only one turn of the wire. Connect the one end of the secondary side wire to the +ve terminal of the PS1 and other side to the +ve terminal of the electrolyzer stack.
3. The +ve and –ve output terminals of the PS2 should be connected to the GND and BATT input terminals of the amplifier.
4. A linear power supply is also needed to connect to the amplifier. The positive and negative terminals of the linear power supply are connected to the GND and REM of the amplifier respectively.
5. The amplifier amplifies the AC signal with DC offset generated by the FRA. Therefore connect the FRA generator output to the amplifier's one of the input channel, either left (L) or right (R).
6. Precaution should be taken while supplying power from the PS2 to the amplifier than voltage should not exceed 12 V. As the current level supplied to the electrolyzer increases, the amplifier draws more current.

7. To obtain the high frequency data, the AC signal on the primary side of the transformer core should be large enough to cause the required perturbation on the DC current of the secondary side. The perturbations of the DC current supplied top the electrolyzer can be accurately measured by current transducer. The current data can be collected with the LabView program data logging. The value of the AC signal that need to be enter into the FRA program varies with the current and AC signal amplitude of the required % of the DC. To get the AC amplitude signal of 10 % of the DC, the approximate ratio of the FRA AC signal and desired AC signal amplitude required is 0.00155. For example, at 10 Adc current, the 10% AC signal amplitude would be 1 A. To cause the 1A ac perturbation of 10 Adc, the value of the FRA AC signal need to be 645.16 mV (i.e. 1/0.00155). These signals then get amplified by the amplifier to get the required test signal for the EIS test.

APPENDIX C

Operating Procedure for Dew Point Control System

Dew point control system should be hooked up with the electrolyzer system, data acquisition system and the TEC enclosure using the following steps.

1. The output of the high pressure hydrogen-water separator should be connected to the input of the first stage CPA1 using the flexible SS cable. In electrolyzer system this output is connected to the coalescing filter and then to the two tube desiccant dryer.
2. The output of the dew point system (i.e. after the dew point sensor, DP) should be connected to the back pressure regulator.
3. Make sure the valve on the bypass line for the dew point sensor (DP1) of the electrolyzer system is completely closed.
4. All the CPAs are water cooled. Connect the pump input water line to the oxygen-water phase separator tank.
5. The outputs of all water cooling blocks are connected together. This water is again input to the oxygen-water phase separator using polypropylene tubing.
6. After turning the pump on using the LabView user interface, make sure that the water is flowing through all the waterblocks and there are no air bubbles.
7. The condensed water from the cold plate is collected in the Bekomat after each CPA using the coalescing filter. This condensed water is drained to the external water reservoir at the bottom.
8. Connect the Cable 10 and Cable 11 from the dew point system to the TEC enclosure inputs 10S and 11S respectively.
9. The TEC enclosure is connected to the data acquisition system using Cable 12. Connect the Cable 12 from data acquisition to the 12P input of the TEC enclosure.

10. Connect all the dew point system sensors to the respective cables with the help of Table 7 descriptions.

Table 7: Dew point system's sensor wiring connections description

Sensor Name	Cable to Connect	Description	Data Acquisition Channel
Pressure, P0	Cbl 18DS	Connect Red to Red & Black to Black Red = 24 V Black = Analog input Signal	AnalogIN 21
Pressure, Pi	Cbl 18AD	Connect Red to Red & Black to Black Red = 24 V Black = Analog input Signal	AnalogIN 12
Temp., T5	Cbl 9D	Connect Red to +ve and Black to –ve Red = 24 V Black = Analog input Signal	AnalogIN 16
Temp., T6	Cbl 9C	Connect Red to +ve and Black to –ve Red = 24 V Black = Analog input Signal	AnalogIN 14
Dew point sensor, DP	Cbl 31	Refer wiring diagram from DP manual Red = 24 V Black = Analog input Signal Shield = Ground	AnalogIN 29
All Bekomats	Cbl 30	Big thick cable from rack mounting plate with 24 V supply	None

The TEC based dew point system is controlled and monitored using the LabView program shown in Figure 72.Follow the procedure for running the electrolyzer system summarized by Harrison [6]. Few of the steps of the electrolyzer system required for the dew point system are summarized below;

1. Start the LabView program by pressing the ⇒ tab. The comment window will popup followed by data saving window. Save the data to the specific folder if required.
2. Go to the 'Cold Plate' tab of the LabView program which is shown in Figure 72. If program is running, all the names of digital output (DO) channels name would appear in the 'DO Ch Names' window.
3. Make sure the program is communicating with the system by activating the switches provided on the front panel. Activating the switch 'Cooling Pump' would start the cooling pump and start circulating water through all the cooling water blocks.
4. Press the 'Start' switch to start the dew point system. This will activate all the TECs and cooling pump. All the sensors would show the respective reading of the parameters.
5. Run the electrolyzer by inputting some power to the electrolyzer.
6. Hydrogen generated by the electrolyzer would start flowing through these CPAs. If first stage TEC is getting too cold then it can be stopped by activating 'TEC1 OFF' switch. There is possibility of ice formation in the second stage CPAs. If the pressure difference between stage 1 & 2 reaches greater than 5 psi, switch the hydrogen flow to the parallel branch using solenoid valve switch 'SV'.

7. Simultaneously, reverse the polarity of the respective TEC to melt the ice. For example, at the beginning the hydrogen flows through CPA 2b, so reverse the polarity of TEC 2b and divert hydrogen flow to the CPA 2a.
8. Repeat the steps 6 and 7 if the pressure difference reaches 5 psi to divert the hydrogen flow to the parallel branch.

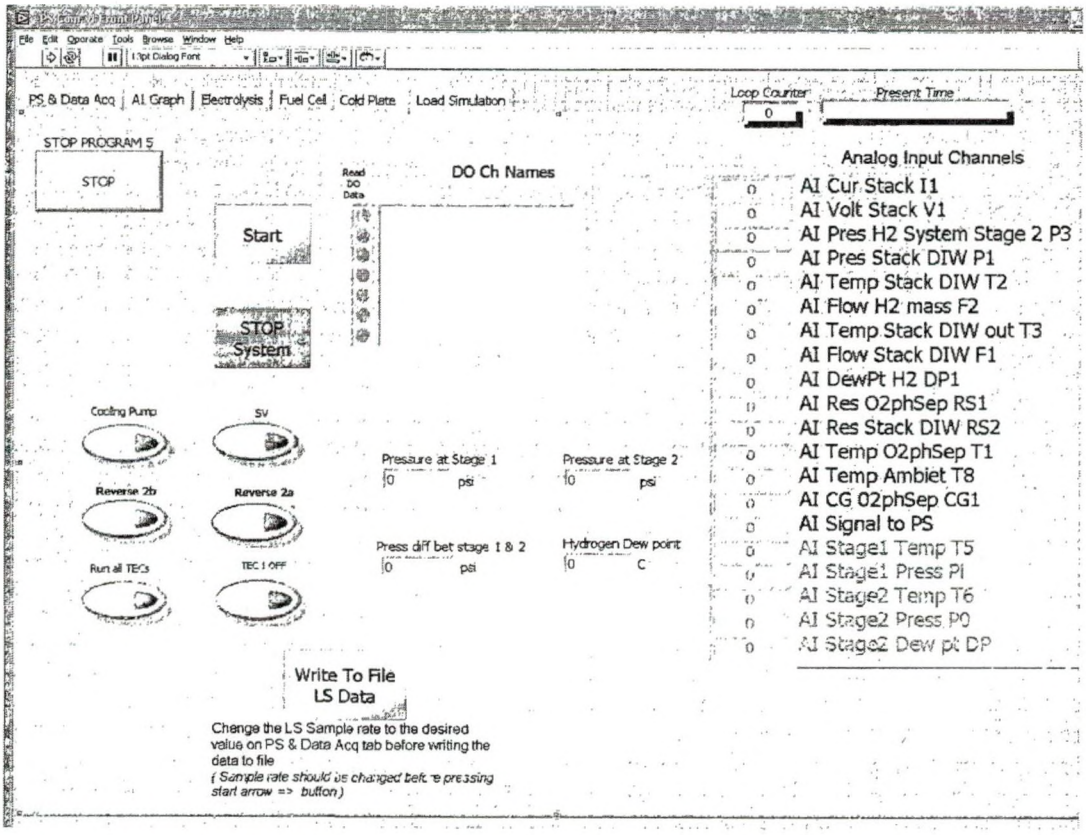

Figure 72: Front panel of LabView program for dew point control set up

The details of the wiring diagram for the TEC enclosure, Cable 10, 11, 12 are shown in the following pages.

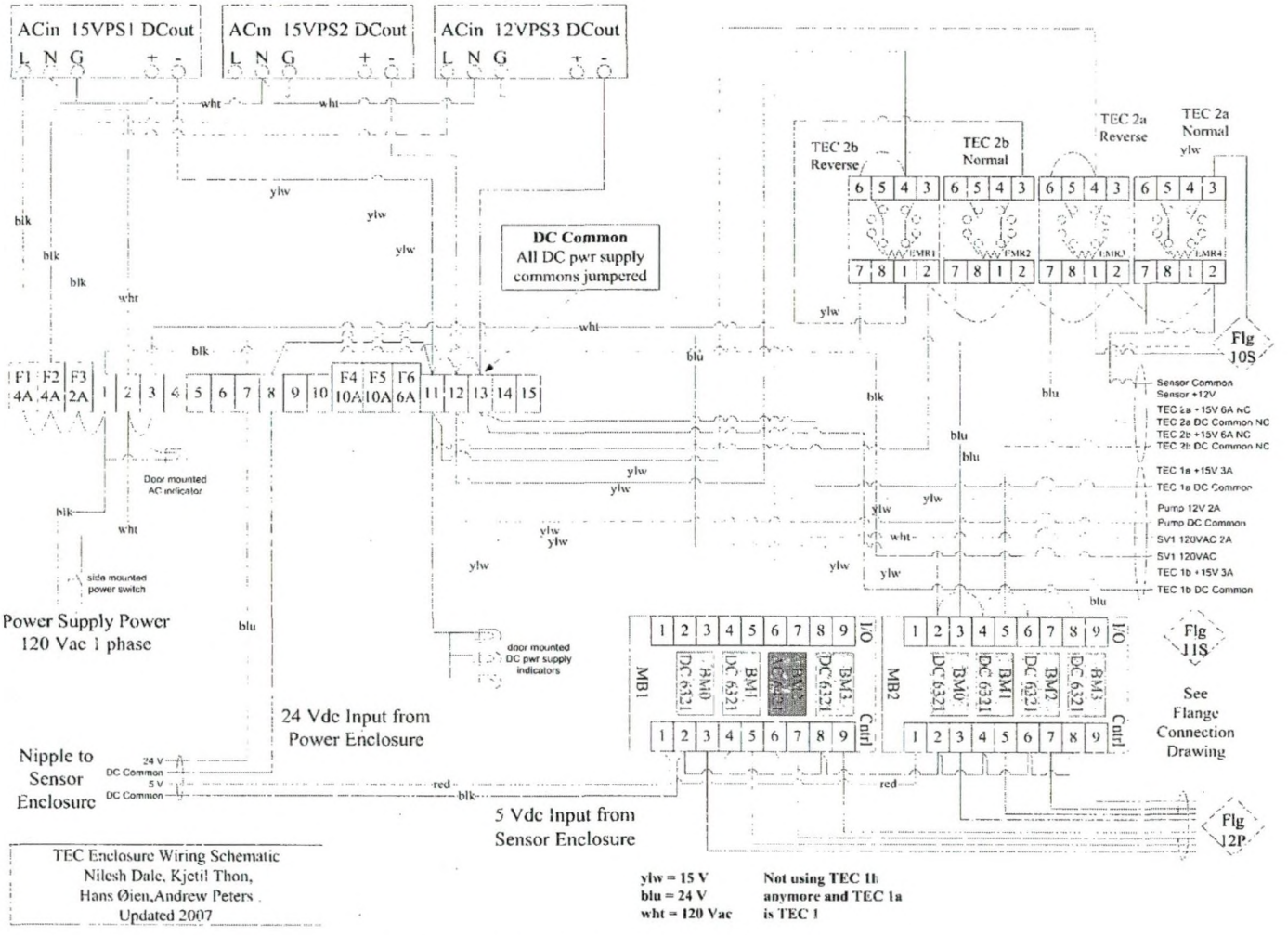

Figure 73: TEC enclosure wiring diagram

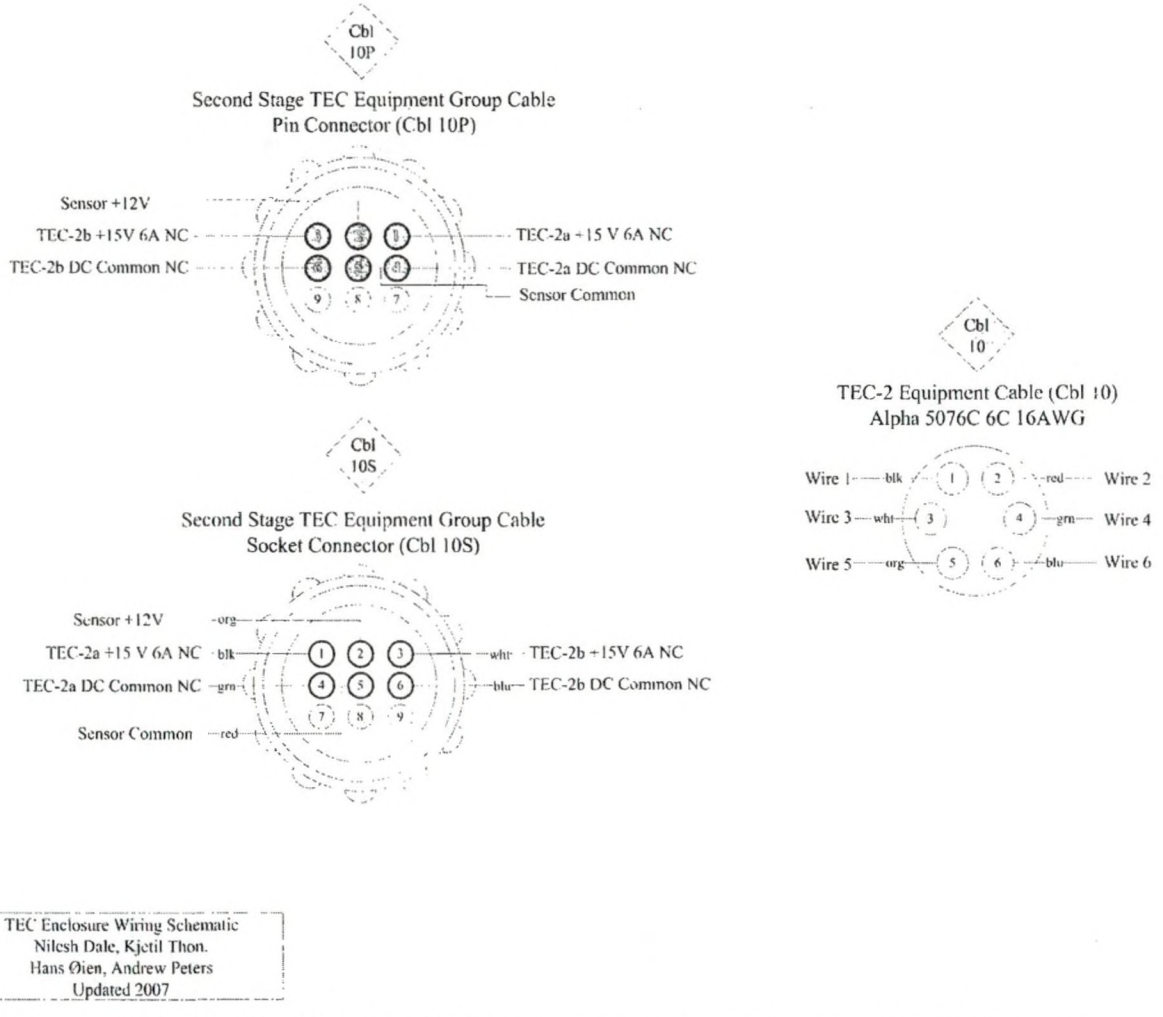

Figure 74: Cable 10 wiring from TEC enclosure to the second stage of the TEC system.

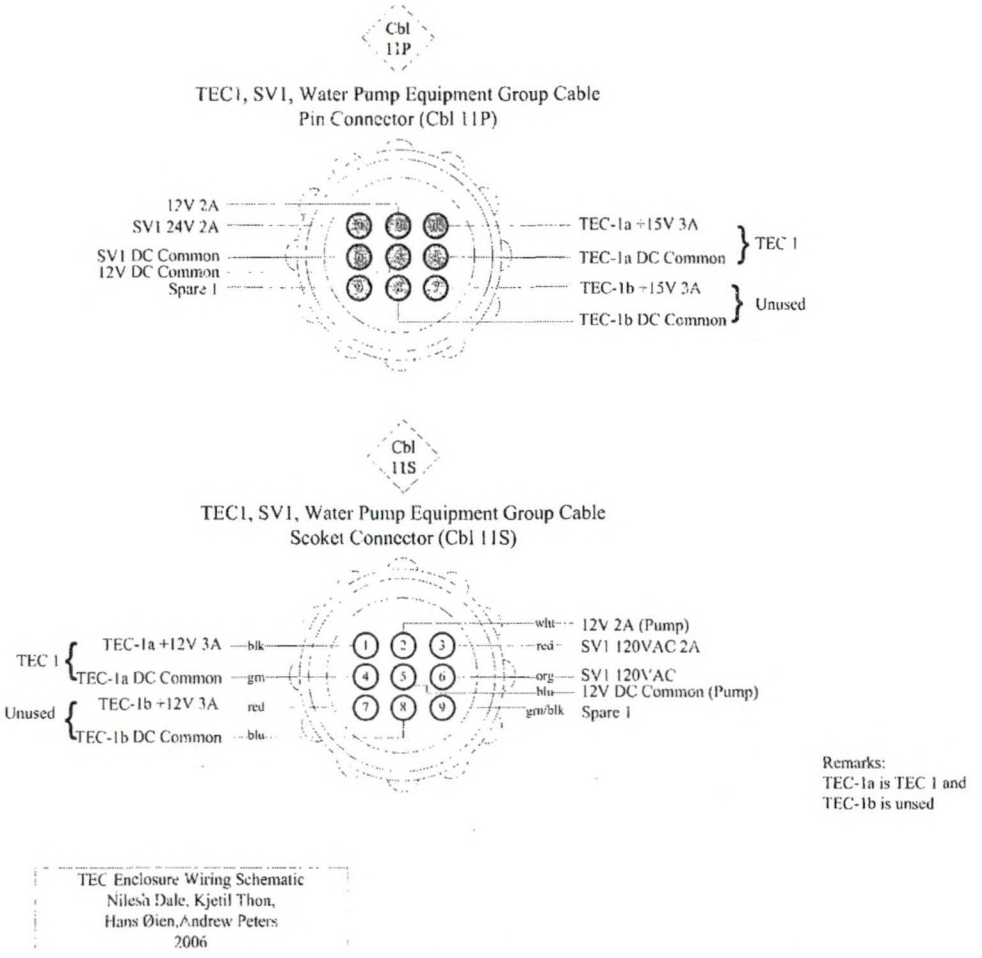

Figure 75: Cable 11 wiring from TEC enclosure to the first stage system, pump and solenoid valve.

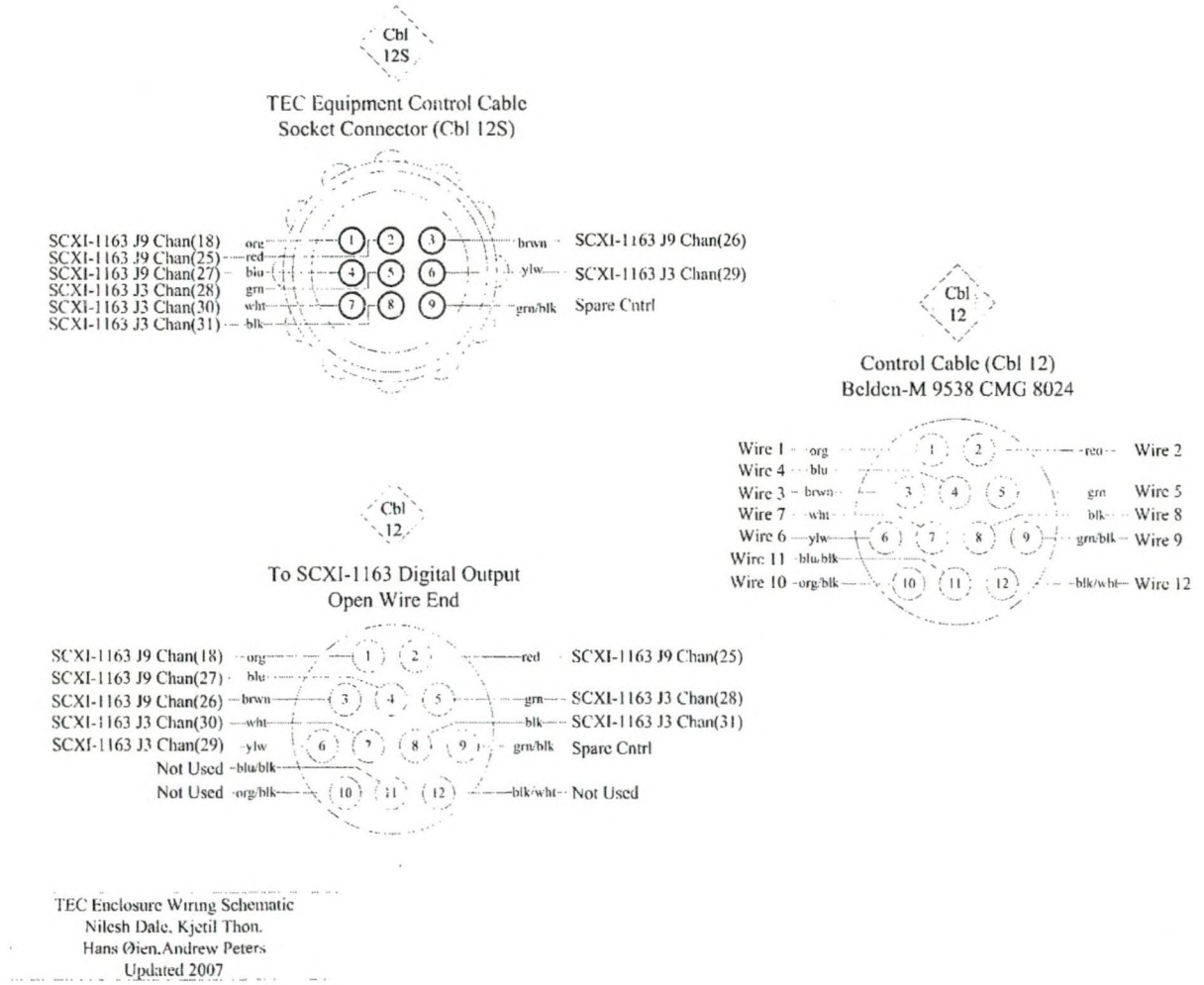

Figure 76: Cable 12 wiring diagram for digital output (DO) from SCXI 1163 to the TEC enclosure.

APPENDIX D

6 kW PEM Electrolyzers Semiempirical Model Code

The Mathematica program code for the semiempirical model of the PEM electrolyzer is presented here. The bold lines are the input commands and the remaining are the outputs. The resulting plots are not shown in the code. This code is for the Mathematica version 5.2. Higher version of Mathematica is not compatible with a few of these commands; however some get replaced with similar newer version commands.

file1 ="C:\Documents and Settings\Guest\My Documents\Data\10CtestLS.csv"
C:\Documents and Settings\Guest\My Documents\Data\10CtestLS.csv

expIVdata1=Import[file1];
a=.;b=.;c=.
F=96485; R=8.314; NC=20;
A= 0.093 12.0^2 2.54^2
86.3998

<<Graphics`MultipleListPlot`
<<Statistics`NonlinearFit`
<<Statistics`NormalDistribution`

T1=10+273.15
283.15

Vn1 = 1.393329505
1.39333

$$\text{Ecell} = \text{Vn1} + \left(\frac{\text{RT1}}{2*0.15\,\text{F}}\right)\text{ArcSinh}\left[\frac{\frac{x}{A}}{2a}\right] + \left(\frac{\text{RT1}}{2*0.5\,\text{F}}\right)\text{ArcSinh}\left[\frac{\frac{x}{A}}{2b}\right] + \left(\frac{178.0*10^{-4}}{c}\right)\frac{x}{A}$$

fit1=FindFit[expIVdata1, NC Ecell, {{a,0.1},{b,0.000009},{c,0.001}},x,MaxIterations→ 100]
{a→ 0.181968,b→ 0.0000430306,c→ 0.0584521}

fita1=NonlinearRegress[expIVdata1,NC Ecell, x,{{a,0.1},{b,0.0000009},{c,0.01}}]
g=Ecell 20/.fit1
20 (1.39333 +0.00352458 x+0.081329 ArcSinh[0.0318025 x]+0.0243987 ArcSinh[134.487 x])

gp=Plot[g,{x,10,140},Frame→ True,PlotRange→ All,TextStyle→ {FontSize→ 14},
FrameLabel→ {StyleForm["Current A "], StyleForm["Stack Voltage V"]},AxesOrigin->{0,28},
PlotStyle→ {Hue[1,1,0],Thickness[0.006]}, ImageSize→ 500]

file2 ="C:\Documents and Settings\Guest\My Documents\Data\15Ctest.csv"
C:\Documents and Settings\Guest\My Documents\Data\15Ctest.csv

expIVdata2=Import[file2];
T2=15+273.15
288.15

Vn2=1.387816249
1.38782

$$\text{Ecell2} = \text{Vn2} + \left(\frac{\text{RT2}}{2*0.17\,\text{F}}\right)\text{ArcSinh}\left[\frac{\frac{x}{A}}{2a}\right] + \left(\frac{\text{RT2}}{2*0.5\,\text{F}}\right)\text{ArcSinh}\left[\frac{\frac{x}{A}}{2b}\right] + \left(\frac{178.0*10^{-4}}{c}\right)\frac{x}{A}$$

fit2=FindFit[expIVdata2, NC Ecell2, {{a,0.1},{b,0.000009},{c,0.001}},x,MaxIterations→ 100]
{a→ 0.148793,b→ 0.000062729,c→ 0.0600136}

fita2=NonlinearRegress[expIVdata2,NC Ecell2,x,{{a,0.1},{b,0.0000009},{c,0.01}}]
g1=Ecell2 20/.fit2
20 (1.38782 +0.00343287 x+0.0730281 ArcSinh[0.0388932 x]+0.0248295 ArcSinh[92.2548 x])

gp1=Plot[g1,{x,10,140},Frame→ True, PlotRange→ All,TextStyle→ {FontSize→ 14},
FrameLabel→ {StyleForm["Current A "],StyleForm["Stack Voltage V"]},AxesOrigin->{0,28},
PlotStyle→ {Hue[1,1,0],Thickness[0.006]}, ImageSize→ 500]

file3 ="C:\Documents and Settings\Guest\My Documents\Data\20CtestLS.csv"
C:\Documents and Settings\Guest\My Documents\Data\20CtestLS.csv

expIVdata3=Import[file3];
T3=20+273.15
293.15

Vn3=1.382347654

$$\text{Ecell3} = \text{Vn3} + \left(\frac{\text{RT3}}{2*0.18\,\text{F}}\right)\text{ArcSinh}\left[\frac{\frac{x}{A}}{2a}\right] + \left(\frac{\text{RT3}}{2*0.5\,\text{F}}\right)\text{ArcSinh}\left[\frac{\frac{x}{A}}{2b}\right] + \left(\frac{178.0*10^{-4}}{c}\right)\frac{x}{A}$$

fit3=FindFit[expIVdata3, NC Ecell3, {{a,0.1},{b,0.000009},{c,0.001}},x,MaxIterations→ 100]
{a→ 0.278931,b→ 0.0000820881,c→ 0.0638291}

fita3=NonlinearRegress[expIVdata3,NC Ecell3,x,{{a,0.1},{b,0.0000009},{c,0.01}}]
g2=Ecell3 20/.fit3
20 (1.38235 +0.00322766 x+0.0701678 ArcSinh[0.0207473 x]+0.0252604 ArcSinh[70.4981 x])

gp2=Plot[g2,{x,10,140},Frame→ True,PlotRange→ All,TextStyle→ {FontSize→ 14},
FrameLabel→ {StyleForm["Current A "],StyleForm["Stack Voltage V"]},AxesOrigin->{0,28},
PlotStyle→ {Hue[1,1,0],Thickness[0.006]}, ImageSize→ 500]

file4 ="C:\Documents and Settings\Guest\My Documents\Data\25CtestLS.csv"
C:\Documents and Settings\Guest\My Documents\Data\25CtestLS.csv

expIVdata4=Import[file4];
T4=25+273.15
298.15

Vn4=1.376928493
1.37693

$$\text{Ecell4} = \text{Vn4} + \left(\frac{\text{RT3}}{2*0.257\,\text{F}}\right)\text{ArcSinh}\left[\frac{\frac{x}{A}}{2a}\right] + \left(\frac{\text{RT3}}{2*0.5\,\text{F}}\right)\text{ArcSinh}\left[\frac{\frac{x}{A}}{2b}\right] + \left(\frac{178.0*10^{-4}}{c}\right)\frac{x}{A}$$

fit4=FindFit[expIVdata4, NC Ecell4, {{a,0.1},{b,0.000009},{c,0.001}},x,MaxIterations→ 100]
{a→ 0.216603,b→ 0.000166491,c→ 0.0653547}

fita4=NonlinearRegress[expIVdata4,NC Ecell4,x,{{a,0.1},{b,0.0000009},{c,0.01}}]
g3=Ecell4 20/.fit4
20 (1.37693 +0.00315232 x+0.049983 ArcSinh[0.0267173 x]+0.0256912 ArcSinh[34.759 x])

gp3=Plot[g3,{x,10,140},Frame→ True, PlotRange→ All, TextStyle→ {FontSize→ 14},
FrameLabel→ {StyleForm["Current A "], StyleForm["Stack Voltage V"]}, AxesOrigin->{0,28},
PlotStyle→ {Hue[1,1,0],Thickness[0.006]}, ImageSize→ 500]

file5 ="C:\Documents and Settings\Guest\My Documents\Data\30CtestLS.csv"
C:\Documents and Settings\Guest\My Documents\Data\30CtestLS.csv

expIVdata5=Import[file5];
T5=30+273.15
303.15

Vn5=1.371552921
1.37155

$$\text{Ecell5} = \text{Vn5} + \left(\frac{\text{RT5}}{2*0.217\,\text{F}}\right)\text{ArcSinh}\left[\frac{\frac{x}{A}}{2a}\right] + \left(\frac{\text{RT5}}{2*0.5\,\text{F}}\right)\text{ArcSinh}\left[\frac{\frac{x}{A}}{2b}\right] + \left(\frac{178.0*10^{-4}}{c}\right)\frac{x}{A}$$

fit5=FindFit[expIVdata5, NC Ecell5, {{a,0.1},{b,0.000009},{c,0.001}},x,MaxIterations→ 100]
{a→ 0.321392,b→ 0.000113939,c→ 0.0735107}

fita5=NonlinearRegress[expIVdata5,NC Ecell5,x,{{a,0.1},{b,0.0000009},{c,0.01}}]
g4=Ecell5 20/.fit5
20 (1.37155 +0.00280257 x+0.0601891 ArcSinh[0.0180062 x]+0.0261221 ArcSinh[50.7908 x])

gp4=Plot[g4,{x,10,140},Frame→ True,PlotRange→ All,TextStyle→ {FontSize→ 14},
FrameLabel→ {StyleForm["Current A "],StyleForm["Stack Voltage V"]},AxesOrigin->{0,28},
PlotStyle→ {Hue[1,1,0],Thickness[0.006]}, ImageSize→ 500]

file6 ="C:\Documents and Settings\Guest\My Documents\Data\34CtestLS.csv"
C:\Documents and Settings\Guest\My Documents\Data\34CtestLS.csv

expIVdata6=Import[file6];
T6=35+273.15
308.15

Vn6=1.366122172
1.36612

$$Ecell6 = Vn6 + \left(\frac{RT6}{2*0.35\,F}\right)\text{ArcSinh}\left[\frac{\frac{x}{A}}{2a}\right] + \left(\frac{RT6}{2*0.5\,F}\right)\text{ArcSinh}\left[\frac{\frac{x}{A}}{2b}\right] + \left(\frac{178.0*10^{-4}}{c}\right)\frac{x}{A}$$

fit6=FindFit[expIVdata6, NC Ecell6, {{a,0.1},{b,0.000009},{c,0.001}},x,MaxIterations→ 100]
{a→ 0.233164,b→ 0.000132684,c→ 0.0736473}

fita6=NonlinearRegress[expIVdata6,NC Ecell6,x,{{a,0.1},{b,0.0000009},{c,0.01}}]
g5=Ecell6 20/.fit6
20 (1.36612 +0.00279737 x+0.0379328 ArcSinh[0.0248196 x]+0.0265529 ArcSinh[43.6154 x])

gp5=Plot[g5,{x,10,140},Frame→ True, PlotRange→ All, TextStyle→ {FontSize→ 14},
FrameLabel→ {StyleForm["Stack Current A "],StyleForm["Stack Voltage V"]},AxesOrigin->{0,28}, PlotStyle→ {Hue[1,1,0],Thickness[0.006]}, ImageSize→ 500]

file7 ="C:\Documents and Settings\Guest\My Documents\Data\40CtestIV.csv"
C:\Documents and Settings\Guest\My Documents\Data\40CtestIV.csv

expIVdata7=Import[file7];
T7=40+273.15
313.15

Vn7=1.360926166
1.36093

$$Ecell7 = Vn7 + \left(\frac{RT7}{2*0.30\,F}\right)\text{ArcSinh}\left[\frac{\frac{x}{A}}{2a}\right] + \left(\frac{RT7}{2*0.5\,F}\right)\text{ArcSinh}\left[\frac{\frac{x}{A}}{2b}\right] + \left(\frac{178.0*10^{-4}}{c}\right)\frac{x}{A}$$

fit7=FindFit[expIVdata7, NC Ecell7, {{a,0.1},{b,0.000009},{c,0.001}},x,MaxIterations→ 100]
{a→ 0.261542,b→ 0.000189162,c→ 0.0853588}

fita7=NonlinearRegress[expIVdata7,NC Ecell7,x,{{a,0.1},{b,0.0000009},{c,0.01}}]
g6=Ecell7 20/.fit7
20 (1.36093 +0.00241357 x+0.044973 ArcSinh[0.0221267 x]+0.0269838 ArcSinh[30.593 x])

gp6=Plot[g6,{x,10,140},Frame→ True,PlotRange→ All,TextStyle→ {FontSize→ 14},
FrameLabel→ {StyleForm["Stack Current A "],StyleForm["Stack Voltage V"]},AxesOrigin->{0,28}, PlotStyle→ {Hue[1,1,0],Thickness[0.006]}, ImageSize→ 500]

file8 ="C:\Documents and Settings\Guest\My Documents\Data\45CtestIV.csv"
C:\Documents and Settings\Guest\My Documents\Data\45CtestIV.csv

expIVdata8=Import[file8];
T8=45+273.15
318.15

Vn8=1.355675668
1.35568

$$Ecell8 = Vn8 + \left(\frac{RT8}{2*0.37\,F}\right)\text{ArcSinh}\left[\frac{\frac{x}{A}}{2a}\right] + \left(\frac{RT8}{2*0.5\,F}\right)\text{ArcSinh}\left[\frac{\frac{x}{A}}{2b}\right] + \left(\frac{178.0*10^{-4}}{c}\right)\frac{x}{A}$$

fit8=FindFit[expIVdata8, NC Ecell8, {{a,0.1},{b,0.000009},{c,0.001}},x,MaxIterations→ 100]
{a→ 0.248972,b→ 0.000223952,c→ 0.0870584}

fita8=NonlinearRegress[expIVdata8,NC Ecell8,x,{{a,0.1},{b,0.0000009},{c,0.01}}]
g7=Ecell8 20/.fit8
20 (1.35568 +0.00236644 x+0.0370468 ArcSinh[0.0232437 x]+0.0274146 ArcSinh[25.8405 x])

gp7=Plot[g7,{x,10,140},Frame→ True, PlotRange→ All, TextStyle→ {FontSize→ 14},
FrameLabel→ {StyleForm["Stack Current A "],StyleForm["Stack Voltage V"]},AxesOrigin->{0,28}, PlotStyle→ {Hue[1,1,0],Thickness[0.006]}, ImageSize→ 500]

file9 ="C:\Documents and Settings\Guest\My Documents\Data\50CtestIV.csv"
C:\Documents and Settings\Guest\My Documents\Data\50CtestIV.csv

expIVdata9=Import[file9];
T9=50+273.15
323.15

Vn9=1.35045934
1.35046

$$Ecell9 = Vn9 + \left(\frac{RT9}{2*0.395\,F}\right)\text{ArcSinh}\left[\frac{\frac{x}{A}}{2a}\right] + \left(\frac{RT9}{2*0.5\,F}\right)\text{ArcSinh}\left[\frac{\frac{x}{A}}{2b}\right] + \left(\frac{178.0*10^{-4}}{c}\right)\frac{x}{A}$$

fit9=FindFit[expIVdata9, NC Ecell9, {{a,0.1},{b,0.000009},{c,0.001}},x,MaxIterations→ 100]
{a→ 0.247867,b→ 0.000245622,c→ 0.0927394}

fita9=NonlinearRegress[expIVdata9,NC Ecell9,x,{{a,0.1},{b,0.0000009},{c,0.01}}]
g8=Ecell9 20/.fit9
20 (1.35046 +0.00222148 x+0.0352474 ArcSinh[0.0233474 x]+0.0278455 ArcSinh[23.5608 x])

gp8=Plot[g8,{x,10,140}, Frame→ True, PlotRange→ All, TextStyle→ {FontSize→ 14},
FrameLabel→ {StyleForm["Stack Current A "],StyleForm["Stack Voltage V"]}, AxesOrigin->{0,28}, PlotStyle→ {Hue[1,1,0],Thickness[0.006]}, ImageSize→ 500]

file10 ="C:\Documents and Settings\Guest\My Documents\Data\55CtestIV.csv"
C:\Documents and Settings\Guest\My Documents\Data\55CtestIV.csv

expIVdata10=Import[file10];
T10=55+273.15
328.15

Vn10=1.345292736
1.34529

$$Ecell10 = Vn10 + \left(\frac{RT10}{2*0.391F}\right)\text{ArcSinh}\left[\frac{\frac{x}{A}}{2a}\right] + \left(\frac{RT10}{2*0.5F}\right)\text{ArcSinh}\left[\frac{\frac{x}{A}}{2b}\right] + \left(\frac{178.0*10^{-4}}{c}\right)\frac{x}{A}$$

fit10=FindFit[expIVdata10, NC Ecell10, {{a,0.1},{b,0.000009},{c,0.001}},x,MaxIterations→ 100]
{a→ 0.320745, b→ 0.000283085,c→ 0.0939453}

fita10=NonlinearRegress[expIVdata10,NC Ecell10,x,{{a,0.1},{b,0.0000009},{c,0.01}}]
g9=Ecell10 20/.fit10
20 (1.34529 +0.00219297 x+0.036159 ArcSinh[0.0180425 x]+0.0282763 ArcSinh[20.4428 x])

gp9=Plot[g9,{x,10,140},Frame→ True,PlotRange→ All,TextStyle→ {FontSize→ 14},
FrameLabel→ {StyleForm["Stack Current A "],StyleForm["Stack Voltage V"]},AxesOrigin->{0,28}, PlotStyle→ {Hue[1,1,0],Thickness[0.006]}, ImageSize→ 500]

file11 ="C:\Documents and Settings\Guest\My Documents\Data\60CtestIV.csv"
C:\\Documents and Settings\\Guest\\My Documents\\Data\\60CtestIV.csv

expIVdata11=Import[file11];
T11=60+273.15
333.15

Vn11=1.340155254
1.34016

$$Ecell11 = Vn11 + \left(\frac{RT11}{2*0.43F}\right)\text{ArcSinh}\left[\frac{\frac{x}{A}}{2a}\right] + \left(\frac{RT11}{2*0.5F}\right)\text{ArcSinh}\left[\frac{\frac{x}{A}}{2b}\right] + \left(\frac{178.0*10^{-4}}{c}\right)\frac{x}{A}$$

fit11=FindFit[expIVdata11, NC Ecell11, {{a,0.1},{b,0.000009},{c,0.001}},x,MaxIterations→ 100]
{a→ 0.398997,b→ 0.000294753,c→ 0.0965191}

fita11=NonlinearRegress[expIVdata11,NC Ecell11,x,{{a,0.1},{b,0.0000009},{c,0.01}}]
g10=Ecell11 20/.fit11
20 (1.34016 +0.00213449 x+0.0333804 ArcSinh[0.014504 x]+0.0287071 ArcSinh[19.6336 x])

gp10=Plot[g10,{x,10,140},Frame→ True, PlotRange→ All, TextStyle→ {FontSize→ 14},
FrameLabel→ {StyleForm["Stack Current A "],StyleForm["Stack Voltage V"]},AxesOrigin->{0,28}, PlotStyle→ {Hue[1,1,0],Thickness[0.006]}, ImageSize→ 500]

<<Statistics`DataSmoothing`
s3=MakeSymbol[{AbsoluteThickness[.05],Circle[{0,0},Offset[{1.2,1.2}]]}];

Data1=ExponentialSmoothing[expIVdata1,0.15`];
Data2=ExponentialSmoothing[expIVdata2,0.15`];
Data3=ExponentialSmoothing[expIVdata3,0.15`];
Data4=ExponentialSmoothing[expIVdata4,0.15`];
Data5=ExponentialSmoothing[expIVdata5,0.15`];
Data6=ExponentialSmoothing[expIVdata6,0.15`];
Data7=ExponentialSmoothing[expIVdata7,0.15`];
Data8=ExponentialSmoothing[expIVdata8,0.15`];
Data9=ExponentialSmoothing[expIVdata9,0.15`];
Data10=ExponentialSmoothing[expIVdata10,0.15`];

```
Data11=ExponentialSmoothing[expIVdata11,0.15`];

AllD=MultipleListPlot[Data1,Data2,Data3,Data4,Data5,Data6,Data7,Data8,Data9,Data10,Data11,
PlotJoined→ False,Frame→ True,PlotRange→ All, TextStyle→ {FontSize→ 14},
FrameLabel→ {StyleForm["Stack Current A"],StyleForm["Stack Voltage V" ]},
SymbolShape→ s3,PlotStyle→ {{AbsoluteDashing[{1.0}],AbsoluteThickness[1.0]},
{AbsoluteDashing[{1.0}], AbsoluteThickness[1]}}, AxesOrigin->{0,28}, ImageSize→ 600];

Show[AllD,gp,gp1,gp2,gp3,gp4,gp5,gp6,gp7,gp8,gp9,gp10]
```

REFERENCES

[1] Robert F. Service, " The Hydrogen Backlash"; *Science*, 35(2004),pg: 958-961

[2] V. Smil, "Energy at the Crossroads: Global perspectives and uncertainties" The MIT Press (2005)

[3] F. Kreith, R.West, "Fallacies of a hydrogen economy: A critical analysis of hydrogen production and utilization", J. of Energy Resources Technology 126(2004) 249-257.

[4] S.P.S. Badwal, S. Giddey, F. T. Ciacchi, "Hydrogen and oxygen generation with polymer electrolyte membrane (PEM)-based electrolytic technology", Ionics 12 (2006) 7-14

[5] S. A. Sherif, F. Barbir, T. N. Veziroglu, "Wind energy and the hydrogen economy-review of the technology", Solar Energy 78 (2005) 647 – 660.

[6] K.W. Harrison "Design, Integration and Control of Proton Exchange Membrane Electrolyzer for Wind Based Renewable Energy Application",(dissertation) , University of North Dakota, August 2006

[7] E.Tzimas, C. Filiou, S.D.Peteves & J.B.Veyret. "Hydrogen Storage State of the Art & Future Perspective." Netherlands Institute for Energy ISBN 92-894-6950-1, 2003.

[8] http://www.eere.energy.gov/hydrogenandfuelcells/education/properties.html

[9] U.S. Department of Energy. 'Hydrogen posture plan' ; Feb 2004

[10] T.N. Veziroglu, S. Sahin, "21st Century's energy: Hydrogen energy system", Energy Conversion and Management 49 (2008) 1820–1831.

[11] S.A. Grigoriev, V. I. Porembsky, V.N. Fateev, "Pure hydrogen production by PEM electrolysis for hydrogen energy", Int. J. of Hydrogen Energy 31 (2006) 171--175.

[12] A. Marshall, B. Borresen, G.Hagen, M. Tsypkin, R. Tunold, "Hydrogen production by advanced proton exchange membrane (PEM) water electrolyzers-Reduced energy consumption by improved electrolcatalysis", Energy 32(2007) 431-436

[13] www.xantrex.com

[14] HOGEN® Hydrogen Generation Systems: Technical Specifications, Proton Energy Systems, Inc., PD-0600-0002 Rev.11.05.

[15] www.lytron.com

[16] www.distributed-energy.com

[17] A. Burke, M.Gardiner, "Hydrogen storage options: Technologies and comparisons for light duty vehicle applications", Institute of Transportation Studies, UCD-ITS-RR-05-01.

[18] J. Larminie, A. Dicks, Fuel Cell Systems Explained, 2nd ed. Chichester, England: Wiley, 2003

[19] R. O'Hayre, " Micro Scale Electrochemistry: Application to Fuel Cells", (dissertation), Stanford University, May 2004

[20] www.ballard.com

[21] Nexa power module user's manual 2003.

[22] A.G. Hombrados, L. Gonzalez, M.A. Rubio, W. Agila, E. Villanueva, D. Guinea, E. Chinarro, B. Moreno, J.R. Jurando, "Symmetrical electric modefor PEMFC characterization using impedance spectroscopy", J. of Power Sources 151 (2005) 25-31.

[23] A.P. Saab, F.H. Garzon, T.A. Zawodzinski , "The effects of processing conditions and chemical composition on electronic and ionic resistivities of fuel cell electrode composites", J. Electrochem Soc 150 (2003): A214-A218.

[24] G. Li, P.G. Pickup, "Ionic conductivity of PEMFC electrode-Effect of Nafion loading", J. Electrochem Soc 150 (2003): C745-C752 .

[25] F. Jaouen, G. Lindbergh, K. Wiezell, "Transients techniques for investigating mass-transport limitations in gas diffusion electrodes", J. Electrochem Soc. 150 (2003) A1711-A1717

[26] M. Ciureanu, R. Roberge, "Electrochemical impedance study of PEM fuel cells, experimental diagnostics and modeling of air cathodes", J.of Phys,Chem. 105 (2001), 3531-3539.

[27] W. Merida, D.A. Harrington, J.M. Le Canut, G. McLean, , "Characterization of proton exchange membrane fuel cell (PEMFC) failures via electrochemical impedance spectroscopy" J. of Power Sources 161 (2006) 264-274.

[28] X. Yuan, J.C. Sun, M. Blanco, H. Wang, J. Zhang, D. Wilkinson, "AC impedance diagnosis of a 500W PEM fuel cell stack, Part I: Stack impedance", J. of Power Sources 161 (2006) 920-928.

[29] E. Barsoukov, J.Ross Macdonald, " Impedance Spectroscopy- Theory, Experiment, and Applications", 2nd Edi., Wiley-Intersciences, 2005.

[30] P. M. Gomadam , J.W. Weidner, "Analysis of electrochemical impedance spectroscopy in proton exchange membrane fuel cells", Int. J. of Energy 29(2005) 1133-1151

[31] R. A. Latham, "Algorithm development for electrochemical impedance spectroscopy diagnostics in PEM fuel cells", (thesis) Department of Mechanical Engg, Uni. of Victoria,Canada, 2004

[32] J.M. Le Caunt, R. M. Abouatallah, D. A. Harrington, "Detection of Membrane Drying, Fuel Cell Flooding, and Anode Catalyst Poisoning of PEMFC Stack by Electrochemical Impedance Spectroscopy", J. of Electrochem Soc., 153 (5) (2006) A 857 – A 864.

[33] W. Choi, J.W. Howze, P. Enjeti, "Development of an equivalent circuit model of a fuel cell to evaluate the effects of inverter ripple current", J. of Power Sources 158 (2006) 1324-1332.

[34] M.C. Lefebvre, R.B. Martin, P.G. Pickup, "Characterization of ionic conductivity profiles within proton exchange membrane fuel cell gas diffusion electrodes by impedance spectroscopy", Electrochemical and Solid –State letters 2 (6) (1999) 259-261

[35] P. M. Gomadam, Weidner J W, Zawodzinski T A, Saab A P, "Theoretical analysis for obtaining physical properties of composite electrodes", J. of Electrochem. Soc. 150(8) (2003) E371-E376

[36] M. Oszcipok, D.Reimann, U. Kronenwett, M. Kreideweis, M.Zedda, "Statistic analysis of operational influences on the cold start behavior of PEM fuel cells", J. of Power Sources 145(2005) 407-415.

[37] J. Amphlett, B. Peppley, E. Halliop, A. Sadiq, "The effect of anode flow characteristics and temperature on the performance of direct methanol fuel cell", J.of Power Sources 96(2001) 204-213.

[38] S. Cleghorn, D. Mayfield, D. Moore, J. Moore, G. Rusch, T. Sherman, , "A polymer electrolyte fuel cell life test: 3 years of continuous operation", J. of Power sources 158 (2006) 446-454.

[39] H. Song, D. Shin, "Influence of CO concentration and reactant gas pressure on cell performance in PAFC", Int. J. of Hydrogen Energy 26 (2001) 1259-1262.

[40] W. Zhu, R. Payne, B. Tararchuk, "PEM stack test and analysis in a power system at operational load via ac impedance", J. of Power Source 168 (2007) 211-217.

[41] N. Wagner, E. Gulzow, "Change of electrochemical impedance spectra (EIS) with time during CO-poisoning of the Pt-anode in a membrane fuel cell", J. of Power Sources 127(2004) 341-347.

[42] X. Yan, M. Hou, L. Sun, D. Liang, Q. Shen, H. Xu, P. Ming, B. Yi, "AC impedance characteristics of a 2 kW PEM fuel cell stack under different operating conditions and load changes", Int. J. of Hydrogen Energy 32(2007) 4358-4364.

[43] www.solartronanalytical.com

[44] www.chromausa.com

[45] X. Yuan, J.C. Sun, H. Wang, J. Zhang, "AC impedance diagnosis of a 500W PEM fuel cell stack, Part II: Individual cell impedance", J. of Power Sources 161 (2006) 929-937.

[46] www.scribner.com

[47] www.home.agilent.com

[48] www.yesmec.com

[49] www.sonicelectronix.com

[50] R. O'Hayre, S.Cha, W. Collela, F. B. Prinz, Fuel Cell Fundamentals, John Wiley & Sons, Inc. (2006)

[51] Princeton Applied Research, Basics of Electrochemical impedance spectroscopy, application note AC-1, 2005.

[52] T. Romero-Castanon, L.G. Arriaga, U. Cano-Castillo, "Impedance spectroscopy as a tool in the evaluation of MEA's", J. Power Sources 118 (2003) 179-182

[53] A. Fischer, J. Jindra, H. Wendt, "Porosity and catalyst utilization of thin layer cathodes in air operated PEM-fuel cells", J. Appli. Electrochem. 28 (1998) 277-282

[54] F. Jaouen, G. Lindbergh, G. Sundholm, "Investigation of Mass-Transport Limitations in the Solid Polymer Fuel Cell Cathode. I. Mathematical Model", J. Electrochem Soc. 149 (2002) A437-A447.

[55] J. Ihonen, F. Jaouen, G. Lindbergh, A. Lundblad, G. Sundholm, "Investigation of Mass-Transport Limitations in the Solid Polymer Fuel Cell Cathode. II. Experimental", J. Electrochem Soc. 149 (2002) A448-A454

[56] R. Makharia, M. Mathias, D. Baker, "Measurement of Catalyst Layer Electrolyte Resistance in PEFCs Using Electrochemical Impedance Spectroscopy", J. Electrochem Soc. 152 (2005) A970-A977

[57] S. Roy, M. Orazem, B. Tribollet. "Interpretation of Low-Frequency Inductive Loops in PEM Fuel Cells", J. Electrochem Soc. 154 (2007) B1378-B1388.

[58] O. Antoine, Y. Bultel, R. Durand, "Oxygen reduction reaction kinetics and mechanism on platinum nanoparticles inside Nafion", J. Electroanal. Chem. 499(2001) 85-94.

[59] M.L. Perry, J. Newman, E.J. Cairns, "Mass Transport in Gas Diffusion Electrodes: A Diagnostic Tool for Fuel-Cell Cathode", J. Electrochem. Soc. 145 (1998) 5–15.

[60]Y. Chu, Y.G. Shul, W. C. Choi, S. I. Woo, H. Han, "Evaluation of the Nafion effect on the activity of Pt-Ru electrocatalysts for the electro-oxidation of methanol", J. of Power Sources 118 (2003) 334–341

[61] T.J.P. Freire, E.R. Gonzalez, "Effect of membrane characteristics and humidification conditions on the impedance response of polymer electrolyte fuel cells", J. Electroanal. Chem., 503 (2001) 57–68

[62] V.A. Paganin, C.L.F. Oliveira, E.A. Ticianelli, T.E. Springer, E.R. Gonzalez, "Modelistic interpretation of a polymer electrolyte fuel cell", Electrochim. Acta 43 (1998) 3761–3766

[63] J.P. Diard, B.Le Gorrec, C. Montella, C. Poinsignon, and G. Vitter, " Impedance measurement of polymer electrolyte membrane fuel cells running on constant load", J. of Power Sources 74 (1998) 244 – 245 .

[64] I. A. Schneider, H. Kuhn, A. Wokaun, and G.G. Scherer, " Study of water balance in a polymer electrolyte fuel cell by locally resolved impedance spectroscopy", J. of Electrochem. Soc., 152 (2005) A2383-A2389

[65] C.Y. Biaku, N.V. Dale, A.J. Peters, M.D. Mann, H. Salehfar,T. Han, "A Semi-Empirical Study of the Temperature Dependence of the Anode Charge Transfer Coefficient of a 6 kW PEM Electrolyzer", Int. J. of Hydrogen Energy, In Press.

[66] K. W. Harrison, E. Hernandez-Pacheco, M. Mann, H. Salehfar, "Semiempirical model for determining PEM electrolyzer stack" *J. of Fuel Cell Science and Technology*, 3 (2006) 220-223.

[67] R.L. LeRoy, C.T. Bowen, "The thermodynamics of aqueous water electrolysis", *J. Electrochem Soc.*, 127(1980) 1954-1962

[68] J.M. Smith, H.C. Van Ness, M.M. Abbott, " Introduction to chemical engineering thermodynamics" McGraw-Hill Publ. 2003

[69] T. Oi, Y. Sakaki, "Optimum hydrogen generation capacity and current density of the PEM-type water electrolyzer operated only during off-peak period of electricity demand", *J. of Power Sources*, 129 (2004) 229-237.

[70] P. Choi, D. Bessarabov, R. Datta, "A simple model for solid polymer electrolyte (SPE) water electrolysis" Solid State Ionics 175 (2004) 535–539.

[71] D. A. Noren, M.A. Hoffman, "Clarifying the Butler-Volmer equation and related approximations for calculating activation losses in solid oxide fuel cell models", J. of Power Sources 152 (2005) 175–181.

[72] A. Roy, S. Watson, D. Infield, Int. J. of Hydrogen Energy 31(2006) 1964 – 1979.

[73] J. Ivy, "Summary of electrolytic hydrogen production: milestone completion report", NREL/MP-560-36734. September 2004.
Website: http://www.nrel.gov/docs/fy04osti/36734.pdf, last accessed on April 21, 2008.

[74] A. Marshall, B. Borresen, G. Hagen, M. Tsypkin, R. Tunold, "Hydrogen production by advanced proton exchange membrane (PEM) water electrolysers-Reduced energy consumption by improved electrocatalysis" Energy 32 (2007)431–436.

[75] H. Ruskeepaa, "Mathematica Navigator", 2nd edi. Elsevier Academic Press, 2003.

[76] A. Parthasarathy, S. Srinivasan, A.J. Appleby. "Temperature dependence of the electrode kinetics of oxygen reduction at the platinum/nafion interface – A microelectrode investigation", J of the Electrochem. Soc. 139(9) 1992, 2530-2537

[77] T. Springer, T. Zawodzinki, S. Gottesfeld, "Polymer electrolyte fuel cells", J. of Electrochem. Soc., 2003, 138 (8), 2334-2342

[78] http://www.energyvortex.com/files/HighPurity_H2.pdf

[79] D. White and C. Heinric, "What is Clean, Dry Air?," Technical Article Program (TAP), Compressed Air and Gas Institute, TAP#106,2002.

[80] N. V. Dale, K.W. Harrison, T. Han, M.D. Mann, H. Salehfar, A.M. Dhirde, "Hydrogen dew point control in renewable energy systems using thermoelectric coolers", IEEE PES General Meeting 2008 Proceedings, 2008

[81] http://www1.eere.energy.gov/hydrogenandfuelcells/pdfs/doe_h2_storage.pdf.

[82] J.M. Sedlak, J.F. Austin and A.B. Laconti, "Hydrogen recovery and purification using the solid polymer electrolyte electrolysis cell", Int. J. of Hydrogen Energy 1981 (6) 45–51.

[83] B. Rohland, K. Eberle, R. Strobel, J. Scholta and J. Garche, "Electrochemical Hydrogen compressor", Electrochimica Acta, 1998 (43) 3841-3846

[84] R. Srobel, M. Oszcipok, M. Fasil,B. Rohland, "The compression of hydrogen in an electrochemical cell based on a PE fuel cell design", J. of Power sources, 2002 (105) 208–215.

[85] S. Porter: Anuual Merit Review, DOE Hydrogen Program, 2005.

[86] K.C. Neyerlin, Wenbin Gu,Jacob Jorne,H.A. Gasteiger, "Study of the exchange current density for the hydrogen oxidation and evolution reactions", J. of Electrochem Soc. 154(7) (2007) B631-B635